

Experimental investigation of mini Gurney flaps in combination with vortex generators for improved wind turbine blade performance

Jörg Alber¹, Marinos Manolesos², Guido Weinzierl-Dlugosch³, Johannes Fischer³, Alexander Schönmeier¹, Christian Navid Nayeri¹, Christian Oliver Paschereit¹, Joachim Twele⁴, Jens Fortmann⁴, Pier Francesco Melani⁵, Alessandro Bianchini⁵.

¹ Technische Universität Berlin, Hermann-Föttinger Institut, Müller-Breslau-Str. 8, 10623 Berlin, Germany

² College of Engineering, Swansea University, Bay Campus, Fabian Way, Swansea, SA1 8EN, United Kingdom

³ SMART BLADE GmbH®, Waldemarstr. 39, 10999 Berlin, Germany

⁴ Hochschule für Technik und Wirtschaft Berlin, Wilhelminenhofstraße 75A, 12459 Berlin, Germany

⁵ Università degli Studi di Firenze, Department of Industrial Engineering (DIEF), Via di Santa Marta 3, 50139 Firenze, Italy

Correspondence to: Jörg Alber (joerg.alber@posteo.de)

Abstract

This wind tunnel study investigates the aerodynamic effects of Mini Gurney flaps (MGFs) and their combination with vortex generators (VGs) on the performance of airfoils and wind turbine rotor blades. VGs are installed on the suction side aiming at stall delay and increased maximum lift. MGFs are thin angle profiles that are attached at the trailing edge in order to increase lift at pre-stall operation. The implementation of both these passive flow control devices is accompanied by a certain drag penalty. The wind tunnel tests are conducted at the Hermann- Föttinger Institut of the Technische Universität Berlin based on two airfoils that are characteristic for different sections of large rotor blades. Lift and drag are determined using a force balance and a wake rake, respectively, for static angles of attack between -5° to 17° at a Reynolds number of 1.5 million. The impact of different MGF heights including 0.25%, 0.5% and 1.0 % and a VG height of 1.1 % of the chord length is tested and evaluated. Furthermore, the clean and the tripped baseline cases are considered. In the latter, leading edge transition is forced with Zig Zag (ZZ) turbulator tape. The preferred configurations are the smallest MGF on the NACA63(3)618 and the medium sized MGF combined with VGs on the DU97W300. Next, the experimental lift and drag polar data is imported into the software QBlade in order to design a generic rotor blade. The blade performance is simulated with and without the add-ons by means of two case studies. In the first case, the retrofit application on an existing blade mitigates the adverse effects of the ZZ tape. Stall is delayed and the aerodynamic efficiency is partly recovered leading to an improvement of the power curve. In the second case, the new design application allows for the design of a more slender blade while maintaining the rotor power. This alternative blade appears to be more resistant against the adverse effects of forced leading edge transition.

1. Introduction

30 1.1 General outline

This report is divided into the following sections.

Introduction. The concepts, mechanisms and applications of Gurney flaps (GFs), ZZ tape and VGs are introduced. The literature review is focused on very small GF heights, so-called MGFs, and their combination with VGs.

Airfoil simulations. The simulation software XFOIL (Drela, 1989) is used to determine the appropriate size of each passive
35 flow control (PFC) device in relation to the local boundary layer thickness of the NACA63(3)618 (tip region) and the DU97W300 (root region).

Experimental set-up. The wind tunnel test section, the measurement methods and the data reduction process are specified including the force balance for the lift, and the wake rake for the drag measurements at a constant Reynolds number of $Re = 1.5 \cdot 10^6$.

40 **Experimental results.** The lift and drag polars, $c_l(\alpha)$ and $c_d(\alpha)$, are presented. Different combinations of MGFs and VGs are evaluated according to characteristic parameters, i.e. the lift performance, the stall behavior and the aerodynamic efficiency.

Rotor blade performance. The experimental data is imported into the software QBlade (Marten, 2020) in order to create a generic rotor blade. The blade performance is simulated by means of two case studies, the retrofit application on an existing, and the new design application on an alternative rotor blade.

45 1.2 Gurney flaps

This aerodynamic device is named after the US racecar driver Dan Gurney. In the early 1970s, he applied it to the rear spoilers achieving significant improvements in the downforce and thus the traction of his Formula One vehicles, see Liebeck (1978).

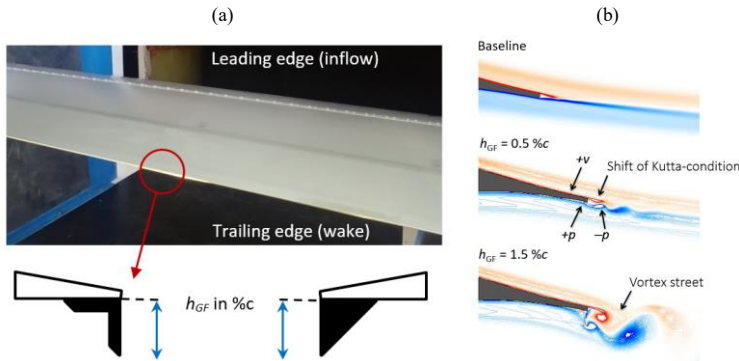
Passive GFs are categorized as static miniflaps or miniature trailing edge devices (MiniTEDs), as described by González-Salcedo et al. (2020). They are different to the concept of flexible trailing edge (TE) flaps that are integrated into the very TE
50 section, see Barlas and van Kuik (2010). The first reference to miniflaps dates back to the early 20th century and was probably developed by Gruschwitz and Schrenk (1933). Zaparka (1935) registered the first patent on active miniflaps for use on airplane wings. Various patents of passive miniflaps followed, particularly in aviation. Boyd (1984) and later Brink (2002) claimed the rights on different versions of wedge-shaped TE flaps. Henne and Gregg (1989) patented the shape of a diverging trailing edge (DTE) of a transonic airfoil generating similar aerodynamic effects than the GF. Bechert et al. (2001) registered a patent on
55 so-called three dimensional (3D) GFs, i.e. profiles with slits, serrations, holes, as well as tiny vortex generators attached to the miniflap itself to stabilize the unsteady wake field. Wang et al. (2008) published a comprehensive review of GFs for use on rotor blades of helicopters and wind turbines. In contrast to the large amount of patents and publications, there are only few examples of standardized or commercialized GF applications on rotor blades of horizontal axis wind turbines (HAWTs). For instance, Vestas (2019) offers GFs in combination with VGs as aerodynamic upgrades of operating wind turbines predicting
60 the average energy production (AEP) to increase by 1.7%. Another example is the blade design of the 10 MW reference wind

Commented [D2]: RC1(Q3minor): PFC not defined

Commented [D3]: RC2: AH93W174 was removed for space economy

Commented [D4]: RC2: typo

turbine of the Danish Technical University (DTU) with a total rotor radius of $R = 89.2$ m. The inner blade part alongside the local rotor radius of $5\%R < r < 40\%R$ was equipped with wedge-shaped GFs including heights of 3.5%, 2.5% and 1.3%, respectively, in relation to the local chord length, c . Bak et al. (2013) claim significant aerodynamic performance improvements, especially on relatively thick airfoils with a maximum thickness greater than $30\%c$.



65 Figure 1. (a) NACA63(3)618 during wind tunnel tests. Vortex generator array and Gurney flap. Definition of Gurney flap height of rectangular and triangular profiles in side view. (b) CFD simulations of the HQ17. Wake structures at $\alpha = 0^\circ$ and $Re = 1 \cdot 10^6$ for different Gurney flap heights, reproduced and modified from Schatz et al. (2004a).

Figure 1a displays the typical GF shapes, i.e. the rectangular, or L-shaped, and the triangular, or wedge-shaped, profiles. Typically, they are installed at the TE and normal to the pressure side of wings and rotor blades. In both cases, the effective GF height, h_{GF} , is expressed in $\%c$, without taking the original TE thickness into account. For identical h_{GF} , the aerodynamic effect of both GF profiles is considered to be very similar, as discussed in Appendix B2. **It is noted that GFs are also used at a certain distance away from the TE. These mini tabs, see Bach et al. (2014), are out of the scope of this study.**

Commented [D5]: RC1 (Q5major): different chordwise positions of GFs were mentioned

Figure 1b illustrates the principal changes of the flow field for two different GF heights, as first reported by Liebeck (1978).

75 Adjacent to the TE modification, a highly efficient vortex system is formed consisting of one vortex upstream and two counter rotating vortices immediately downstream. Bechert et al. (2000) and Schatz et al. (2004b) showed by means of experimental and numerical investigations that the wake structures are quasi two dimensional (2D) at pre stall operation. The recirculation region changes the Kutta condition, so that the rear stagnation point is shifted downstream and deflected downwards, see also Jeffrey et al. (2000) and Cole et al. (2013). The modifications of the flow field lead to the following set of simultaneous effects.

- 80 • Lift performance. The suction peak is higher and coupled with a positive pressure built-up right in front of the GF, as such increasing the pressure difference between the suction and the pressure side. As a results, the effective camber is enhanced, so that the same lift coefficient, c_l , is already reached at a lower angle of attack (AoA), α . Furthermore, the adverse pressure gradient on the suction side becomes milder generating a higher maximum lift coefficient, $c_{l,max}$.

85 • Drag behavior. The recirculation or low pressure region in the immediate wake leads to an increased momentum loss and thus higher drag coefficient, $c_d(\alpha)$. In addition, the intensity of the wake unsteadiness is stronger, especially if vortex shedding is initiated in the form of an absolute instability, as illustrated for $h_{GF} = 1.5\%$ in Figure 1b.

Overall, the impact of GFs is quantifiable as an increase in both lift and drag. Bechert et al. (2000) and later Schatz et al. (2004b) showed that the drag increase is related to both the intensity and the frequency of the wake unsteadiness. As a consequence, the drag penalty was less severe for small GF heights comparing $h_{GF} = 0.5\%$ to 1.5% , see Figure 1b.

Commented [D6]: RC1 (Q2minor) and RC2: For clarity, the following statement was removed.

90 1.3 Zig Zag tape

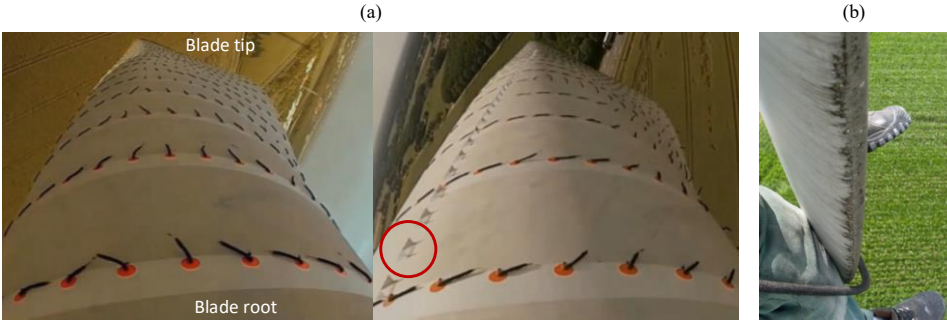
ZZ turbulator tape is implemented to initiate the boundary layer (BL) transition at a fixed chord position, see Figure 3a. Its height, h_{ZZ} , should be smaller than the local BL thickness in order to trigger transition while avoiding a disproportionate drag increase or even turbulent separation. Next to trip wire or carborundum paper, ZZ tape facilitates the comparability between different measurement methods. Moreover, it is applied to evaluate the sensitivity of airfoils to the adverse effects of leading edge roughness (LER), as discussed by van Rooij and Timmer (2003), Timmer and Schaffarczyk, (2004) and in greater detail by Wilcox et al. (2017). Another example is Oerlemans et al. (2009), who implemented ZZ tape on the rotor blades of a commercial multi MW wind turbine. In fact, LER due to erosion and the accumulation of sediments are major challenges for rotor blade manufacturers and wind turbine operators, see Figure 2b. Over time, LER is practically inevitable. According to Maniaci (2020), it mainly affects the mid to tip region, where the rotor blade is exposed to the highest relative velocities.

100 Depending on the degree of roughness, the AEP decrease of multi MW HAWTs is between of 2 % and 5 %.

Commented [D7]: RC2: commercial instead of research wind turbine

1.4 Vortex generators

As opposed to GFs, VGs have been commercialized by various wind energy companies for almost two decades. Usually, the suboptimal or declining AEP motivates blade manufacturers and wind park operators to investigate possible causes, such as



105 Figure 2. Utility scale wind turbines. (a) Simultaneous flow tuft measurements (baseline versus VG configuration) on the same rotor, with permission from SMART BLADE GmbH. (b) Leading edge erosion at the blade tip, with permission from Seilpartner GmbH.

early separation or LER. One possible solution is the installation of VGs to alleviate the flow separation in the root to mid region of rotor blades. More recent studies have also investigated the opportunities of relatively small VG sizes towards the tip region, see Bak et al. (2018). Typically, VGs are commercialized as retrofit solutions, i.e. add-ons that are installed on the surface of already running rotor blades, as depicted in Figure 2a. In this way, SMART BLADE (2021) predict an AEP growth of approximately 2%. A more detailed review on VGs for use on rotor blades is provided by Bak et al. (2016) and González-Salcedo et al. (2020).

The purpose of VGs is to delay the BL stagnation and thus separation, see Figure 2a. As such, the flow tufts are attached to the blade surface, as compared to the stalling baseline blade. The thin vanes shed a pair of vortices transporting momentum from the more energetic flow into the viscous layers close to the surface. The vortex system spreads out towards the TE, where it is released into the wake. More detailed research on the mechanism of VGs is provided by Manolesos and Voutsinas (2015). Overall, the VG effect is quantifiable as a substantial increase in both maximum lift and the AoA where stall is initiated, $\alpha(c_{l,max}) = \alpha_{cl,max}$. At the same time, drag is increased significantly at low and moderate AoA. The impact on the aerodynamic efficiency, L/D (α), depends on the design parameters that are summarized in Figure 3.

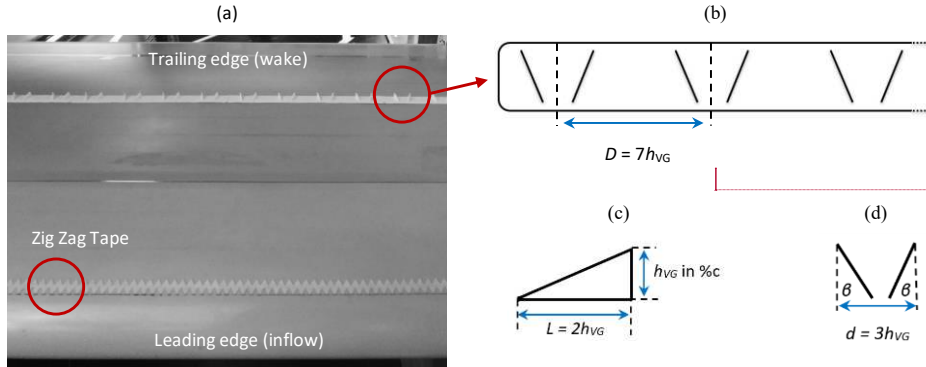


Figure 3. NACA63(3)618 during wind tunnel tests. (a) Top view on suction side with ZZ tape and VG array. (b) VG panel including spacing between VGs, with permission from SMART BLADE GmbH. (c) Side view of single vane. (d) Top view of single VG.

Figure 3a and b depict an array of VG panels, as installed on the suction side of the airfoil model. Following Baldacchino et al. (2018), the design parameters generate a counterrotating, common downflow VG system. The spacing between the center points of two VGs is defined as $D = 7h_{VG}$, see Figure 3b. Figure 3c shows that each VG consists of a delta-shaped pair of vanes with a length, $L = 2h_{VG}$, and the VG height, h_{VG} , given in %c. According to Figure 3d, the distance between the two vanes, $d = 3h_{VG}$, results in $\beta \approx \pm 18^\circ$.

Commented [D9]: RC2: sentences were improved, i.e. paragraph was rewritten

Commented [D10]: RC2: idem

Commented [D12]: RC2: Indication of wake rake positions was deleted to avoid confusion

Commented [D13]: RC2: The content of this paragraph was summarized and shortened.

1.5 Combining Vortex generators and Gurney flaps

130 Despite the large body of literature on each device, the simultaneous use of GFs and VGs is less profoundly researched. Storms
et al. (1994) investigated one such configuration in the NASA Ames Research Center using a NACA4412 profile. Stall was
delayed by around 5° and $c_{l,max}$ was increased by 36 % improving L/D at elevated AoA. However, at low and moderate AoA,
the combined drag penalty led to decreased aerodynamic efficiency. Fuglsang et al. (2003) conducted experiments in the
VELUX wind tunnel of the DTU based on the Riso-B1-24. To the authors’ knowledge, this is the only experimental study
applying VGs and GFs on a dedicated wind turbine airfoil. Stall was delayed by approximately 3°, coupled with an increase
135 in $c_{l,max}$ of 34 %. Similar results were achieved installing ZZ tape on the suction side. Following from that, Fuglsang et al.
(2004) concluded that, despite the small L/D decrease, the combination of both devices “(...) could provide an attractive choice
for the root part of a wind turbine blade where reduction of solidity is a key issue to reduce blade costs.”. In a more recent
study, Li-shu et al. (2013) performed wind tunnel tests on a WA251A airfoil at the Northwestern Polytechnical University of
Xi’an. Maximum lift was increased by 18.6 % delaying stall by approximately 2°. The authors report “remarkable
140 improvements” implementing both PFC devices simultaneously. For clarity, the design parameters of the mentioned references
are summarized in Table 1.

Table 1. Literature references. GF and VG design parameters.

Airfoil	Reference	Re [$\cdot 10^6$]	h_{GF} [%c]	h_{VG} [%c]	x_{VG} [%c]	D [h_{VG}]
NACA4412	Storms et al. (1994)	2.0	1.25	0.5	12	6.0
Riso-B1-24	Fuglsang et al. (2003)	1.6	1.0	1.0	20	4.2
WA251A	Li-shu et al. (2013)	3.0	0.9, 1.25	0.5	21	unspecified

145 The literature review shows that GFs, ZZ tape and VGs are well-studied PFC devices. However, to the authors’ knowledge,
there are no scientific reports investigating MGF heights smaller than 0.5%c and their combination with VGs for use on
dedicated wind turbine airfoils. This study aims at closing these research gaps.

2. Airfoil simulations

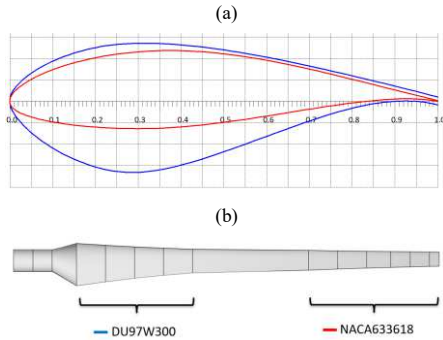
150 In preparation for the wind tunnel tests, the simulation software XFOIL is used to determine the appropriate size of each PFC
device in relation to the local boundary layer thickness of the corresponding airfoil.

2.1 Airfoils

Figure 4a displays the two airfoils that are tested during the wind tunnel experiments, the NACA63(3)618 and the DU97W300.
They are applied at different sections of large rotor blades, see Figure 4b. The main specifications are summarized in Table 2.

Commented [D14]: Q1(major): The section was rewritten highlighting the novelty of this study in comparison to the given references

Commented [D15]: RC2: The information of this paragraph were presented in a more lucid table



155 Figure 4. NACA63(3)618 and DU97W300. (a) Airfoil coordinates normalized by the chord length. (b) Airfoil position on a generic rotor blade.

Table 2. Maximum thickness, maximum camber and trailing edge thickness. Chord position in brackets. All values in %c.

Airfoil	$h_{t,max}(x)$	$h_{camber,max}(x)$	h_{TE}
NACA63(3)618	18.0 (34.0)	3.0 (53.7)	0.17
DU97W300	30.0 (29.3)	2.1 (80.5)	1.75

160 The NACA63(3)618 is part of the six-digit wing sections developed by the National Advisory Committee for Aeronautics (NACA) for use on high speed aircrafts, see Abbott and von Doenhoff (1959). The NACA 63 and 64 families are still popular for the design of large rotor blades, see Timmer (2009). The DU97W300 was designed by the Delft University (DU) as a dedicated wind turbine airfoil, see Timmer and van Rooij (2003).

2.2 XFOIL simulations

165 The 2D airfoil performance is simulated with the panel code XFOIL. The freely available and widely recognized software is based on a viscid-inviscid interaction scheme, which was validated, for instance by Timmer and Schaffarczyk (2004). Apart from the airfoil coordinates, including the finite TE thickness, the software requires the chord-based Reynolds number and the AoA range as input parameters, here $Re = 1.5 \cdot 10^6$ and $-5^\circ < \alpha < 20^\circ$. The location of the free BL transition is modeled by means of the e^N method. The amplification factor, or N criterion, describes the level of both the surface roughness and the inflow turbulence intensity. The default value, $N = 9$, refers to clean conditions, i.e. assuming a completely smooth surface and laminar inflow conditions that are found in low turbulence wind tunnels. In this study, $N = 5$ is chosen to account for the measured turbulence intensity of the current wind tunnel facility. In the so-called tripped case, the transition location is fixed at a static chordwise position, x_{zz} , on both the suction and the pressure side.

Commented [D16]: RC2: AH93W174 was removed for brevity

Commented [D17]: RC2: Excessive information on airfoils was removed

Commented [D18]: RC1 (Q2major): The statement was rephrased avoiding the term "strong turbulence intensity".

The appropriate height of each PFC device is determined in relation to the local BL thickness, δ , which is defined as the normal distance between the solid surface and the first streamline reaching 99% of the axial free flow velocity. XFOIL calculates the BL displacement thickness, δ^* , describing the distance by which the free flowing streamlines are displaced from the solid surface due to the existence of the BL. According to Schlichting and Gersten (2000), the laminar BL thickness on a flat plate at zero incidence is approximately three times the BL displacement thickness,

$$\delta \approx 3\delta^*. \quad (1)$$

Eq. (1) is also valid for thin airfoil shapes. According to Baldacchino et al. (2018), the turbulent BL thickness is related to δ^* and the momentum thickness θ ,

$$\delta \approx \theta \left(3.15 + \frac{1.72}{(\frac{\delta^*}{\theta}) - 1} \right) + \delta^*. \quad (2)$$

2.3 Zig Zag tape

The baseline configurations include both the free and the forced BL transition. In the tripped case, ZZ tape is applied alongside the complete airfoil span on both the suction side (SuS) at $x_{ZZ} = 5\%$ and at the pressure side (PS) at $x_{ZZ} = 10\%$, as illustrated in Figure 3a. The ZZ tape height is selected in relation to the laminar BL thickness, see Eq. (1), the corresponding chord positions, x_{ZZ} , and the design AoA, $\alpha_{opt} = \alpha(L/D_{max})$,

$$h_{ZZ} \leq \delta(\alpha_{opt}, x_{ZZ}). \quad (3)$$

Table 3. XFOIL simulations of the boundary layer thickness according to Eq. (1).

	$\alpha_{opt} [^\circ]$	$\delta_{SuS} [mm]$	$\delta_{PS} [mm]$
NACA63(3)618	5	0.51	0.55
DU97W300	9	0.54	0.42

Based on Table 3 and Eq. (3), the NACA63(3)618 is equipped with $h_{ZZ} = 0.4$ mm and the DU97W300 with $h_{ZZ} = 0.3$ mm. As such, the ZZ tape penetrates the upper layers of the BL without increasing drag excessively. The width of the turbulator tape is 12 mm and the angle between its serrations is 60° . These characteristics are in close agreement with comparable wind tunnel tests at the DU and the DTU, see Timmer and van Rooij (2003) and Fuglsang et al. (2004).

2.4 Mini Gurney flaps

Kentfield (1996), Giguère et al. (1997) and Bechert et al. (2000) postulated that the GF needed to be covered by the local BL in order to avoid an excessive drag, in relation to the lift increase. Following from that, Alber et al. (2017) evaluated wind tunnel data of 9 different DU and NACA airfoils at $1 \cdot 10^6 < Re < 2 \cdot 10^6$. It was concluded that L/D (α) could only be maintained or improved using very small GFs in the range of $0.2\%c \leq h_{GF} \leq 0.5\%c$, i.e. GFs that were submerged deeply into the local BL. However, the BL thickness depends on the interaction of multiple factors, such as the Reynolds number, the AoA and the

Commented [D19]: RC2: The selection of the ZZ height was explained with more clarity.

transition location. Hence, the definition of a MGF hereby refers to a height of between one and two times the local BL displacement thickness at the design AoA,

$$\delta^*(\alpha_{opt}) \leq h_{MGF} \leq 2\delta^*(\alpha_{opt}). \quad (4)$$

Within the range given by Eq. (4), the MGF effect on the airfoil performance is assumed to be beneficial throughout the pre-stall region, as further investigated by means of the wind tunnel measurements, see Sect. 4. Moreover, combining Eq. (2) and Eq. (4), an appropriate MGF height may also be estimated as approximately one quarter of the turbulent BL thickness,

$$h_{MGF} \approx 0.25\delta(\alpha_{opt}). \quad (5)$$

Table 4. XFOIL simulations of the boundary layer displacement thickness and the resulting MGF heights according to Eq. (4).

	clean			ZZ	
	α_{opt} [°]	δ^* [%c]	h_{MGF} [%c]	δ^* [%c]	h_{MGF} [%c]
NACA63(3)618	5	0.17	0.17...0.34	0.28	0.28...0.56
DU97W300	9	0.25	0.25...0.50	0.35	0.35...0.70

Table 4 shows that h_{MGF} is case dependent on the airfoil itself and on whether transition is free or fixed. In the latter case, δ^* is increased significantly due to the early expansion of the turbulent BL. For the purpose of the current wind tunnel tests, the following flap heights are installed: 0.25%c, 0.5 %c and 1 %c, as such covering both the clean and the tripped cases. Even though it is not considered a MGF as per Eq. (4), $h_{GF} = 1$ %c is included as a common literature reference. Unless specified otherwise, the GFs consist of rectangular, i.e. equilateral angle profiles made of brass.

2.5 Vortex generators

The chord position of the VG array, x_{VG} , is located upstream of the mean separation line to delay stall, $x(\alpha_{cl,max})$, and downstream of the BL transition location to limit drag at pre-stall operation, $x(\alpha_{opt})$. The VG height is determined in relation to the turbulent BL thickness at maximum lift,

$$h_{VG} = f[\delta(x_{VG}, \alpha_{cl,max})]. \quad (6)$$

It is noted that XFOIL simulations are of low order, especially for AoA close to stall. Nonetheless, the estimation of the BL thickness is considered to be sufficiently accurate for the purpose of the current VG design.

Table 5 shows that $\delta(x_{VG})$ is similar in both the clean and the tripped cases at maximum lift, i.e. as stall is initiated. Based on Eq. (6), the VG height of $h_{VG} = 1.1$ %c is selected. In case of the DU97W300, $h_{VG} > \delta(x = 30$ %c) resembles a standard VG array in the root to mid region of a rotor blade. Regarding the NACA63(3)618, a sub boundary layer VG configuration is investigated with $h_{VG} < \delta(x = 50$ %c), as discussed by Lin (2002) and Bak et al. (2018). In the mid to tip blade region, the objective is to reduce drag and to maintain $L/D(\alpha)$ on a high level.

Commented [D20]: RC1 (Q9major): For clarity, the range of the MGF heights was specified and included in the Table

Commented [D21]: RC1 (Q13major): the misleading term "at stall" was replaced

Table 5. XOIL simulations of the boundary layer thickness according to Eq. (2).

	$\alpha_{cl,max} [^\circ]$	$x_{VG} [\%c]$	$\delta_{clean}(x_{VG}) [\%c]$	$\delta_{ZZ}(x_{VG}) [\%c]$
NACA63(3)618	12	50	1.55	1.62
DU97W300	12	30	0.58	0.72

2.6 Summary

Figure 5a displays both the height and the chordwise location of each PFC device that is investigated in this section. According to previous research efforts at the TU Berlin, Figure 5b and c depict the vorticity caused by either VGs or MGFs. The wake interaction of the flow control mechanisms and its effects on the lift and drag performance is presented as part of the wind tunnel tests in Sect.4.

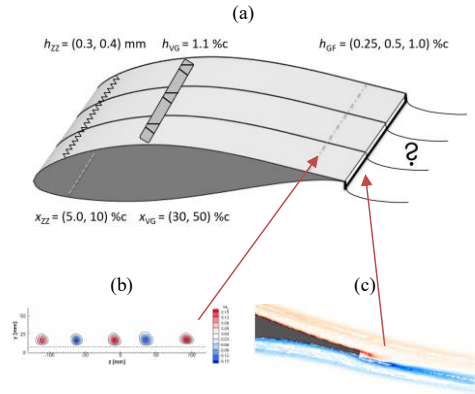


Figure 5. (a) Height and location of passive flow control devices. (b) Particle Image Velocimetry (PIV) measurements of VG vortices on the NACA63(3)618 in spanwise view ($h_{VG} = 1.7\%c$ at $x_{PIV} = 80\%c$ and $Re = 1.3 \cdot 10^6$), reproduced from Mueller-Vahl et al. (2012). (c) CFD simulations of a MGF on the HQ17 in side view ($h_{GF} = 0.5\%c$ at $\alpha = 4^\circ$ and $Re = 1 \cdot 10^6$), reproduced from Schatz et al. (2004a).

3. Experimental setup

The wind tunnel test section, the measurement methods and the data reduction process are specified, including the force balance for the lift, and the wake rake for the drag measurements at a Reynolds number of $Re = 1.5 \cdot 10^6$.

3.1 Test section

The experiments are conducted in the large closed-loop wind tunnel of the HFI at the TU Berlin. The airfoil test section is 2 m in width and 1.44 m in height. It consists of a 2.5 m long removable structure that is attached to the duct outlet, see Figure

Commented [D23]: RC1(Q4minor): The term "airfoil box" was replaced

6a. The contraction ratio is 6.25 : 1 and the complete length of the test section is 5 m. It was designed, constructed and integrated into the wind tunnel by Meyer (2000).

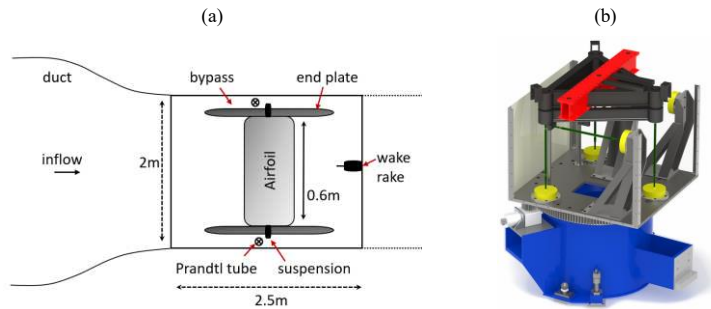


Figure 6. (a) Airfoil test section in top view. (b) Force balance underneath the test section in side view, load cells in yellow, support for attaching the frame of the wing model in red.

The inlet and the outlet of the duct walls are equipped with a ring line of pressure taps. The inflow velocity is determined from the contraction ratio and the static pressure difference. The airfoil model, or wing, is positioned in the centre of the test section, as displayed in Figure 6a. It is enclosed by two 1.5m long end plates that are parallel to the tunnel, as such reducing the influence of the wall BL. The velocities inside the 0.25 m wide bypass channels are measured via two separate Prandtl tubes to obtain the effective inflow velocity. The wing is directly clamped to the platform of the permanently installed force balance underneath the test section, see Figure 6b. Hence, the suspension is decoupled from the end plates and the tunnel walls. The AoA is controlled by means of a stepping motor with an accuracy of 0.1° , which is directly attached to the suspension. The wing models were CNC milled from a solid block of ObomodulanTM, as described by Pechlivanoglou (2013). The chord length is 0.6 m and the span is 1.54 m resulting in an aspect ratio of 2.56.

3.2 Measurement methods

3.2.1 Force balance

The lift forces are directly transferred to the six component force balance, see Figure 6b. The load cells consists of strain gauges generating voltage signals that are proportional to the incoming forces. Each signal is digitalized by a CompactDAQ System of National Instruments with a sampling rate of 5 kHz. The data is recorded using a LabVIEW user interface, including forces, velocities and environmental conditions, i.e. air density and kinematic viscosity, all of which are automatically converted to average results at each AoA. The LabVIEW interface also contains the AoA control in terms of range, steps and measurement duration. According to Meyer et al. (2016), the uncertainty of the uncorrected lift coefficients, $c_{l,raw}(\alpha)$, is 0.2%. As such, the lift results show good agreement with literature data, as shown in Appendix B1. However, since its implementation in the wind tunnel, the set-up has been characterized by elevated drag results. The reasons are the small gaps between the wing

Commented [D24]: RC2: Additional information on the test section was removed.

Commented [D25]: RC1(Q6minor): The attachment of the wing model to the force balance was specified

Commented [D26]: RC1 (Q5minor): the measurement principle of the inflow velocity was specified.

RC1 (Q7minor): the dimensions of the end plates was included

RC1 (Q8minor): the reference Prandtl tube in front of the airfoil model was removed to avoid confusion

Commented [D27]: RC1(Q6minor): idem

and the end plates leading to suction effects. Moreover, a turbulent BL is formed on the end plates triggering separation on the outer parts of the airfoil model. Both effects are 3D and therefore detected in the form of increased total drag values, see Meyer et al. (2016). For the purpose of this study, a wake rake is designed, constructed and implemented into the test section aiming at 2D drag measurements.

3.2.2 Wake rake

The wake rake method is widely recognized for determining 2D drag coefficients at pre-stall conditions, see Fuglsang et al. (2004).

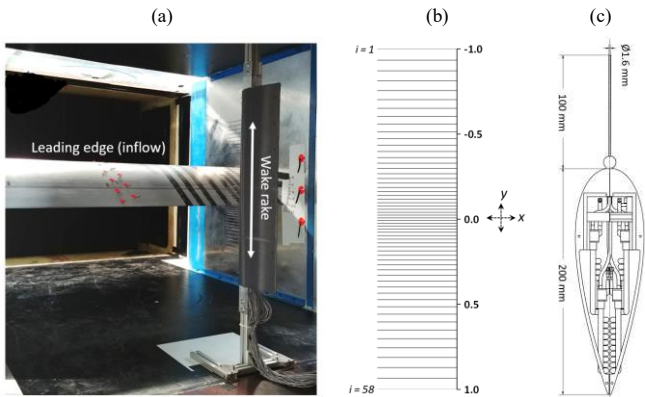


Figure 7. (a) Test section during wind tunnel measurements including airfoil model, one of the end plates and the wake rake. (b) Normalized vertical rake tube positions, y , and numbering, i , in side view. (c) Cross section of wake rake casing and pressure tube in top view.

Figure 7a displays the wake rake, which is positioned at a distance of one chord length, i.e. 0.6 m, downstream of the airfoil trailing edge. According to Barlow et al. (1999), a distance of at least 70% c is necessary for the flow to return to the static pressure level inside the wind tunnel. Figure 7b illustrates that the rake consists of a straight vertical line of 58 pitot tubes, each measuring the total pressure, p_{total} . The normalized vertical positions are defined as $y = 0.0$ for the center, $y_{i=1} = -1.0 = -250$ mm for the uppermost tube and $y_{i=58} = 1.0 = 250$ mm for the lowest tube. The total rake span is 0.5 m. The spacing between the tubes is smallest towards the center with $\Delta y_{\text{min}} = 4$ mm, and widest towards the top and the bottom with $\Delta y_{\text{max}} = 16.5$ mm. The casing consists of a symmetrical NACA0030 profile, see Figure 7c. The distance between the LE and the orifice of each pitot tube is 100 mm, where the impact of the casing on the flow is considered negligible. The static pressure, p_{static} , is determined by means of the static pressure lines of two Prandtl tubes that are installed inside the downstream plane of the wake rake. The differential pressure at each rake tube, $\Delta p(y_i)$, is measured with single pressure sensors that are installed inside the casing. They are connected with flexible silicon tubes, each shorter than 200 mm in order to avoid dynamic feedback effects. The accuracy of each sensor is given with 0.1% of the full scale range of 1000 Pa under nominal conditions. The voltage signal

Commented [D28]: RC1 (Q9minor): the indication of the distance between wake rake and airfoil trailing edge was clarified

Commented [D29]: RC1 (Q10minor): the meaning of this statement was specified

is digitalized by a separate CompactDAQ system at a sampling rate of 10 kHz and recorded by a Labview user interface. After installing each airfoil model, the vertical center of the rake, $y = 0.0$, is aligned with the maximum pressure loss at the corresponding design AoA. In this way, the static rake span covers the complete AoA range, $-5^\circ < \alpha < 17^\circ$, avoiding the installation of a vertical traversing system.

The uncorrected total drag coefficient is determined at each static AoA over an interval of 5s by determining the momentum loss in the wake. According to Barlow et al. (1999),

$$c_{d,raw}(\alpha) = 2 \int \left(\sqrt{\frac{\Delta p_i}{\Delta p_{ref}}} - \frac{\Delta p_i}{\Delta p_{ref}} \right) \frac{dy}{c}, \quad (7)$$

where, Δp_i is the mean differential pressure value in Pa at each rake tube,

$$\Delta p_i = \Delta p(y_i) = \Delta p_{total}(y_i) - \Delta p_{static}, \quad (8)$$

and Δp_{ref} the reference pressure in Pa of the free flow that is taken from the two uppermost and the two lowest rake tubes,

$$\Delta p_{ref} = 0.25 \cdot (\Delta p_1 + \Delta p_2 + \Delta p_{57} + \Delta p_{58}). \quad (9)$$

The pressure coefficient, c_{pi} , is defined as,

$$c_{pi} = \frac{\Delta p_i}{\Delta p_{ref}}, \quad (10)$$

Based on Eq. (7), the uncorrected drag contribution of each rake tube, c_{di} , becomes,

$$c_{di} = \sqrt{c_{pi}} - c_{pi}. \quad (11)$$

The uncorrected total drag coefficient is then numerically integrated over the spacing between the rake tubes using the trapezoid rule,

$$c_{d,raw}(\alpha) = \frac{1}{c} \sum_{i=1}^{58} (c_{di} + c_{di+1}) \cdot (y_{i+1} - y_i), \quad (12)$$

where c is the airfoil chord length and y_i the normalized position of each rake tube, as illustrated in Figure 7b.

The measured lift and drag polars, $c_{l,raw}(\alpha)$ and $c_{d,raw}(\alpha)$, are affected by the wind tunnel walls. The reasons are, first of all, that the solid blockage effect leads to the constriction of the curved streamlines around the airfoil model. Secondly, the wake blockage effect causes the constriction of the curved streamlines in the wake. For the results to be comparable to equivalent open flow conditions, it is necessary to apply wind tunnel corrections, as detailed in Appendix A. In the remainder of this report, the polar data refers to the corrected lift and drag coefficients, $c_l(\alpha)$ and $c_d(\alpha)$.

3.3 Test matrix

The inflow velocity, $u = 40$ m/s, corresponds to a Reynolds number of approximately $1.5 \cdot 10^6$. The free stream turbulence intensity of the empty wind tunnel is estimated by means of a Prandtl tube and is less than 0.3 %. The AoA ranges from $-5^\circ < \alpha < 17^\circ$ in steps of 1° . At each static AoA, there is a buffer of 4 s for the flow to settle, after which data is recorded for another 5 s. Hence, the total number of samples is $n = 5 \cdot 10^4$ for each rake sensor and $n = 2.5 \cdot 10^4$ for the load cells of the force balance. Before each test run, all sensors are subjected to a zero-offset measurement at standstill in order to reduce experimental errors.

The sequence of measurements starts with the clean baseline followed by the three GF configurations, GF025, GF05 and GF1,

Commented [D30]: RC2: This part was rewritten and shortened

Commented [D31]: RC1 (Q12minor): the data reduction process was explained with more clarity

Commented [D32]: RC1 (Q13minor): The basic momentum loss equation that the scrip is based on was included

Commented [D33]: RC1(Q13minor): idem

Commented [D34]: RC2: Sect. 3.2.3. Wind tunnel corrections was shifted to Appendix A to shorten the main part of the report

Commented [D34]: RC2: Sect. 3.2.3. Wind tunnel corrections was shifted to Appendix A to shorten the main part of the report

310 which refer to a GF height of 0.25 %c, 0.5%c and 1%c, respectively. Next, GF1 is removed and the VG array is installed, followed by the combined configurations, VG + GF025, VG + GF05 and VG + GF1. In the next round, ZZ tape is attached and the test matrix is repeated. Each complete cycle, clean and tripped, is measured within less than 24 hours for the environmental conditions to remain as constant as possible.

Commented [D36]: RC2: the designation of the configurations (GF025, etc) were specified with more clarity.

4. Experimental results

315 The presentation of the wind tunnel measurements is focused on the NACA63(3)618 with GFs and the DU97W300 including VGs plus GFs. All results refer to the clean and the tripped cases. They are presented in the form of both the polar curves and the wake pressure fields.

4.1 NACA63(3)618: Gurney flaps

4.1.1 Polar curves

325 Figure 8 shows the clean and the tripped polar curves of the NACA63(3)618. For clarity, characteristic lift and L/D values are summarized in Table 6

Error! Reference source not found.. In the baseline cases, the drag results are valid until stall at $\alpha_{cl,max} = 10.5^\circ$ and the lift curves are measured until the post-stall AoA of 18.5° , see Figure 8a and c. As expected, ZZ tape with $h_{ZZ} = 0.4$ mm manifests itself in a lift decrease, coupled with a significant drag increase. The design point declines from $\alpha_{opt, clean} = 6.4^\circ$ to $\alpha_{opt, ZZ} = 5.4^\circ$ and the corresponding aerodynamic efficiency drops from $L/D_{max, clean} = 109$ to $L/D_{max, ZZ} = 60$, see Figure 8b and d. The clean and the tripped GF configurations are characterized by an increase in both lift and drag throughout the complete pre-stall region. Furthermore, the shape of the polar curves and the stall behaviour is maintained. In the clean cases, L/D_{max} is only marginally improved by GF025 and GF05. Nonetheless, the significant lift increase is expected to be beneficial in terms of the rotor blade performance, as long as L/D (α) is maintained. As such, GF025 provides the preferred results, while GF1 leads to an overall L/D (α) decrease. In the tripped cases, the aerodynamic efficiency is improved independently of the GF height. The reason is the significant expansion of the BL due to forced LE transition, so that larger GFs appear to be more beneficial.

Commented [D37]: RC2: The structure of this chapter was changed to shorten the report. For that, the results were restricted to

- 1.) the NACA63(3)618 with GFs (only) and
- 2.) the DU97W300 with VGs plus GFs

The following parts were moved to the appendices (pls note that the numbering of the sections and Figures has changed as they refer to the previous version of this manuscript):

- Fig. 10 + text
- 4.1.3 Vortex generators plus Mini Gurney flaps (NACA)
- 4.2.2 Mini Gurney flaps (DU97W300)

The following subsections were removed entirely (pls note that the numbering of the sections and Figures has changed as they refer to the previous version of this manuscript):

- Sect. 4.1.1 Baseline (NACA)
- Sect. 4.2.3: Fig. 17+text
- Appendix A and everything that had to do with the third airfoil AH97W174

Commented [D40]: RC1(Q18minor): the fact that the L/D increase is marginal was highlighted

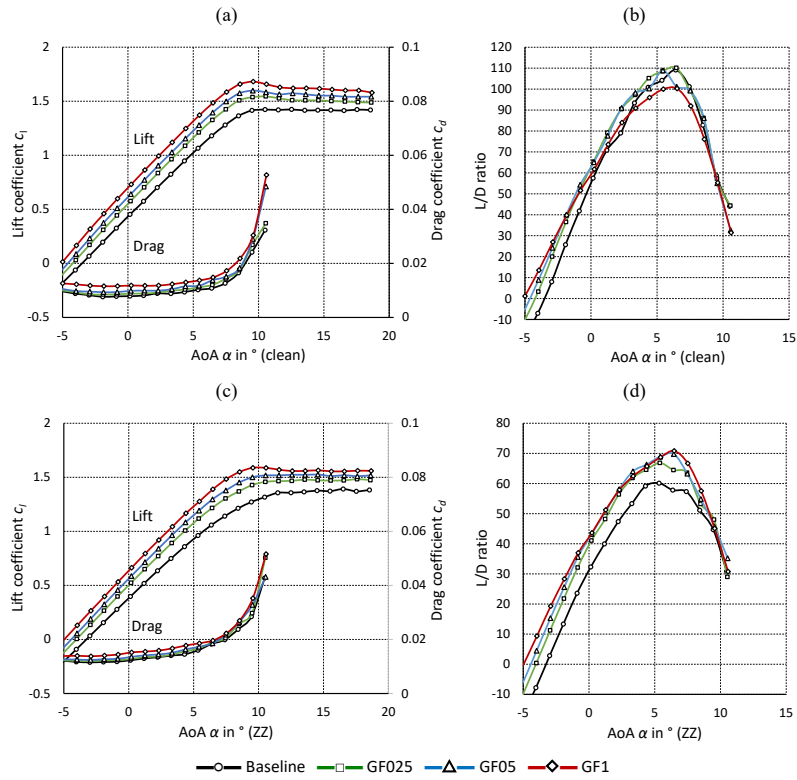


Figure 8. NACA63(3)618. Gurney flaps. (a) Lift and drag coefficients (clean). (b) L/D ratio (clean). (c) Lift and drag coefficients (ZZ). (d) L/D ratio (ZZ).

Table 6. NACA63(3)618. Gurney flaps. Characteristic values.

	Clean		ZZ	
	$c_{l,max}$ (10.5°)	L/D_{max} (6.4°)	$c_{l,max}$ (10.5°)	L/D_{max} (5.4°)
Baseline	1.42	109	1.32	60
GF025	1.54	110	1.46	67
GF05	1.58	101	1.52	69
GF1	1.66	100	1.59	69

345 4.1.2 Wake pressure field

In order to deepen the understanding of the aerodynamic mechanisms, the wake rake data is further evaluated. Figure 9 displays the momentum loss in the wake of the clean and the tripped GF configurations. At $\alpha_{\text{opt}} = 6.4^\circ$, the pressure coefficients, c_{pi} , correspond to attached flow. The pressure deficit and thus drag is increased in relation to the GF height. Moreover, the vertical position of the wake dent is characteristic for the downwash angle, which is proportional to lift. Hence, the minima of the c_{pi} curves descend towards the wind tunnel floor as the GF heights increase. In the tripped case, the pressure deficit and thus drag is more pronounced and the downwash angle is smoother due to lower lift values.

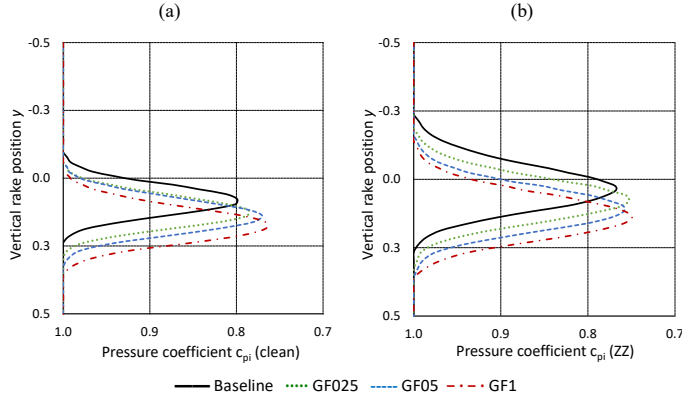


Figure 9. NACA63(3)618 at $\alpha = 6.4^\circ$. Gurney flaps. Pressure coefficients over vertical wake rake positions. (a) Clean case. (b) Tripped case.

Next, the fluctuations of the pressure measurements indicate the intensity of the wake unsteadiness, which is an important contributor to the total drag value. These fluctuations are determined via the standard deviation of the differential pressure data in Pa at each rake tube and each AoA,

$$\sigma_{pi}(\alpha) = \sqrt{\frac{1}{n-1} \sum_{i=1}^n |\Delta p_i(t) - \Delta p_i|^2}, \quad (13)$$

where $n = 5 \cdot 10^4$ is the number of samples of each pressure sensor, $\Delta p_i(t)$ the time resolved differential pressure values in Pa and Δp_i the average differential pressure in Pa at each AoA, see Eq. (8).

Figure 10a shows that, in the clean case, the intensity of the wake unsteadiness is dependent on the GF height. Despite the offset due to the steeper downwash angle, the minima of the c_{pi} curves are similar between the clean baseline and the MGF configurations, as predicted by Bechert et al. (2000) and Schatz et al. (2004b), see Sect. 1.2. In the tripped cases, Figure 10b illustrates that σ_{pi} is more pronounced due to the thicker and more turbulent BL, whereas the relative $\sigma_{pi}(\alpha)$ contribution of the GFs appears to be minor.

Commented [D42]: RC1(Q16minor) and RC2: cross-reference was corrected

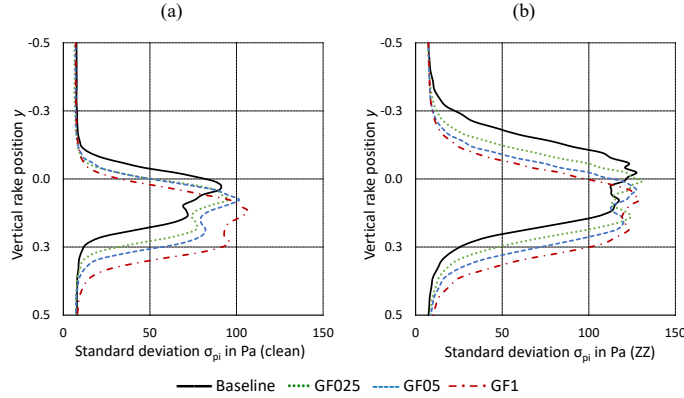


Figure 10. NACA63(3)618 at $\alpha = 6.4^\circ$. Gurney flaps. Standard deviation of raw pressure data over vertical wake rake positions. (a) Clean case. (b) Tripped case.

For completeness, additional NACA63(3)618 results are presented in Appendix B. The polar curves that refer to the combination of VGs plus GFs are included in Appendix B1. Appendix B2 presents the investigation of the different GF shapes, i.e. the rectangular versus the rectangular profiles.

4.2 DU97W300: Vortex Generators plus Gurney flaps

4.2.1 Polar curves

Figure 11 displays the clean and the tripped polar curves of the DU97W300. In the baseline cases, the design AoA is decreased from $\alpha_{\text{opt, clean}} = 9.5^\circ$ to $\alpha_{\text{opt, ZZ}} = 7.4^\circ$ and the stall angle is declined from $\alpha_{\text{cl, max, clean}} = 12.6^\circ$ to $\alpha_{\text{cl, max, ZZ}} = 10.4^\circ$, see Figure 11a and c. Hence, using ZZ tape with $h_{\text{ZZ}} = 0.3$ mm, separation is initiated early, in fact only 1° below $\alpha_{\text{opt, clean}}$. As a result, the aerodynamic efficiency drops from $L/D_{\text{max, clean}} = 88$ to $L/D_{\text{max, ZZ}} = 41$, see Figure 11b and d. For clarity, characteristic lift and L/D values are summarized in Table 7. Looking at the VG (only) cases, stall is delayed by approximately 3° coupled with a substantial increase in maximum lift, see Figure 11a and c. However, the VGs lead to a more abrupt stall behaviour and thus adverse load excursions, as reported by Mueller-Vahl et al. (2012). Despite the improved drag behavior at elevated AoA, the drag penalty causes L/D_{clean} to decrease at low and moderate AoA. Under tripped conditions, the aerodynamic efficiency is only slightly decreased in the lower AoA range. Furthermore, $L/D_{\text{max, ZZ}}$ is significantly increased, as it is shifted by almost 5° recovering a large area of otherwise separated flow between $7.4^\circ < \alpha < 15.6^\circ$, as illustrated in Figure 11d. In the combined cases, the VG is superposed by the GF effect leading to both stall delay and the pre-stall lift increase. Compared to the VG (only) configurations, $L/D(a)$ is therefore maintained in the clean, and slightly improved in the tripped cases.

Commented [D43]: RC1(Q21minor): Paragraph was rewritten to clarify why the VG + GF cases are preferred over the VG (only) configuration

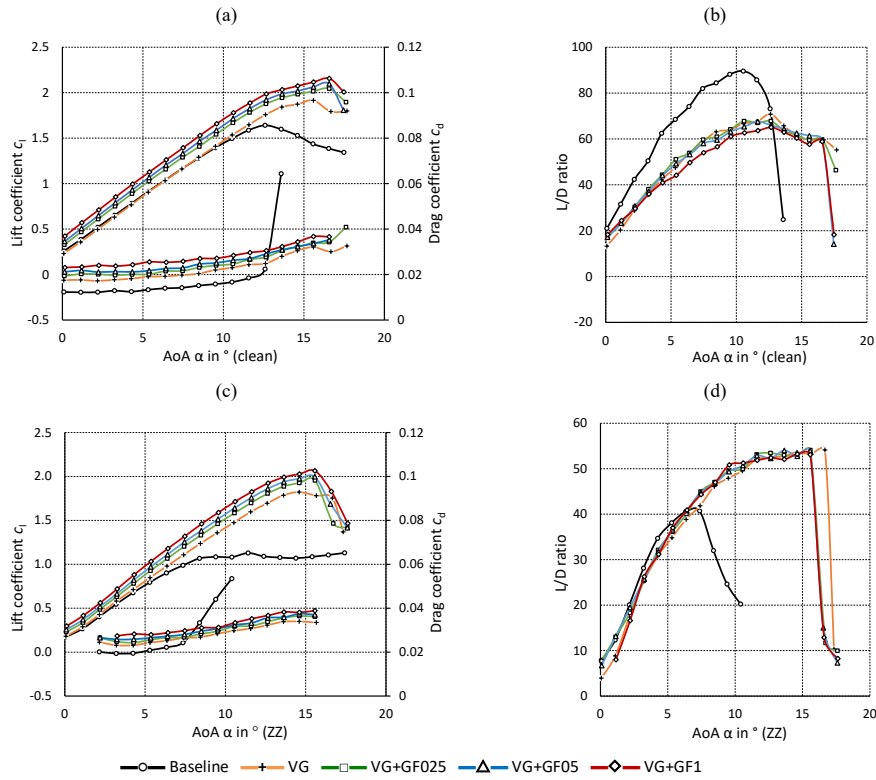


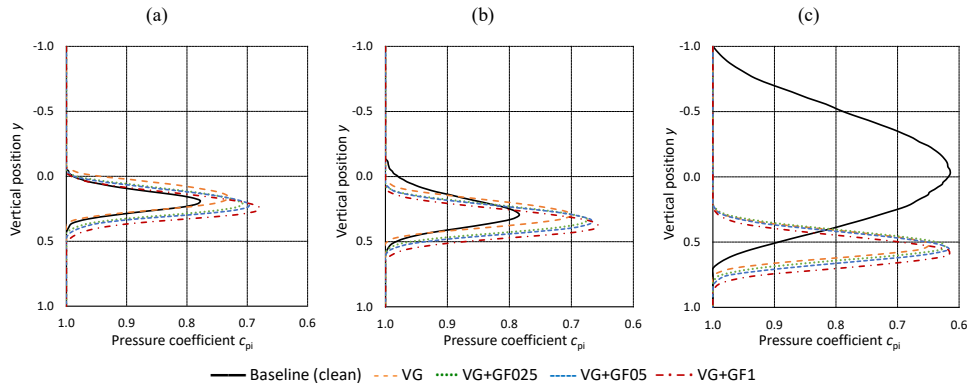
Figure 11. DU97W300. Vortex generators and Gurney flaps. (a) Lift and drag coefficients (clean). (b) L/D ratio (clean). (c) Lift and drag coefficients (ZZ). (d) L/D ratio (ZZ).

Table 7. DU97W300. Vortex generators plus Gurney flaps.

	Clean		ZZ	
	$c_{l,max}(\alpha)$	$L/D_{max}(\alpha)$	$c_{l,max}(\alpha)$	$L/D_{max}(\alpha)$
Baseline	1.64 (12.6°)	88 (9.5°)	1.13 (11.4°)	41 (7.4°)
VG	1.91 (15.6°)	71 (12.6°)	1.82 (14.6°)	52 (12.6°)
VG+GF025	2.04 (16.6°)	68 (12.6°)	1.96 (15.6°)	53 (12.6°)
VG+GF05	2.10 (16.6°)	66 (12.6°)	2.00 (15.6°)	52 (12.6°)
VG+GF1	2.16 (16.6°)	65 (12.6°)	2.06 (15.6°)	52 (12.6°)

4.2.2 Wake pressure field

395 In order to deepen the understanding of the aerodynamic mechanisms, the wake rake data is further evaluated. Figure 12a displays the pressure loss in the wake of the clean VG + GF configurations. At $\alpha_{\text{opt, clean}} = 9.5^\circ$, the pressure coefficients, c_{pi} , correspond to attached flow. At $\alpha = 12.6^\circ$, the wake deficit of the baseline curve extends towards the upper side of the rake indicating the formation of the TE separation bubble on the suction side and thus the initiation of stall, see Figure 12b. The curves of the VG + GF configurations, on the other hand, show that the flow remains attached.



400 Figure 12. DU97W300. Pressure coefficients over vertical wake rake positions in the clean case. Vortex generators and Gurney flaps. (a) $\alpha_{\text{opt}} = 9.5^\circ$. (b) $\alpha_{\text{cl,max}} = 12.6^\circ$. (c) $\alpha = 16.5^\circ$.

At $\alpha = 16.5^\circ$, the baseline airfoil is clearly stalling, see Figure 12c. At this point, the wake consists of separated flow, i.e. 3D structures that cannot be determined by means of the wake rake. As opposed to that, the VG configurations **delay** the formation of stall cells, so that the flow remains attached, as described by Manolesos and Voutsinas (2015). Finally, at $\alpha = 17.5^\circ$, which is not displayed here, the flow separates abruptly leading to a steep decline of the lift curves. These load excursions are perceptible in the form of strong mechanical vibrations of the setup as well as a deep roaring sound inside the wind tunnel. The wake deficit remains similar in shape and amount comparing the VG (only) to the combined configurations, again pointing towards a favorable wake interaction between VGs and MGFs.

410 For completeness, additional DU97W300 results are presented in Appendix C. The validation of the experimental setup is compared to wind tunnel measurements of the DU in Appendix C1. The polar curves that refer to the GF (only) configurations are included as Appendix C2.

Commented [D49]: RC1 (Q19minor): "suppress" was replaced by "delay"

5. Rotor blade performance

The preferred configurations of VGs and GFs are selected on the basis of the wind tunnel measurements. The experimental polar data is imported into the software QBlade (Marten, 2020) in order to create a generic rotor blade. The blade performance is simulated by means of two case studies, the retrofit application on an existing, and the new design application on an alternative rotor blade design.

5.1 Blade configurations

Table 8 summarizes the qualitative effect of the preferred MGF (only) and MGF + VG configurations including $h_{MGF} = 0.25\%$ and $h_{MGF} = 0.5\%$. It is noted that $h_{GF} = 1.0\%$ is not considered relevant for this section due to the elevated drag penalty and thus L/D decrease.

Table 8. Performance evaluation of MGFs and VGs based on the wind tunnel tests of the NACA63(3)618 and the DU97W300. ↑ for increase, ≈ for similar and ↓ for decrease.

	Clean			ZZ		
MGFs (only)	$c_l(\alpha) \uparrow$	$\alpha_{cl,max} \approx$	$L/D_{max} \approx$	$c_l(\alpha) \uparrow$	$\alpha_{cl,max} \approx$	$L/D_{max} \uparrow$
VG + MGF	$c_l(\alpha) \uparrow$	$\alpha_{cl,max} \uparrow$	$L/D_{max} \downarrow$	$c_l(\alpha) \uparrow$	$\alpha_{cl,max} \uparrow$	$L/D_{max} \uparrow$

Commented [D50]: RC2: the readability of Table was improved.

First of all, the effect of both PFC devices is case dependent, as illustrated in Table 8. Apart from that, it is difficult to measure and to foresee the degree of LER, as described by Papi et al. (2021). Hence, the principal objective of this study is to improve the airfoil performance based on forced LE transition without jeopardizing the aerodynamic efficiency of the clean airfoil. Looking at the MGF (only) configurations, lift is increased at the design point and the stall behavior is consistent. The decambering effect of the ZZ tape is partly recovered, as such improving the aerodynamic efficiency, while $L/D_{max, clean}$ is maintained. Next, VG + MGF lead to significant improvements regarding both the lift increase and the stall delay. In the clean case, $L/D_{max, clean}$ is decreased due to the combined drag penalty. In the tripped case, however, the combined configurations achieve a triple improvement in terms of lift increase, stall delay and aerodynamic efficiency.

In conclusion, GF025 is selected over GF05 because it is the more conservative option, especially in the clean case of the NACA63(3)618. Regarding the DU97W300, VG + GF05 is the preferred option due to both the significant stall delay and the pre-stall lift increase. It is noted that either of the MGF configurations, GF025 and GF05, lead to similar results indicating a certain tolerance in choosing the optimum MGF height in accordance with Eq. (4).

5.2 Blade design

The experimental lift and drag polars are imported into the open source software QBlade. Figure 13 illustrates the rotor blade of the NREL 5 MW reference wind turbine, as specified by Jonkman et al. (2009). The total rotor radius is $R = 63$ m, the average wind speed at hub height is $u = 8$ m/s. The design tip speed ratio (TSR), $\lambda(R) = \lambda_{opt} = 8$ is defined as

$$\lambda(r) = \frac{2\pi f r}{u}, \quad (14)$$

where f is the rotational frequency in Hz.

The NREL blade is used as a template for the so-called generic rotor blade design, which is scaled down to $R = 20$ m, $u = 7$ m/s and $\lambda_{opt} = 7$. The resulting Reynolds numbers are closer to those of the wind tunnel tests, i.e. in the range of $1.5 \cdot 10^6$ to $2 \cdot 10^6$ rather than $3 \cdot 10^6$ to $9 \cdot 10^6$.

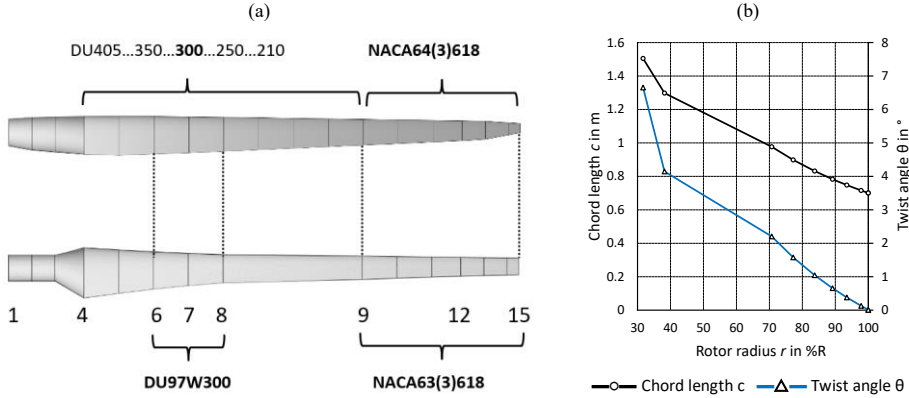


Figure 13. (a) Design of the generic rotor blade based on the NREL 5 MW reference wind turbine. (b) Geometry of the generic blade over the rotor radius.

Figure 13a shows that the DU97W300 is placed from blade position 6 to 8 and the NACA63(3)618 between position 9 and 15. The mid span region, see position 8 to 9, is simply interpolated for the purpose of this numerical part. Figure 13b shows the chord length $c(r)$ and the twist angle $\theta(r)$ at each blade position, which are determined by means of the blade optimization procedure of Schmitz (1956), as described by Gasch and Twele (2012),

$$c(r) = \frac{16\pi r}{B \cdot c_l(\alpha_{opt})} \sin^2 \left[\frac{1}{3} \tan^{-1} \left(\frac{R}{\lambda_{opt} \cdot r} \right) \right], \quad (15)$$

$$\theta(r) = \varphi - \alpha_{opt} = \frac{2}{3} \tan^{-1} \left(\frac{R}{\lambda_{opt} \cdot r} \right) - \alpha_{opt}, \quad (16)$$

where B is the number of blades and φ the inflow angle in $^\circ$.

Commented [D51]: RC1(Q20minor): the position of legend was fixed

Commented [D52]: RC2: Paragraph was shortened.

The Schmitz design leads to elevated chord lengths and twist angles in the root region due to the decreasing rotational speed and thus $\lambda(r)$ towards the blade root. For practical and logistical reasons, $c(r < 30\%R)$ is usually designed separately in order to limit the volume and the weight of large rotor blades. Hence, the numerical results of the generic blade are only feasible between position 6 at $r = 31.7\%R$ and the tip. Besides, no specific tip design is implemented. Next, two case studies are defined and presented based on Eq. (15) and (16). The first one is the retrofit application, i.e. the PFC devices are installed on an existing rotor blade, for instance during regular maintenance activities. The original blade design is based on the smooth surface, i.e. the clean airfoil polars. Over time, LER occurs and the data files of the clean are replaced by the tripped baseline. As a consequence, the aerodynamic efficiency and therefore the AEP is decreased. During the third step, the polar data of both VGs and MGFs is imported in order to recover some of the power output, as illustrated in Figure 14.

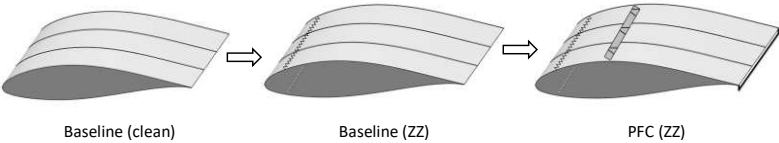


Figure 14. Retrofit application of passive flow control devices on a generic rotor blade section.

The second case study is the new design application. The PFC devices are installed as part of the blade manufacturing process on the ground. The performance of the clean and the tripped baseline blade, as previously depicted in Figure 14, is compared to an alternative configuration that includes the PFC devices as part of the design process itself. Hence, the blade geometry, $c(r)$ and $\theta(r)$, is calculated separately for the alternative blade, PFC* (clean) and PFC* (ZZ), see Figure 15.

Commented [D53]: RC2: Paragraph was shortened.

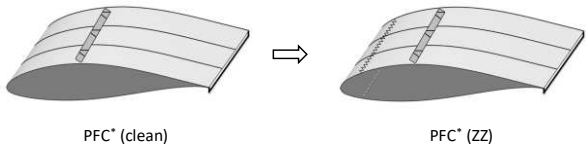


Figure 15. New design application of passive flow control devices on a generic rotor blade section.

5.3 Blade simulations

The rotor blade simulations are performed using the steady Blade Element Momentum (BEM) method based on Hansen (2015), which is embedded into QBlade, v99. The BEM simulations entirely depend on the quality of the imported polar data at each blade section, see Figure 13a. Furthermore, empirical correction algorithms are activated, including root and tip loss calculations, thrust forces of heavily loaded rotors (Glauert correction) and spanwise crossflow effects, as described by Marten et al. (2013). The power curves are determined with respect to the rated power output of $P_{\max} = 600 \text{ kW}$ at $u = 12 \text{ m/s}$. The basic pitch and rpm controller settings are optimized for reaching maximum power output.

Commented [D54]: RC2: the following sentences were removed

5.3.1 Retrofit application

The BEM simulations of the retrofit application are presented. Figure 16 shows the AoA along the local rotor radius, r . The clean baseline coincides with $\alpha_{\text{opt, clean}} = 9.5^\circ$ of the DU97W300 in the root, and $\alpha_{\text{opt, clean}} = 6.4^\circ$ of the NACA63(3)618 in the tip region. Replacing the clean by the tripped polar data, the AoA are significantly increased, see Figure 16a. In fact, the root region is already stalling for $\alpha > 10.5^\circ$, so that the local L/D drops dramatically, see Figure 16b. This adverse effect of forced LE transition is partly compensated for by the PFC devices. Hence, the AoA are closer to $\alpha_{\text{opt, clean}}$ and the $L/D(r)$ is partly recovered. Figure 16c shows the power coefficients over the complete operational range of the rotor. In the tripped case, the power curve is shifted towards higher TSR leading to $\lambda(c_{p, \text{max, ZZ}}) = 8$ rather than $\lambda_{\text{opt}} = 7$. As a result, $c_{p, \text{max, clean}}(\lambda_{\text{opt}}) = 0.48$ is decreased by 13 % to $c_{p, \text{max, ZZ}}(\lambda_{\text{opt}}) = 0.42$. After the retrofit application, the c_p curve is closer to the design point with $c_{p, \text{max, PFC}}(\lambda_{\text{opt}}) = 0.45$, reducing the relative power loss to 5.7 %. In this generic case study, the power loss due to forced LE transition is approximately halved by the retrofit application of MGFs and VGs.

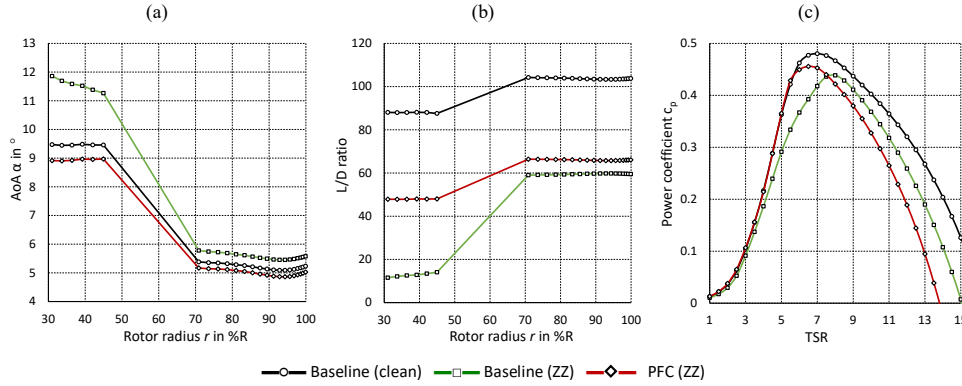


Figure 16. Rotor blade performance simulation of baseline and retrofit application. (a) AoA over rotor radius at $\lambda_{\text{opt}} = 7$. (b) L/D over rotor radius at $\lambda_{\text{opt}} = 7$. (c) Power coefficients over TSR.

5.3.2 New design application

The BEM results of the new design application are presented. According to Eq. (15), the lift increase caused by the MGFs, see Figure 17a, leads to a significant chord length reduction. Comparing the baseline cases, the optimum chord length is reduced by 23.4 % in the root and by 12 % in the tip region, as illustrated in Figure 17b. Regardless of the structural-dynamic considerations, this approach might contribute to the development of more slender blades and thus saving material costs, as previously suggested by Fuglsang et al. (2004), see Sect. 1.5. Moreover, periodic gravitational load alternations as well as fatigue loads are potentially mitigated by reducing the blade weight.

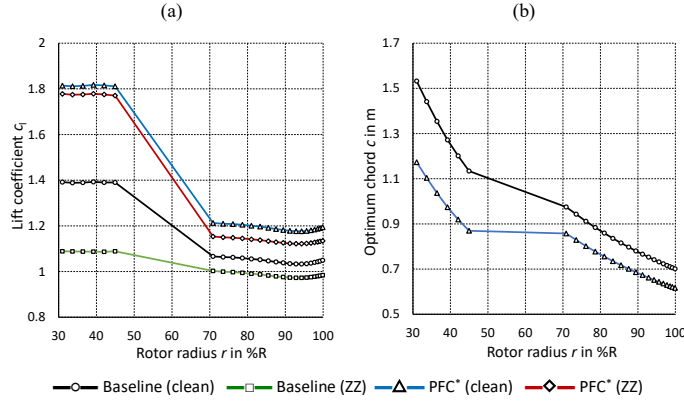


Figure 17. Blade geometry of baseline and new design application at $\lambda_{\text{opt}} = 7$. (a) Lift coefficients over rotor radius (b) Optimum chord length over rotor radius.

Next, Figure 18 shows the BEM simulation of the new design application. It is noted that the clean and tripped baseline curves, Baseline (clean) and Baseline (ZZ), are identical to previous Figure 16. First of all, PFC* (clean) and PFC* (ZZ) lead to similarly high design AoA, $\alpha_{\text{opt,PFC}} \approx 12^\circ$ towards the root, see Figure 18a. Apart from that, stall is delayed by the VGs until approximately 16° , which is not shown here. In the tip region, the MGF only leads to a marginal increase regarding α (λ_{opt}). Figure 18b illustrates that, in the clean case, the aerodynamic efficiency is decreased towards the root region due to the drag penalty of the PFC devices, whereas the MGF achieves a slight L/D improvement towards the tip. In contrast to that, the PFC* (ZZ) improves the aerodynamic efficiency significantly throughout the complete blade length, as compared to Baseline (ZZ). Hence, the PFC* configuration appears to be less sensitive to forced LE transition. Next, Figure 18c shows the corresponding power curves. In both PFC* (clean) and PFC* (ZZ), $c_{p,\text{max}}$ remains at $\lambda_{\text{opt}} = 7$. As a consequence, $c_{p,\text{max}} = 0.48$ is almost identical compared to Baseline (clean), despite moderate differences at elevated TSR for $\lambda > \lambda_{\text{opt}}$. In the tripped cases, $c_{p,\text{max}}(\lambda_{\text{opt}}) = 0.45$ is reduced by only 4.6 % relating PFC (ZZ) to PFC (clean) rather than by 13 % with regards to the baseline cases. Again, the power loss due to forced LE transition is at least halved and the rotor blades are significantly more slender due to the new design application of MGFs and VGs.

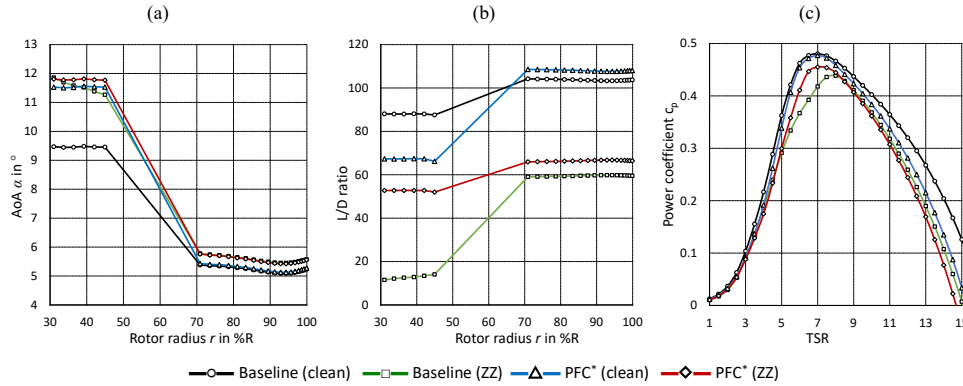


Figure 18. Rotor blade performance simulation of baseline and new design application. (a) AoA over rotor radius at $\lambda_{opt} = 7$. (b) L/D over rotor radius at $\lambda_{opt} = 7$. (c) Power coefficients over TSR.

6 Conclusions

Commented [D55]: RC2: The conclusions were revised.

520 This study investigates the use of mini Gurney flaps and their combination with vortex generators for improved rotor blade performance of wind turbines. GFs and VGs are well-studied PFC devices. However, to the authors' knowledge, there are no scientific papers investigating MGF heights smaller than 0.5%c and their combination with VGs on dedicated wind turbine airfoils. This report contributes in closing these research gaps.

Commented [D56]: Q1(major): idem. (The novelty of this study was highlighted in comparison to the given references)

525 For that, wind tunnel tests are conducted using the NACA63(3)618 and the DU97W300. Lift and drag are measured by means of a force balance and a wake rake, respectively. The baseline results are successfully validated against literature data. The impact of MGFs and VGs on the polar curves depends on whether transition is free or fixed on the airfoils. The configurations with just the MGFs increase the lift performance under pre-stall conditions. Furthermore, the aerodynamic efficiency is maintained in the clean, and improved in the tripped case. Looking at the combined configurations, the VG effect is superposed
530 by the MGF effect, leading to both stall delay and the pre-stall lift increase. In the clean case, the aerodynamic efficiency is decreased due to the combined drag penalty, whereas in the tripped case, it is significantly improved. Furthermore, VGs coupled with MGFs are preferred over the VG (only) configuration due to the additional pre-stall lift increase.

The experimental polar data is imported into the software QBlade in order to design and to simulate a generic rotor blade. The
535 NACA63(3)618 is equipped with the smallest MGF height of 0.25%c in the tip region. The medium size MGF of 0.5 %c and the VG height of 1.1 %c are both attached to the DU97W300 in the root region. The BEM simulations are based on two case studies, the retrofit application on an existing, and the new design application on an alternative blade configuration. The retrofit

application alleviates the adverse effects of forced leading edge transition. Separation is delayed in the root region and the aerodynamic efficiency and thus power output is recovered towards the tip region. The new design application leads to a more slender blade while maintaining the rotor power. Again, the alternative blade appears to be more resistant against leading edge roughness effects.

Further research on MGFs and their interaction with VGs is recommended, especially considering leading edge roughness effects and erosion. Next steps involve the design of sub boundary layer VGs in conjunction with MGFs to further reduce the drag penalty. Moreover, a complete aeroelastic simulation is required, especially regarding open field tests of MGFs in combination with VGs on large wind turbine rotor blades.

Appendix A: Wind tunnel corrections

Following from the experimental setup, see Sect. 3.2, the calculation of the wind tunnel wall effects on the uncorrected lift and drag polars, $c_{l,raw}(\alpha)$ and $c_{d,raw}(\alpha)$, is summarized. According to Barlow et al. (1999), the wind tunnel blockage, ε , is the sum of the solid and the wake blockage factors,

$$\varepsilon = \varepsilon_{solid} + \varepsilon_{wake} = \Lambda\mu + \frac{c}{4h_{wt}}c_{d,raw}, \quad (17)$$

where Λ refers to the so-called body shape factor, which is a function of the maximum airfoil thickness and h_{wt} is the height of the wind tunnel. For clarity, $\mu = \frac{\pi^2}{48} \left(\frac{c}{h_{wt}} \right)^2$ is introduced as an auxiliary constant.

Based on Eq. (17), the solid and the wake blockage correction is applied on the following parameters at each static AoA,

$$c_d = c_{d,raw}(1 - 3\varepsilon_{solid} - 2\varepsilon_{wake}), \quad (18)$$

$$c_l = c_{l,raw}(1 - \mu - 2\varepsilon), \quad (19)$$

$$Re = Re_{raw}(1 + \varepsilon), \quad (20)$$

$$\alpha = \alpha_{raw} + \frac{57.3\mu}{2\pi}(c_{l,raw} + 4c_{m,raw}), \quad (21)$$

$$c_m = c_{m,raw}(1 - 2\varepsilon) + 0.25\mu c_l, \quad (22)$$

where c_m refers to the moment coefficient at 0.25c.

Eq. (18) to (22) are embedded into the data post-processing script.

Appendix B: NACA63(3)618

B1. Vortex generators plus Gurney flaps

Figure 19 shows the polar curves of the VG + GF configurations based on the NACA63(3)618. As presented in Sect. 4.2.1, the VG is superposed by the GF effect, leading to both stall delay and pre-stall lift increase. Compared to the corresponding

Commented [D57]: RC2: All Appendices were reorganized

560 VG (only) configurations, L/D (a) is maintained in the clean, and slightly improved in the tripped cases. For clarity, characteristic lift and L/D values are summarized in Table 9.

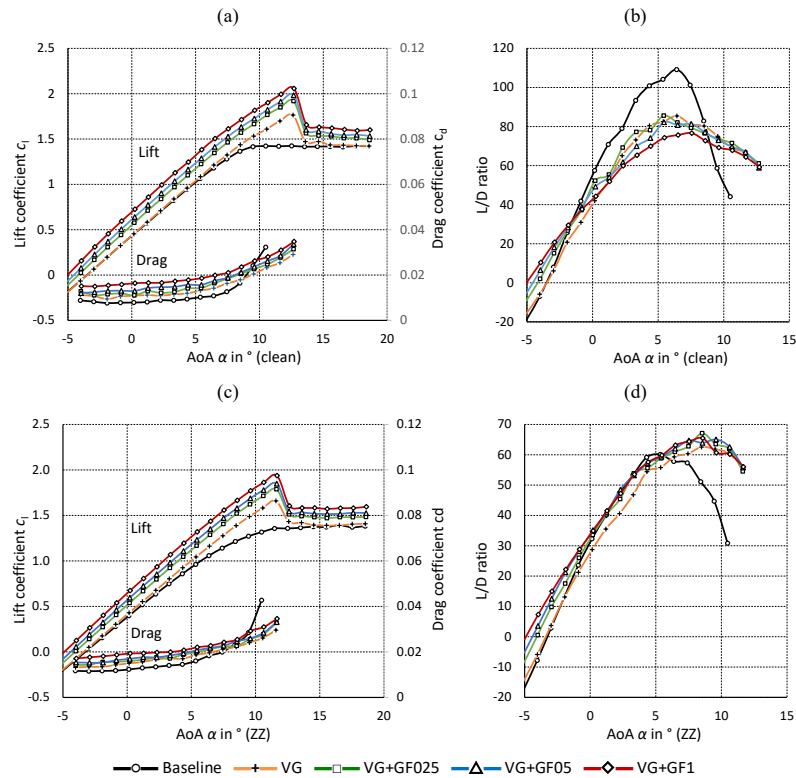


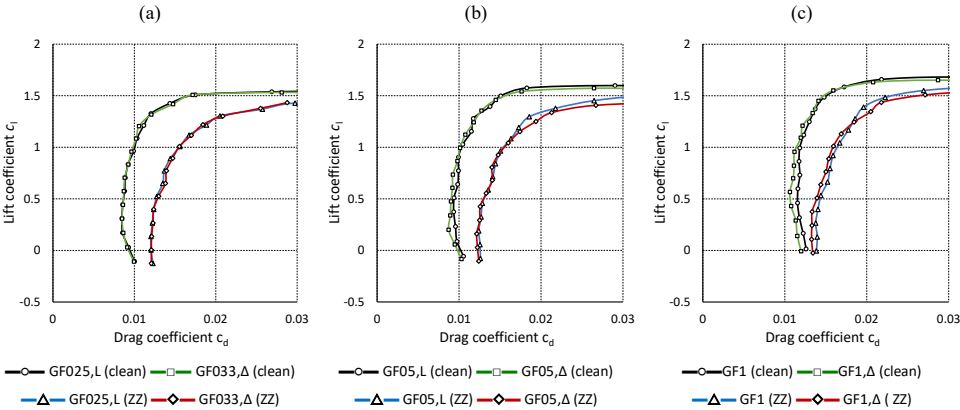
Figure 19. NACA63(3)618. Vortex generators and Gurney flaps. (a) Lift and drag coefficients (clean). (b) L/D ratio (clean). (c) Lift and drag coefficients (ZZ). (d) L/D ratio (ZZ).

565 Table 9. NACA63(3)618. Vortex generators plus Gurney flaps. Characteristic values.

	Clean		ZZ	
	$c_{l,max}(\alpha)$	$L/D_{max}(\alpha)$	$c_{l,max}(\alpha)$	$L/D_{max}(\alpha)$
Baseline	1.42 (10.5°)	109 (6.4°)	1.32 (10.5°)	60 (5.4°)
VG	1.76 (12.7°)	85 (6.4°)	1.66 (11.6°)	63 (8.5°)
VG+GF025	1.92 (12.7°)	82 (6.4°)	1.79 (11.6°)	67 (8.5°)
VG+GF05	1.98 (12.7°)	81 (6.4°)	1.85 (11.6°)	64 (8.5°)
VG+GF1	2.06 (12.7°)	76 (6.4°)	1.94 (11.6°)	65 (8.5°)

B2. Rectangular versus triangular Gurney flaps

570 Timmer and van Rooij (2003) as well as Fuglsang et al. (2003) reported that rectangular and triangular GFs of identical height generate very similar aerodynamic effects, apart from minor differences in drag. In order to verify this observation, the NACA63(3)618 is equipped with angle sections made of brass versus isosceles triangles made of thermoplastic material, see Figure 1a. In Figure 20, the lift over the drag coefficients are compared in both the clean and the tripped cases looking at each GF configuration separately. It is noted that the smallest triangular size, $h_{MGF,\Delta} = 0.33\%$ is larger than the corresponding rectangular profile, $h_{MGF,L} = 0.25\%$. In all cases, the triangular or wedge shaped profiles show a slight decrease in both lift and drag, see Figure 20b and c. Apart from that, the effect on the airfoil polars is very similar between both GF profiles.



575 Figure 20. NACA63(3)618. Rectangular (L) versus triangular (Δ) Gurney flap profiles. Lift over drag curves in clean and tripped cases (a) $h_{MGF,L} = 0.25\%$ and $h_{MGF,\Delta} = 0.33\%$. (b) $h_{MGF} = 0.5\%$. (c) $h_{GF} = 1\%$.

Appendix C: DU97W300

C1. Data validation

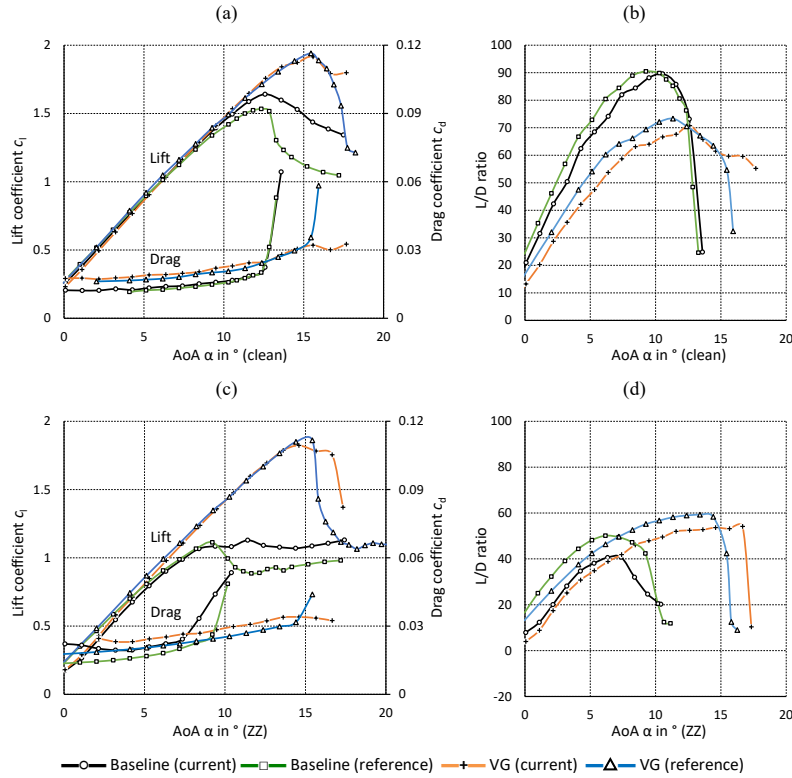
The baseline and the VG measurements of the DU97W300 are compared to reference data in order to validate the experimental setup. Baldacchino et al. (2018) performed similar experiments in the low turbulence wind tunnel of the DU. The airfoil chord length was $c = 0.65$ m (here 0.6 m) and $Re = 2 \cdot 10^6$ (here: $Re = 1.5 \cdot 10^6$) with a free stream turbulence intensity of below 0.1% (here: 0.3 %). Lift was determined from surface pressure measurements and drag by means of a wake rake, which was positioned at a distance of 60 %c (here 100%c) away from the airfoil TE. Forced LE transition was triggered by means of ZZ tape with $h_{ZZ} = 0.17$ mm at $x_{ZZ} = 5.0$ %c on the suction side, as opposed to the more aggressive tripping of the current setup with $h_{ZZ} = 0.3$ mm on both the suction and the pressure side. The VG configurations included $h_{VG} = 0.77$ %c and $D = 7h_{VG}$ at $x_{VG} = 30$ %c, as compared to the current setup with $h_{VG} = 1.1$ %c. Figure 21 shows the direct comparison between the polar data. For clarity, characteristic lift and L/D values are summarized in Table 10.

Figure 21a and c show very good agreement between the lift curves of both the baseline and the VG configurations. However, the stall behaviour is smoother looking at the current measurements. In the clean case, drag is elevated compared to the reference data leading to slightly decreased L/D (α) curves. The main reasons are the differences in the Reynolds number and the inflow turbulence intensity. Furthermore, due to the larger VG height, drag is slightly higher in the pre-stall region, as compared to the DU measurements. In the tripped case, the more pronounced differences in both c_d (α) and thus L/D (α) are due to the more aggressive tripping of the current setup. Overall, the results are in very good agreement with the reference data, as highlighted in Table 10.

Table 10. DU97W300. Characteristic values. Reference data is adopted from Baldacchino et. al (2018)

	Clean		ZZ	
	$c_{l,max}(\alpha)$	$L/D_{max}(\alpha)$	$c_{l,max}(\alpha)$	$L/D_{max}(\alpha)$
Baseline	1.64 (12.6°)	88 (9.5°)	1.13 (11.4°)	41 (7.4°)
Baseline (reference)	1.53 (12.4°)	90 (9.3°)	1.11 (9.2°)	50 (6.2°)
VG	1.91 (15.6°)	71 (12.6°)	1.82 (14.6°)	52 (12.6°)
VG (reference)	1.94 (15.5°)	73 (11.3°)	1.86 (15.4°)	59 (13.4°)

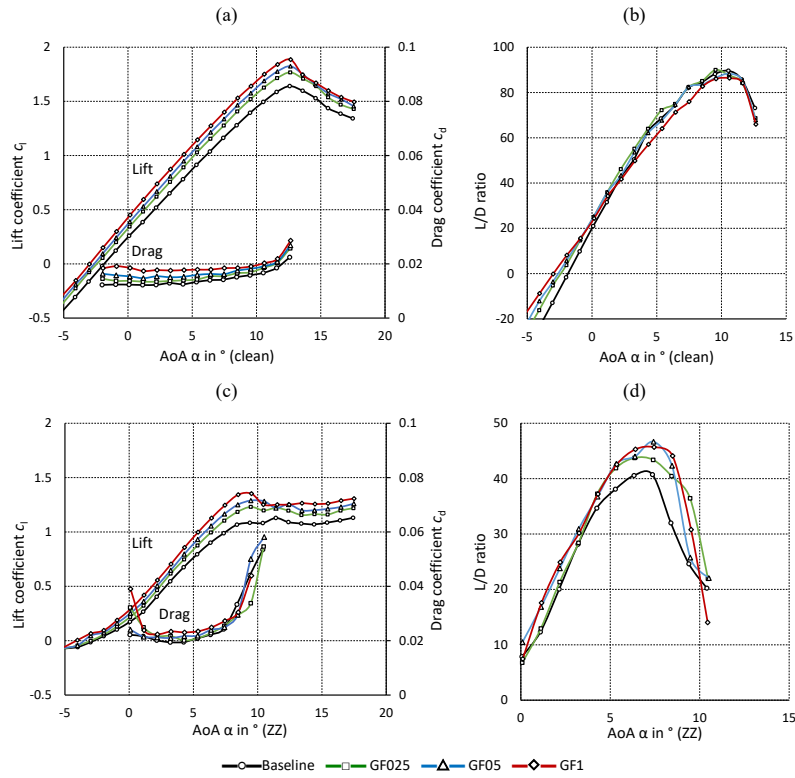
Commented [D58]: RC2: The validation of the measurement results were restricted to one airfoil. The results of the NACA validation was deleted.



605 Figure 21. DU97W300. Clean and tripped cases. Baseline and VG configurations at $Re = 1.5 \cdot 10^6$ compared to reference data from Baldacchino et al. (2018) at $Re = 2 \cdot 10^6$. (a) Lift and drag coefficients. (b) Lift to drag ratio.

C2. Gurney flaps

Figure 22 shows the polar curves of the GF configurations based on the DU97W300. As presented in Sect. 4.1.1, the increase in both lift and drag depends on the GF height and the shape of the polar curves is basically maintained. Furthermore, the beneficial GF effect on the aerodynamic efficiency is more pronounced in the tripped case. Figure 22b shows that, in the clean case, $L/D(\alpha)$ is maintained applying either of the MGFs, whereas it is decreased using the GF1. According to Figure 22d, the performance deterioration due to forced LE transition is alleviated by all GFs, with GF05 achieving the preferred results in terms of $L/D_{ZZ}(\alpha)$. For clarity, characteristic lift and L/D values are summarized in Table 11.



615 Figure 22. DU97W300. Gurney flaps. (a) Lift and drag coefficients (clean). (b) L/D ratio (clean). (c) Lift and drag coefficients (ZZ). (d) L/D ratio (ZZ).

Table 11. DU97W300. Gurney flaps. Characteristic values.

	Clean		ZZ	
	$c_{l,max}(12.6^\circ)$	$L/D_{max}(9.5^\circ)$	$c_{l,max}(10.4^\circ)$	$L/D_{max}(7.4^\circ)$
Baseline	1.64	88	1.08	41
GF025	1.77	90	1.20	43
GF05	1.82	87	1.28	47
GF1	1.89	86	1.25	46

Data availability.

Measurement data and results can be provided by contacting the corresponding author.

620 Author contribution

Johannes Fischer designed and fabricated the wake rake and the vortex generators. Jörg Alber validated the wake rake measurements and designed the Gurney flaps. Jörg Alber, Marinos Manolesos, Guido Weinzierl-Dlugosch, Johannes Fischer and Alexander Schönmeier prepared and conducted the wind tunnel experiments. Jörg Alber performed the airfoil and rotor blade simulations. Jörg Alber and Alexander Schönmeier processed the experimental and numerical data. Jörg Alber wrote the manuscript and managed the review process, with the support of all co-authors.

Competing interests

The authors declare that they have no conflict of interest.

Acknowledgements

The authors would also like to appreciate the constant support of the technicians of the Hermann-Föttinger Institut at the Technische Universität Berlin.

References

- Abbott, I.H., and von Doenhoff, A.E.: Theory of Wing Sections, Dover publications, Inc. New York, ISBN 100486605868, 1959.
- Alber, J., Pechlivanoglou, G., Paschereit, C. O., Twele, J., and Weinzierl, G.: Parametric Investigation of Gurney Flaps for the Use on Wind Turbine Blades, in: Proceedings of the ASME Turbo Expo 2017, Volume 9, Wind Energy, Charlotte, North Carolina, USA, Paper GT2017-64475, <https://doi.org/10.1115/GT2017-64475>, June, 2017.
- Bach, A. B., Lennie, M., Pechlivanoglou, G., Nayeri, C. N. and Paschereit, C. O.: Finite micro-tab system for load control on a wind turbine, Journal of Physics: Conference Series, Volume 524, <http://dx.doi.org/10.1088/1742-6596/524/1/012082>, 2014.
- Bak, C., Skrzypiąski, W., Fischer, A., Gaunaa, M., Brønnum, N. F. and Kruse, E. K.: Wind tunnel tests of an airfoil with 18% relative thickness equipped with vortex generators, Journal of Physics: Conference Series, Volume 1037, Issue 2, <http://dx.doi.org/10.1088/1742-6596/1037/2/022044>, 2018.
- Bak, C., Skrzypiąski, W., Gaunaa, M., Villanueva, H., Brønnum, N. F. and Kruse, E. K.: Full scale wind turbine test of vortex

generators mounted on the entire blade, Journal of Physics: Conference Series, Volume 753, Issue 2,
645 <http://dx.doi.org/10.1088/1742-6596/753/2/022001>, 2016.

Bak, C., Zahle, F., Bitsche, R., Kim, T., Yde, A., Henriksen, L. C., Natarajan, A., and Hansen, M.: Description of the DTU 10
MW Reference Wind Turbine, Technical University of Denmark, DTU Wind Energy Report-I-0092, June 2013.

Baldacchino, D., Ferreira, C., de Tavernier, D., Timmer, W. A. and van Bussel, G. J. W.: Experimental parameter study for
passive vortex generators on a 30% thick airfoil, Wind Energy. 2018, Vol. 21, p. 745-765,
650 <https://doi.org/10.1002/we.2191>, 2018.

Barlas, T.K., Kuik, van G. A. M.: Review of state of the art in smart rotor control research for wind turbines, Progress in
Aerospace Sciences, Vol. 46, Issue 1, p. 1-27, ISSN 0376-0421, <https://doi.org/10.1016/j.paerosci.2009.08.002>, 2010.

Barlow, J. B., Rae, W. H. and Pope, A.: Low-Speed Wind Tunnel Testing, John Wiley & Sons, 3rd edition, USA,
<https://doi.org/10.2514/2.633>, 1999.

655 Bechert, D. W., Meyer, R., and Hage, W.: Drag reduction of airfoils with miniflaps – Can we learn from dragonflies?, AIAA
Fluids 2000 Conference and Exhibit, Denver, USA, Paper 2000-2315, <https://doi.org/10.2514/6.2000-2315>, June
2000.

Bechert, D., Meyer, R., and Hage, W.: Airfoil with performance enhancing trailing edge, Europäische Patentschrift, Patent
Number: 01250001.3, Date of Patent: 2nd of January 2001.

660 Boyd, J. A.: Trailing edge device for an airfoil, United States Patent, Patent Number: 4,542,868, Date of Patent: 24th of
September, 1985.

Brink, am B. K.: Trailing edge wedge for an aircraft wing, United States Patent, Patent Number: US 6,382,561 B1, Date of
Patent: 7th of May 2002.

Cole, J. A., Vieira, B. A. O., Coder, J. G., Premi, A. and Maughmer, M. D.: Experimental Investigation into the Effect of
665 Gurney Flaps on Various Airfoils, Journal of Aircraft, Vol. 50, No. 4, <https://doi.org/10.2514/1.C032203>, 2013.

Drela, M.: XFOIL: An Analysis and Design System for Low Reynolds Number Airfoils, in: Mueller, T. J., Low Reynolds
Number Aerodynamics, Vol. 54, Springer Berlin, Heidelberg, https://doi.org/10.1007/978-3-642-84010-4_1, 1989.

Fuglsang, P., Bak, C., Gaunaa, M. and Antoniou, I.: Design and Verification of the Risø-B1 Airfoil Family for Wind Turbines,
ASME. J. Sol. Energy Eng, Vol. 126, p. 1002-1010, <https://doi.org/10.1115/1.1766024>, November 2004.

670 Fuglsang, P., Bak, C., Gaunaa, M. and Antoniou, I.: Wind tunnel tests of Risø-B1-18 and Risø-B1-24, Forskningscenter Risøe,
Risøe-R-1375(EN), 2003.

Gasch, R. and Twele, J.: Wind Power Plants - Fundamentals, Design, Construction and Operation, Springer-Verlag Berlin
Heidelberg, <https://doi.org/10.1007/978-3-642-22938-1>, 2012.

Giguère, P., Lemayt, J., and Dumas, G.: Gurney flap effects and scaling for low-speed airfoils, in: 13th AIAA Applied
675 Aerodynamics Conference, San Diego, USA, Paper 1995-1881-CP, <https://doi.org/10.2514/6.1995-1881>, June, 1995.

González-Salcedo, Á., Croce, A., León, C. A., Nayeri, C. N., Baldacchino, D., Vimalakanthan K., and Barlas, T.: Blade Design
with Passive Flow Control Technologies, p. 11-16, in: Stoevesandt B., Schepers G., Fuglsang P., and Yeping S. (eds):

- Handbook of Wind Energy Aerodynamics, Springer, Cham., https://doi.org/10.1007/978-3-030-05455-7_6-1, 2020.
- Gruschwitz, E. and Schrenk, O.: A simple method for increasing the lift of airplane wings by means of flaps, National Advisory Committee for Aeronautics, N.A.C.A. Technical Memorandum, No. 714, Washington, 1933.
- Hansen, M. O. L.: Aerodynamics of Wind Turbines, 3rd edition, Earthscan from Routledge, Taylor & Francis Group, London, UK, <https://doi.org/10.4324/9781315769981>, 2015.
- Henne, P. A. and Gregg, R. D.: Divergent trailing-edge airfoil, United States Patent, Patent Number: 4,858,852, Date of Patent: 22th of August 1989.
- Jeffrey, D., Zhan, X. and Hurst, D. W.: Aerodynamics of Gurney Flaps on a Single-Element High-Lift Wing, Journal of Aircraft, Vol. 37, No. 2, <https://doi.org/10.2514/2.2593>, April 2000.
- Jonkman, J., Butterfield, S., Musial, W. and Scott, G.: Definition of a 5-MW Reference Wind Turbine for Offshore System Development, National Renewable Energy Lab. (NREL), Technical Report NREL/TP-500-38060, <https://doi.org/10.2172/947422>, 2009.
- Kentfield, J.: The Influence of Free-Stream Turbulence Intensity on the Performance of Gurney-Flap Equipped Wind-Turbine Blades, Wind Engineering, <https://www.jstor.org/stable/43749607>, 1996.
- Liebeck, R. H.: Design of Subsonic Airfoils for High Lift, in: 9th AIAA Fluid and Plasma Dynamics Conference, Vol. 15, No. 9, Paper 76-406, San Diego, USA, <https://doi.org/10.2514/3.58406>, 1978.
- Lin, J. C.: Review of research on low-profile vortex generators to control boundary-layer separation, Progress in Aerospace Sciences, Vol. 38, Issues 4–5, p. 389-420, ISSN 0376-0421, [https://doi.org/10.1016/S0376-0421\(02\)00010-6](https://doi.org/10.1016/S0376-0421(02)00010-6), 2002.
- Li-shu, H., Chao, G., Wen-Ping S. and Ke, S.: Airfoil flow control using vortex generators and a Gurney flap, Journal of Mechanical Engineering Science, Vol. 227, Issue 12, p. 2701-2706, <https://doi.org/10.1177/0954406213478533>, 2013.
- Maniaci, D. C., Westergaard, C., Hsieh, A. and Paquette, J. A.: Uncertainty Quantification of Leading Edge Erosion Impacts on Wind Turbine Performance, Journal of Physics: Conference Series, Vol. 1618, <http://dx.doi.org/10.1088/1742-6596/1618/5/052082>, 2020.
- Manolesos, M. and Voutsinas, S. G.: Experimental investigation of the flow past passive vortex generators on an airfoil experiencing three-dimensional separation, Journal of Wind Engineering and Industrial Aerodynamics, Vol. 142, p.130-148, ISSN 0167-6105, <https://doi.org/10.1016/j.jweia.2015.03.020>, 2015.
- Marten, D., Wendler, J., Pechlivanoglou, G., Nayeri, C. N., and Paschereit, C. O.: Development and Application of a Simulation Tool for Vertical and Horizontal Axis Wind Turbines, ASME Turbo Expo 2013, Volume 8, San Antonio, Texas, USA, Paper GT2013- 94979, <https://doi.org/10.1115/GT2013-94979>, June 2013.
- Marten, D.: QBlade: A Modern Tool for the Aeroelastic Simulation of Wind Turbines, Doctoral Thesis, Technische Universität Berlin, DOI:10.14279/depositonce-10646, <https://depositonce.tu-berlin.de/handle/11303/11758>, 2020.
- Meyer, R., Hage, W., Bechert, D. W., Schatz, M. and Thiele, F.: Drag Reduction on Gurney Flaps by Three-Dimensional Modifications, Journal of Aircraft, Vol. 43, No. 1, <https://doi.org/10.2514/1.14294>, February 2006.

- Meyer, R., K., J.: Experimentelle Untersuchungen von Rückstromklappen auf Tragflügeln zur Beeinflussung von Strömungsablösungen, PhD Thesis, Technische Universität Berlin, Hermann-Föttinger-Institut für Strömungsmechanik, 2000.
- 715 Mueller-Vahl, H., Pechlivanoglou, G., Nayeri, C. N. and Paschereit, C. O.: Vortex Generators for Wind Turbine Blades: A combined Wind Tunnel and Wind Turbine Parametric Study, ASME Turbo Expo, GT2012-69197, <https://doi.org/10.1115/GT2012-69197>, 2012.
- Oerlemans S., Fisher, M., Maeder T. and Kögler, K.: Reduction of Wind Turbine Noise Using Optimized Airfoils and Trailing-Edge Serrations, AIAA Journal, Vol. 47, No. 6, <https://arc.aiaa.org/doi/10.2514/1.38888>, June 2009.
- 720 Papi, F., Balduzzi, F., Ferrara, G. and Bianchini, A.: Uncertainty quantification on the effects of rain-induced erosion on annual energy production and performance of a Multi-MW wind turbine, in: Renewable Energy, Vol.165, p. 701-715, <https://doi.org/10.1016/j.renene.2020.11.071>, 2021.
- Pechlivanoglou, G.: Passive and active flow control solutions for wind turbine blades, PhD Thesis, Technischen Universität Berlin, Fakultät V - Verkehrs- und Maschinensysteme, 2013.
- 725 Schatz, M., Günther, B., and Thiele, F.: Numerical Simulation of the Unsteady Wake behind Gurney-Flaps, available at: https://www.cfd.tu-berlin.de/research/flowcontrol/gurneys_en/ (last access: 17 October 2020), 2004a.
- Schatz, M., Günther, B., and Thiele, F.: Computational modelling of the unsteady wake behind Gurney-flaps, 2nd AIAA Flow Control Conference Portland, Oregon, USA, Paper 2004-2417, <https://doi.org/10.2514/6.2004-2417>, June 2004b.
- Schlichting, H. and Gersten, K.: Boundary-Layer Theory, Springer-Verlag Berlin Heidelberg, Edition Number 9, <https://doi.org/10.1007/978-3-662-52919-5>, 2000.
- 730 Schmitz, G.: Theorie und Entwurf von Windrädern optimaler Leistung (Theory and design of windwheels with an optimum performance), Wiss. Zeitschrift der Universität Rostock, 5. Jahrgang, 1955/56.
- SMART BLADE: <https://www.smart-blade.com/vortex-generators> (last access: 17 October 2021), 2021.
- Storms, B. L. and Jang, C. S.: Lift Enhancement of an Airfoil Using a Gurney Flap and Vortex Generators, in: 31st AIAA Aerospace Sciences Meeting, Journal of Aircraft, Vol. 31, No. 3, Paper 93-0647, Reno, Nevada, USA, <https://doi.org/10.2514/3.46528>, May, 1994.
- 735 Timmer, W. A. and van Rooij, R. P. J. O. M.: Summary of the Delft University Wind Turbine Dedicated Airfoils, ASME. J. Sol. Energy Eng., Vol. 125(4), p. 488-496, <https://doi.org/10.1115/1.1626129>, November 2003.
- Timmer, W. A.: An overview of NACA 6-digit airfoil series characteristics with reference to airfoils for large wind turbine blades, 47th AIAA Aerospace Sciences Meeting, Orlando, Florida, AIAA 2009-268, <https://doi.org/10.2514/6.2009-268>, January 2009.
- 740 Timmer, W.A. and Schaffarczyk, A.P.: The effect of roughness at high Reynolds numbers on the performance of aerofoil DU 97-W-300Mod, Wind Energ., 7: 295-307, <https://doi.org/10.1002/we.136>, 2004.
- van Rooij, R. P. J. O. M. and Timmer, W. A.: Roughness Sensitivity Considerations for Thick Rotor Blade Airfoils, 41st

- 745 Aerospace Science Meeting and Exhibit, Reno, Nevada, USA, AIAA Paper 2003-0350, January 2003,
<https://doi.org/10.2514/6.2003-350>.
- Vestas: Aerodynamic upgrades, PowerPlus™ case study, available at:
<https://nozebra.ipapercms.dk/Vestas/Communication/Productbrochure/ProductImprovements/aerodynamic-upgrades-case-study/>, 2019 (last access: 17th of March 2022).
- 750 Wang, J. J., Li, Y. C., and Choi, K.-S.: Gurney flap - Lift enhancement, mechanisms and applications, Progress in Aerospace Sciences, Vol. 44, Issue 1, p. 22-47, ISSN 0376-0421, <https://doi.org/10.1016/j.paerosci.2007.10.001>, January 2008.
- Wilcox, B. J., White, E. B., and Maniaci, D. C.: Roughness Sensitivity Comparisons of Wind Turbine Blade Sections, Sandia Report, SAND2017-11288, <https://doi.org/10.2172/1404826>, 2017.
- Zaparka, E. F.: Aircraft and control thereof, United States Patent, Re. 19,412, Original No. 1,893,065, Date of Patent: 1st of
755 January 1935.

Dear Referee 1,

on behalf of all co-authors, I would like to thank you for taking the time to review our study. Your suggestions will definitely improve the quality of this paper.

Most of your suggestions will be implemented in the revised paper. In only a few cases, the comments are contradictory to those of Referee 2 and a synthesis of the suggestions will be tried.

Detailed one-to-one answers can be found in bold letters in the following.

Best regards,

Jörg Alber

General comments:

This paper present wind tunnel investigations on the effects of Mini Gurney flaps (MGFs) and their combination with vortex generators (VGs) on the performance of airfoils and wind turbine rotor blades.

This paper present high quality experiments with a lot of details on how to design the combined configurations of MGF and VG. Output results on the efficiency of passive devices should however be taken with caution because of two main reasons:

- the zztape effects are more important than passive device effects which is certainly an important issue for real blades that have generally LE erosion during operation. Same studies with different LE roughness should certainly be performed as pointed out by the authors.
- experiments were performed in a low turbulent intensity wind tunnel facility, which is far from the environment of operated blades and may lead to a decrease of actuator efficiency.

An important output of the present paper is the new design opportunities (chord length significantly reduced) that is provided using these passive devices. This study explains to do such a new blade design (the first detailed paper on that matter from my knowledge).

It has however some issues that need to be corrected. The major issues concern :

- the scientific objective that is unclear regarding the available literature of section 1.5.
- the hypothesis on the design of MGF and Vgs that are not always formulated, especially when using Xfoil to design actuators at high angle of incidence.

These issues will be tackled in response to the comments below.

I thus recommend the publication of the paper with corrections detailed below.

MAJOR ISSUES:

Q1: P6L137 How the present study is original from the existing literature of section 1.5 ?

Section 1.5 is a literature review on experimental studies that investigated the effect of GFs coupled with VGs based on similar wind tunnel tests. The main differences between the present study and the given references are:

1.) Storms et al. (1994), NACA 4412: This not a wind turbine airfoil. Furthermore, the Gurney flap (GF) height is 1.25 %c, which is not considered to be a mini Gurney flap (MGF) according to the definition established by the authors.

2.) Fuglsang et al. (2003). This is the only comprehensive study that the authors could find, which is based on wind turbine airfoils (of the Risø family). However, the size of the GF is 1%c and this is not considered to be a MGF. The VG design is similar in height, but different in the spacing between the vanes, here $D = 4.2\%c$ rather than $D = 7\%c$. Furthermore, the current wind tunnel tests are based on three wind turbine airfoils with different characteristics. In addition, our work expands on the wake interaction between both PFC devices, as compared to Fuglsang et al.

3.) Li-shu et al. (2013), WA251A: This not a wind turbine airfoil and, again, the GF height is 0.9 %c doesn't qualify as MGF.

In summary, we consider our work original because of the following points:

- the definition and implementation of MGFs, which are smaller than more “conventional” GFs
- the interaction between MGF and relatively small VGs
- the use of the wind tunnel data for rotor blade simulations.

The Sect. 1.5. will be reformulated to make these aspects clearer.

Q2: p8L190: “relative strong turbulence intensity of $Ti=0.3\%$ ”

For atmospheric flows in which wind turbine operates, the turbulence intensity is rather around 10%, please remove strong and put it in the context of wind tunnel facilities.

This is correct. The sentence will be reformulated to clarify that this refers to a comparison with the wind tunnel conditions of other low-turbulence wind tunnels. As such, the inflow turbulence is stronger at TU Berlin compared to e.g. TU Delft.

Q3: P9L216: this “The model revealed a non-proportional dependency on the GF height”

contradict this “diminishing HGF, dCL/hGF increased, whereas dCd/hGF decreased.

Also, from equation 6: $Cl/Cd \sim dCl/Cd$, which also contradicts the non-proportional dependency ...

It is not clear what is non-proportional to what ?

Agreed, the statement will be reformulated with more clarity.

Previous research showed that decreasing the GF height has a beneficial effect on L/D. This observation led to the basic assumption that mini GF < 0.5%c are likely to be beneficial in terms of lift and L/D for Reynolds numbers between one and two million. This assumption was validated by means of the current wind tunnel tests.

Q4: P9L221: hGF is defined relatively to the blade chord while the conclusion is “GF needs to be submerged deeply into the local BL”

The height of the device should be expressed relatively to the boundary layer thickness to do that conclusion. Also, it can't be reduced to the boundary layer thickness dependency only, as the

boundary layer is never in equilibrium on blades but subjected to different pressure gradient history depending on the blade shape. The conclusion of Alber et al (2017) study is therefore limited to the tested configurations.

The GF height is given in relation to the chord length (%c). It is crucial that the GF is significantly smaller than the BL at design conditions, i.e. at the AoA where L/D is maximal. Based on our research, the GF works best if it is between one and two times the displacement thickness (δ^*), as simulated by XFOIL. For comparison, this is in the order of 0.25% the turbulent BL thickness δ (according to the 99%*free flow- definition). Please note that these indications are guidelines.

Yes, the BL is not static and depends on a variety of factors, such as Re, AoA, suction or pressure side, the chordwise position and the transition location. Hence, the ratio between GF and BL should be taken at the design AoA. Furthermore, it is important that the wind tunnel tests cover a wider range of AoA, at least up to $c_{l,max}$.

Yes, the conclusions are always limited to the tested configurations. For instance, looking at very large Reynolds numbers, δ^* is significantly smaller and so is the optimum MGF height that should be used.

This part will be clarified.

Q5: P9L224: “ratio between the GF height and the BL displacement thickness at the TE”

Why at the TE?

This is rather at the location of the GF. The effect of GF location is certainly another parameter that needs to be explored.

The BL thickness depends on the chordwise location. We found that (using XFOIL) δ^* at the position of the GF itself (i.e. close to the TE) works well in order to determine the height of the flap.

Yes, the chordwise position of the GF is crucial. However, this study is restricted to the “classic” position at the TE. This aspect will be highlighted with more clarity.

Q6: P9L225: It is not clear here why MGF is designed at the optimal angle of incidence ? It is certainly the angle of incidence corresponding to the maximum TE boundary layer thickness, so the MGF design is detrimental to other angles of incidence?

Please explain.

The rotor blades are designed in relation to the design AoA, where the aerodynamic efficiency is maximum (L/D_{max}) to extract maximum power. The idea is precisely that the MGF is significantly smaller than the local BL, so that it is beneficial throughout the relevant range of AoA (i.e. up to $c_{l,max}$). Based on our experimental results, this approach worked well.

Q7: P10L2: “ $hMGF < \delta^*$ ”, the impact of MGF on the airfoil performance becomes insignificant.

Even if it seems obvious that the MGF size has some low limitation, how do you end-up with this value ?

We have evaluated numerous experimental studies of cambered airfoils. In general, it was observed that the GF height needs to be significantly smaller than half of the turbulent BL in order to have a beneficial effect on both lift and L/D(max). The equivalent displacement thickness is in the range of $\delta^* < h_{GF} < 2 \delta^*$.

According to wind tunnel tests, this XFOIL-based assumption is useful to estimate an appropriate MGF height. Yes, if the MGF becomes “too small” in relation to the local BL, its effect vanishes. Hence, it is assumed that below the displacement thickness δ^* , the MGF will not be effective. However, we didn’t test such tiny devices because it didn’t seem practical or helpful to do so.

This statement will be clarified.

Q8: p10L228: “ $h_{MGF} \sim 0.25 \delta$ ”

Why choosing 1/4 while 2/3 would lead to an higher aerodynamic impact and is stil compatible to eq.

8 ?

The design considerations refer to δ^* , which is simulated by XFOIL. Additionally, δ^* can be turned into δ to get a clearer idea in terms of the 99% BL definition. For the purpose of wind tunnel tests, different GF heights are chosen to cover a plausible range of GF heights.

Q9: p10L234: “ $0.1\%c < h_{MGF} < 0.7\%c$ ”

According to table 3, the minimum value of delta is 0.82%*c*, leading to $h_{MGF}=0.2\%c$ (according to equation 9). Please correct.

The definition of a MGF is provided by equation 8 ($\delta^* < h_{GF} < 2 \delta^*$). Equation 9 was included because δ (99%) is often used in literature. However, XFOIL is only capable of calculating δ^* , not δ .

The relation between eq. 8 and 9 will be reformulated in the review to avoid misunderstandings.

Q10: P10L239: “All tested ... in relation to the size of GF”, this sentence is not clear, is the GF height varying from 0.3mm to 0.6mm ? It does not seems so for the smallest MGF as the chord is $c=0.6m$ and $h_{MGF}=0.25\%c=0.15mm$. Please make it clearer.

The indications in mm (0.15mm) refer to the wall thickness of the brass profile, not the height of the GF. In this example the GF height is $0.25\%c \cdot 0.6m = 1.5 mm$

This indication will be clarified.

Q11: P10L241: on the vortex generators design

The BL transition can be extracted from Xfoil. However, Xfoil is known to be limited to attached flow configurations with difficulties to correctly predict forces when there exist flow separation and especially at C_{lmax} . I also don’t know any Xfoil output on the mean separation line.

It is therefore not clear here how the location of the mean separation line is obtained ?

Please be clearer.

The purpose of VGs is to delay separation. This mechanism is relevant for AoA close to $c_l(max)$. Before stall, it is preferable for the VGs to be submerged into the BL to limit the drag increase.

Yes, close to separation, XFOIL is less reliable. Referring to several previous studies (given as references), the δ^* calculation is considered to be sufficiently accurate for the purpose of the current wind tunnel tests.

It will be clarified that the design consideration of VGs are of low-order.

It is possible to estimate the mean separation line with XFOIL by looking at the BL of the suction side, as long as stall is not complete. The VGs are usually placed at a chordwise position closer to the leading edge, i.e. relatively far from the separation line at cl (max). Hence, the chordwise position of the laminar-to-turbulent BL transition is more relevant in terms of the VG height.

Q12: Also, once the flow is separated, there is not anymore a boundary layer flow, so the standard boundary layer thickness definition fails. Please specify how do you define it ?

The Reviewer is right. The BL thickness needs to be calculated when separation is about to be initiated at cl (max), i.e. when there still is a BL (apart from the TE separation bubble).

Q13: P11L1: “at stall, delta is similar in both the clean and tripped cases”

Stall configuration refers to a full flow separation over the blade suction side, so no delta can be measured (as there no boundary layer anymore).

Please reformulate to be clearer.

Agreed. This statement will be reformulated accordingly.

Q14: P17L377: From

Dan H. Neuhaert and Catherine B. McGinley “Free-Stream Turbulence Intensity in the Langley 14- by 22-Foot Subsonic Tunnel” NASA report NASA/TP-2004-213247, Langley Research Center, Hampton, Virginia

The turbulent intensity is one order of magnitude higher, between $\sim 0.07\%$ to 0.08% .

There is certainly a mistake in the reported Ti (0.005%), please correct.

Agreed. This statement will be corrected.

Q15: The drag signal is acquired at 10kHz and the lift is acquired at 5kHz, it is therefore possible to plot the standard deviation with the AOA. Please add this quantity that will help to evaluate further the actuator efficiency.

The signal of the force balance is indeed captured at 5 kHz. However, the mean lift value was created automatically without storing the time-resolved measurements so that this quantity cannot be provided.

The wake rake signal consists of 60 pressure tubes, so that the StDev can only be provided for each tube individually, as already illustrated in Fig. 12.

Furthermore, the 2nd review suggests the paper to be shortened. Therefore, we would prefer not to include this information for the other airfoils, too.

Conclusion:

The ZZ tape has more impact on the L/D ratio than the actuators themselves. Therefore authors

raise naturally the question of the blade roughness impact on their conclusion, but should also raise the question of the turbulent intensity impact, that has the ability to enhance the mixing rate of separated shear layers near the maximum lift values (or near stall).

Agreed.

Unfortunately, testing different types of surface roughness is beyond the scope of this study. The aspect of turbulence intensity is surely relevant. In the wind tunnel of TU Berlin, it is currently not possible to generate reproducible inflow turbulence similar to open field conditions at the hub height of a wind turbine. Apart from that, it is common practice to measure airfoils at low-turbulent inflow.

Please note: due to LE roughness (here ZZ tape), the clean rotor blade suffers from the fact that the design tip speed ratio (TSR) is increased due to the loss in lift, in this case from $TSR_{opt} = 7$ to 8 (see Fig. 23, p.32). As such, the blade is running sub-optimally, as such causing an additional drop in L/D at each blade element leading to power decrease. This lift decrease can be alleviated by adding a MGF, which enhances lift. Hence, looking at the rotating blade, the main effect of the MGF is the re-adjustment of the TSR in order to bring it back, i.e., closer, to the optimum TSR.

MINOR ISSUES:

Q1: This citation is not a peer review journal nor a conference paper:

Schatz, M., Gunther, B., and Thiele, F.: Numerical Simulation of the Unsteady Wake behind Gurney-Flaps, available at:

https://www.cfd.tu-berlin.de/research/flowcontrol/gurneys_en/ (last access: 17 October 2020), 2004a.

Agreed. The images are identical to the peer reviewed article (see Schatz et al. 2014). In order to avoid copyright issue with AIAA, we used the freely available images from our university website, which are identical.

Q2: L93: “the unsteadiness vanished as the AoA is increased from 0 to 4°”

why only until 4° ? It increases again afterwards ?

No, according to this prior study at TU Berlin of 2014, the additional unsteadiness of the MGF (compared to the baseline airfoil) vanishes at 4°. This means that for $AoA > 4^\circ$, the additional unsteadiness due to the MGF was of minor importance or irrelevant.

This statement will be clarified.

Q3: P2L37: what PFC stands for ?

Passive flow control (PFC). The abbreviation will be included.

Q4: P12L267: what is the purpose of the “airfoil box” ?

At TU Berlin, we use solid metal structures, so-called boxes, that can be lifted into the test section of the wind tunnel. The airfoil box is specific for testing different airfoil sections (wings).

The term will be explained with more clarity.

Q5: P12L274: from the static pressure difference between the inlet and outlet of a duct you only get

the pressure losses, not the dynamic pressure used to measurement the inflow velocity. Please correct the sentence.

There is a ring line of pressure tabs at both the inlet and the outlet of the duct determining the static pressure. The flow velocity can be calculated by the static pressure difference and the contraction ration (according to Bernoulli for horizontal and incompressible air flows):

$$v_2^2 = \frac{2 \cdot (p_1 - p_2)}{\rho \cdot \left(\frac{A_2}{A_1}\right)^2}$$

where v2 is the flow velocity in the test section and p1 the integrated static pressure at the inlet and p2 at the outlet.

The measurement principle will be explained in more depth.

Q6: P12L276: How the blade is attached to the balance system ?

The airfoil model is decoupled form the wind tunnel and fixed directly to the metal beam of the force balance.

The installation principle will be clarified.

Q7: P12L277: What are the wind tunnel boundary layer thickness value ? And what are the end plates dimensions and how they were chosen ?

The boundary layer thickness at the wind tunnel walls were not measured during the tests.

The dimension of the end plates will be included.

Q8: P12L277-278: The flow in the bypass region is certainly very complex with interaction between the facility boundary-layer and the end plate boundary layer. Why using that location as a reference velocity ? Is the prandtl tube in front of the blade sufficiently insufficient ? Is there blade induction effects at this location ?

The Prandtl tube in front of the airfoil model is only a reference in order to validate the inflow velocity, see Q5: P12L274. For that, the flow velocity is measured without the airfoil model and compared between the ring line and the Prandtl tube.

The Prandtl tube will be removed from the Figure to avoid misunderstandings.

Q9: P14L1: what is the origin of x ? because x=c from figure 4a is at the trailing edge ... I guess you mean x/c=2 ?

Please correct.

This indication refers to the distance between the airfoil trailing edge and the pressure tubes of the wake rake. Hence, the wake rake is positioned exactly 1 chord-length, i.e. 0.6m or 100 %, behind the airfoil trailing edge.

This indication will be specified with more clarity.

Idem p25L494: 100%c → x/c=2

Again, this means that the distance between the airfoil and the rake is 1 chord length or 100 %.

This indication will be specified with more clarity.

Q10: P14L2: what do you mean by “return to static pressure level in the wind tunnel” ?

If the pressure is measured in the blade wake area at high angle of incidence, 1D is certainly not sufficient to return to the static pressure level in the wind tunnel. Please be more specific.

According to the references given in the report (Barlow et al. p.178), the wake rake should be located at least $0.7c$ behind trailing edge for the static pressure not to be affected by the unsteadiness of the airfoil wake.

This statement will be specified.

Q11: P14L311: “two Prandtl tubes that are installed inside the downstream plane of the rake, one on top and one below the casing”

This sentence is not clear as Prandtl tubes measure the dynamic pressure (difference between static and total pressure). Please be clearer.

Prandtl tubes are used to measure both the total pressure (in front) and the static pressure (from the side). This method will be clarified.

Q12: P14: careful on the notations: $\Delta P(y_i) = \Delta P_i$ of equation 11?

$P_{total} = \bar{P}$ total (the question behind is: how long the signal was acquired and does the bar mean averaged over that signal ?)

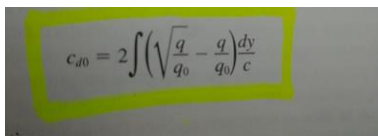
$P_{static} = \bar{P}$ static (idem)?

Yes, the bar on top of the p indicates that each signal (of each pressure tube) was averaged over the measurement duration of 5 sec per AoA (after 4 sec buffer).

This indication will be clarified.

Q13: P14L330: please explain (quickly) where the relation 14 comes from.

Eq. 14 is the practical and detailed implementation of the momentum loss, see e.g. Barlow et al. p. 177.


$$c_{d0} = 2 \int \left(\sqrt{\frac{q}{q_0}} - \frac{q}{q_0} \right) \frac{dy}{c}$$

Q14: P14L340: About Λ : is it related to the airfoil thickness (and so dependent on each airfoil), or is it the height of the test section (and so a fixed value). Please make it clearer.

Λ is the so-called body shape factor as introduced by Allen and Vincenti (1944). It is a function of the maximum thickness of the aerodynamic body, here the airfoil model. For brevity, the reader is referred to secondary literature, such as Barlow et al. p. 352.

Q15: Please provide the raw lift and drag curves to see the improvement when applying the wind tunnel correction.

The raw data would probably not provide any additional insight. For space economy and according to the 2nd review (length of the report), we would prefer to not include more data.

Q16: P18L396: Next, figure 12a ... isn't it figure 11a ?

Please check.

Yes, this mistake will be corrected.

Q17: P18 legend of figure 11 on p19.

Please correct

Agreed. The layout will be corrected.

Q18: p21L1-2: it should also be noted that there is only marginal L/D improvement between GF cases.

The marginal L/D improvement in the clean case of Fig. 13 (b) will be highlighted.

Q19: P26L506: normalizing the vertical position with the chord and locate the center relatively to the blade will help to evaluate the wake extend and thus conclude on the flow separation extend, that is not necessarily going up to the trailing edge - stalled (in figure 15a: the baseline zz case indicates that the flow separation do not occurs at the leading edge).

The Reviewer's suggestion is not completely clear to us. The vertical positions of the rake tubes are normalized by the total rake span, i.e. the distance from the top to the bottom tube. Hence, $y = 0.0$ is the exact middle of the wake rake. At positive AoA, the minimum pressure point is pushed towards the wind tunnel floor due to the downwash effect in the airfoil wake.

Using ZZ tape, Fig. 15 (a) indicates that stall is happening without the drop in lift in the clean case. This is a common observation of airfoil measurements in wind tunnels.

Q20: P26L509: please replace "suppress" by "delay"

Okay.

Q21: p27 Figure 19: I don't see the benefit of adding GF (or MGF) compared to VG alone, and it is not commented in the article.

Please explain why MGF+VG is better than VG alone for that configuration ?

The benefit of using both MGF+VG is that the L/D ratio is slightly improved and, more importantly, that pre-stall lift is significantly elevated. The latter aspect is crucial in order to mitigate the lift decrease due to roughness on the rotating blade.

This benefit will be highlighted.

Q22: P30: legend of figure 20 is misplaced.

The legend will be corrected.

Dear Mohammad Mahfouz (RC2),

on behalf of all co-authors, I would like to thank you for taking the time to review our study. Your suggestions will definitely improve the quality of this paper.

Most of your suggestions will be implemented in the revised paper. The report will be restructured and shortened, as suggested. In only a few cases, your comments cannot be implemented entirely.

Detailed one-to-one answers are provided inside the pdf supplement.

Best regards,

Jörg Alber



Experimental investigation of Mini Gurney Flaps in combination with vortex generators for improved wind turbine blade performance

Jörg Alber¹, Marinos Manolesos², Guido Weinzierl-Dlugosch³, Johannes Fischer³, Alexander Schönmeier¹, Christian Navid Nayeri¹, Christian Oliver Paschereit¹, Joachim Twele⁴, Jens Fortmann⁴, Pier Francesco Melani⁵, Alessandro Bianchini⁵.

¹ Technische Universität Berlin, Hermann-Föttinger Institut, Müller-Breslau-Str. 8, 10623 Berlin, Germany

² College of Engineering, Swansea University, Bay Campus, Fabian Way, Swansea, SA1 8EN, United Kingdom

³ SMART BLADE GmbH®, Waldemarstr. 39, 10999 Berlin, Germany

10 ⁴ Hochschule für Technik und Wirtschaft Berlin, Wilhelminenhofstraße 75A, 12459 Berlin, Germany

⁵ Università degli Studi di Firenze, Department of Industrial Engineering (DIEF), Via di Santa Marta 3, 50139 Firenze, Italy

Correspondence to: Jörg Alber (joerg.alber@posteo.de)

Abstract

This wind tunnel study investigates the aerodynamic effects of Mini Gurney flaps (MGFs) and their combination with vortex generators (VGs) on the performance of airfoils and wind turbine rotor blades. VGs are installed on the suction side aiming at stall delay and increased maximum lift. MGFs are thin angle profiles that are attached at the trailing edge in order to increase lift at pre-stall operation. The implementation of both these passive flow control devices is accompanied by a certain drag penalty. The wind tunnel tests are conducted at the Hermann- Föttinger Institut of the Technische Universität Berlin. Lift is determined with a force balance and drag with a wake rake for static angles of attack from -5° to 17° at a constant Reynolds number of 1.5 million. The impact of different MGF heights including 0.25%, 0.5% and 1.0 % and an uniform VG height of 1.1 % of the chord length are tested on three airfoils that are characteristic for different sections of large rotor blades. Furthermore, the clean and the tripped baseline cases are considered. In the latter, leading edge transition is forced by means of Zig Zag (ZZ) turbulator tape. The preferred configurations are the smallest MGF on the NACA63(3)618 and the AH93W174 (mid to tip blade region) and the medium sized MGF combined with VGs on the DU97W300 (root to mid region). Next, the experimental lift and drag polar data is imported into the software QBlade in order to design a generic rotor blade. The blade performance is simulated with and without the add-ons based on two case studies. In the first case, the retrofit application on an existing blade mitigates the adverse effects of the ZZ tape. Stall is delayed and the aerodynamic efficiency is partly recovered leading to an improvement of the power curve. In the second case, the new design application allows for the design of a more slender blade while maintaining the power output. Moreover, the alternative blade appears to be more resistant against forced leading edge transition.



1. Introduction

1.1 General outline

The study is divided into the following sections.

1. **Introduction.** The concepts, mechanisms and applications of Gurney flaps (GFs), ZZ tape and VGs are introduced. The literature review is focused on very small GF heights, so-called MGFs, and the combination of GFs with VGs.
2. **Airfoil simulations.** The simulation software XFOIL (Drela, 1989) is used to determine the appropriate dimensions of each PFC device in relation to the local boundary layer thickness of the following airfoils: the NACA63(3)618, the AH93W174 and the DU97W300.
3. **Experimental set-up.** The wind tunnel test section, the measurement methods and the data reduction process are specified including the force balance for the lift, and the wake rake for the drag measurements at a constant Reynolds number of $Re = 1.5 \cdot 10^6$.
4. **Experimental results.** The baseline lift and drag polars, $c_l(\alpha)$ and $c_d(\alpha)$, of each airfoil are validated against literature data. Different combinations of MGFs and VGs are assessed according to characteristic parameters, i.e. the lift performance, the stall behavior and the aerodynamic efficiency.
5. **Rotor blade performance.** The experimental data of the preferred configurations is imported into the software QBlade (Marten, 2020) to create a generic rotor blade. The blade performance is simulated based on two case studies, the retrofit application on an existing, and the new design application on an alternative rotor blade.

1.2 Gurney flaps

This aerodynamic device is named after the US racecar driver Dan Gurney. In the early 1970s, he applied it to the rear spoilers achieving significant improvements in the downforce and thus the traction of his Formula One vehicles, see Liebeck (1978). Passive GFs are categorized as static miniflaps or miniature trailing edge devices (MiniTEDs), as described by González-Salcedo et al. (2020). Hence, they are different to the concept of flexible trailing edge (TE) flaps that are integrated into the very TE section, see Barlas and van Kuik (2010). The first reference to miniflaps dates back to the early 20th century and was probably developed by Gruschwitz and Schrenk (1933). Zaparka (1935) registered the first patent on active miniflaps for use on airplane wings. Various patents of passive miniflaps followed, particularly in aviation. Boyd (1984) and later Brink (2002) claimed the rights on different versions of wedge-shaped TE flaps. Henne and Gregg (1989) patented the shape of a diverging trailing edge (DTE) of a transonic airfoil generating similar aerodynamic effects than the GF. Bechert et al. (2001) registered a patent on so-called three dimensional (3D) GFs, i.e. profiles with slits, serrations, holes, as well as tiny vortex generators attached to the miniflap itself in order to stabilize the otherwise unsteady wake field. Wang et al. (2008) published a comprehensive review of GFs for use on rotor blades of helicopters and wind turbines. In contrast to the large amount of patents and publications, there are only few examples of standardized or commercialized GF applications on rotor blades of horizontal axis wind turbines (HAWTs). For instance, Vestas (2019) offers GFs in combination with VGs as aerodynamic



upgrades of operating wind turbines predicting the average energy production (AEP) to increase by 1.7%. Another example is the blade design of the 10 MW reference wind turbine of the Danish Technical University (DTU) with a total rotor radius of $R = 89.2$ m. The inner blade part alongside the local rotor radius of $5\%R < r < 40\%R$ was equipped with wedge-shaped GFs including heights of 3.5%, 2.5% and 1.3%, respectively, in relation to the local chord length. Bak et al. (2013) claim significant aerodynamic performance improvements, especially on relatively thick airfoils with a maximum thickness of $h_{th,max} \geq 30\%c$.

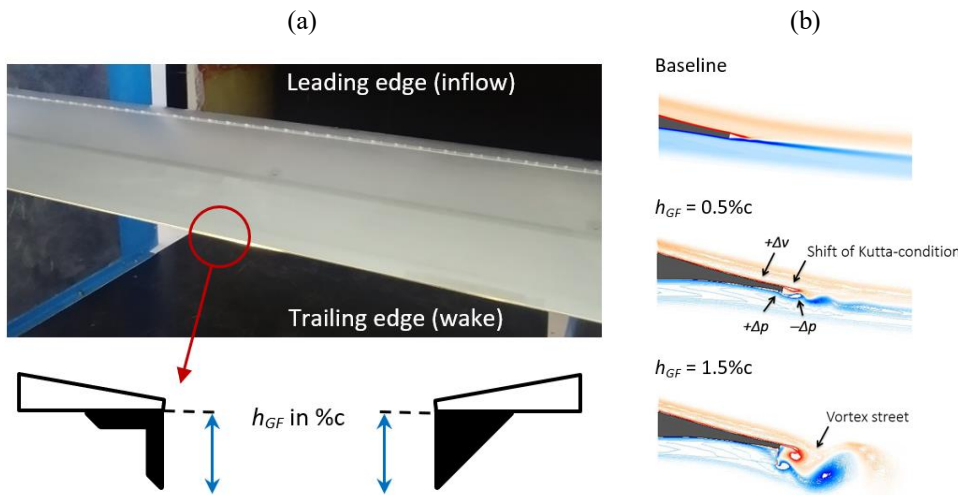


Figure 1. (a) NACA63(3)618 during wind tunnel tests. Vortex generator array and Gurney flap. Definition of Gurney flap height of rectangular and triangular profiles in side view. (b) CFD simulations of the HQ17. Wake structures at $\alpha = 0.0^\circ$ and $Re = 1 \cdot 10^6$ for different Gurney flap heights, reproduced and modified from Schatz et al. (2004a).

Figure 1a displays typical GFs, i.e. the rectangular, or L-shaped, and the triangular, or wedge-shaped, profiles. They are attached at the TE of wings and rotor blades, normal to the pressure side. In both cases, the effective GF height, h_{GF} , is expressed in percentage of the chord length, $\%c$, without taking the original TE thickness, h_{TE} , into account. For identical h_{GF} , the aerodynamic effect of both GF profiles is considered to be very similar, as discussed in Sect 4.1.2. Figure 1b illustrates the principal changes of the flow field for two different GF heights, as first reported by Liebeck (1978). Adjacent to the TE modification, a highly efficient vortex system is formed consisting of one vortex upstream and two counter rotating vortices immediately downstream. Bechert et al. (2000) and Schatz et al. (2004b) showed by means of experimental and numerical investigations that the wake flow structures are quasi two dimensional (2D) at pre stall operation. The recirculation region changes the Kutta condition, so that the rear stagnation point is shifted downstream and deflected downwards, see Jeffrey et al. (2000) and Cole et al. (2013). The modifications of the flow field lead to the following set of simultaneous effects:

- **Lift performance:** The suction peak is higher and coupled with a positive pressure built-up right in front of the GF, increasing the pressure difference between suction side (SuS) and pressure side (PS). As a results, the effective camber is enhanced, thus shifting the lift curve upwards so that the same $c_l(\alpha)$ is already reached at a lower angle of attack (AoA), α . Furthermore, the adverse pressure gradient on the SuS becomes milder generating higher maximum lift coefficients, $c_{l,max}$, as stall is initiated.



- Drag behavior: The recirculation or low pressure region in the immediate wake causes an increased momentum loss and thus higher drag coefficients, $c_d(\alpha)$. In addition, the intensity of the unsteadiness is stronger, especially if vortex shedding is initiated in the form of an absolute instability, as illustrated in Figure 1b for $h_{GF} = 1.5\%c$.

90 Overall, the impact of GFs is quantifiable as an increase in both lift, Δc_l , and drag, Δc_d . Bechert et al. (2000) and Schatz et al. (2004b) showed that $\Delta c_d(\alpha)$ is directly related to the lift fluctuations, i.e. the intensity and the frequency of the wake unsteadiness. As a consequence, the drag penalty proved to be less severe for small GF heights, comparing $h_{GF} = 0.5\%c$ to $1.5\%c$ in Figure 1b. Furthermore, in case of $h_{GF} = 0.5\%c$, the unsteadiness vanished as the AoA is increased from $\alpha = 0.0^\circ$ to 4.0° , as illustrated comparing Figure 1b to Figure 5c. In summary, the reviewed results indicate the possibility to improve, or at least to maintain, the lift to drag (L/D) ratio by installing rather small GFs heights in the order of $h_{GF} \leq 0.5\%c$ at $Re \approx 1 \cdot 10^6$.

1.3 Zig Zag tape

ZZ turbulator tape is implemented to initiate the boundary layer (BL) transition at a fixed chord position, see Figure 3a. Its height, h_{ZZ} , should be slightly smaller than the local laminar BL thickness in order to trigger transition while avoiding a disproportionate drag increase or even turbulent separation. Next to trip wire or carborundum paper, ZZ tape facilitates the comparability between different measurement methods. Moreover, it is applied to evaluate the sensitivity of airfoils to adverse leading edge roughness (LER) effects, as discussed by van Rooij and Timmer (2003), Timmer and Schaffarczyk, (2004) and in greater detail by Wilcox et al. (2017). Another example is Oerlemans et al. (2009), who implemented ZZ tape on the rotor blades of research wind turbines. In fact, LER due to erosion and the accumulation of sediments are major challenges for rotor blade manufacturers and wind turbine operators, see Figure 2b. According to Maniaci (2020), LER mainly affects the mid to tip region where the rotor blade is exposed to high relative velocities. Depending on the severity, or the degree of roughness, the AEP decrease of multi MW HAWTs is between of 2 % and 5 %.

1.4 Vortex generators

As opposed to GFs, VGs have been commercialized by various wind energy companies for almost two decades. The suboptimal or declining AEP over the years is often the reason for blade manufacturers and wind park operators to investigate the possible causes, such as early separation, LER, and to invest in feasible solutions, such as PFC devices. VGs are implemented in order to prevent, or at least to alleviate, the flow separation in the root to mid region of rotor blades. More recent studies have investigated the opportunities of relatively small VG heights in the mid to tip blade region, see Bak et al. (2018). According to Lin (2002), they are referred to as sub- BL or low profile VG configurations, see Sect. 2.5. Typically, VGs are commercialized as retrofit solutions, i.e. add-ons that are installed onto the surface of already running rotor blades, as depicted in Figure 2a. In this way, SMART BLADE (2021) predict an AEP growth of approximately 2%. A more detailed review on VGs for use on rotor blades is provided by Bak et al. (2016) and González-Salcedo et al. (2020).

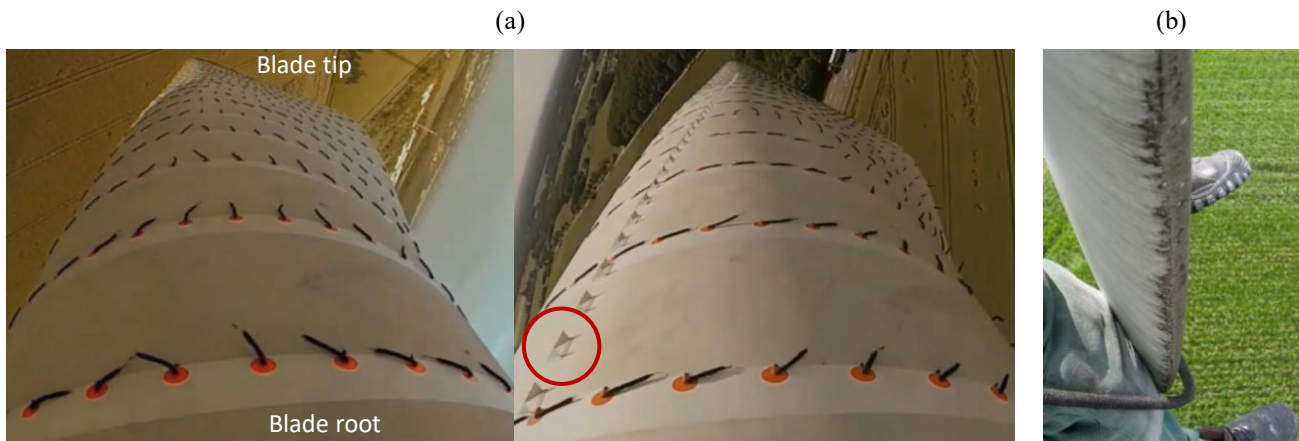


Figure 2. Utility scale wind turbines. (a) Simultaneous flow tuft measurements on different blades of the same rotor, baseline versus VG configuration, with permission from SMART BLADE GmbH. (b) Leading edge erosion at the blade tip, with permission from Seilpartner GmbH.

120 The purpose of VGs is to delay the stagnation of the BL flow and thus separation. Installing VGs, Figure 2a illustrates that the flow tufts are attached to the blade surface **until closer** to the TE, as compared to the stalling baseline blade. The thin vane tips shed a pair of vortices in order to transport momentum from the free flow into the viscous BL close to the surface. The vortex system spreads out towards the TE, where it is released into the immediate wake. More detailed research on the underlying mechanism of VGs is provided by Manolesos and Voutsinas (2015). Overall, the VG effect is quantifiable as a substantial

125 increase in both maximum lift, $c_{l,max}$, and the AoA where stall is initiated, $\alpha(c_{l,max}) = \alpha_{cl,max}$. However, drag is increased significantly at low and moderate AoA. The impact on the aerodynamic efficiency, $L/D(\alpha)$, depends on the design parameters illustrated in Figure 3.

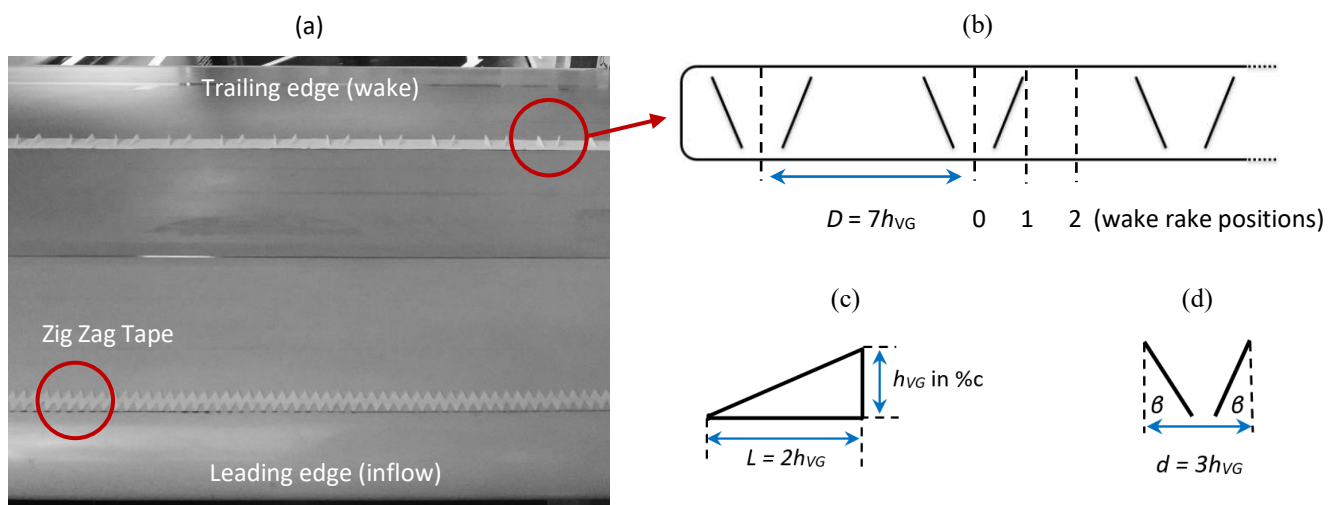


Figure 3. NACA63(3)618 during wind tunnel tests. (a) Top view on suction side with Zig Zag tape and VG array. (b) VG panel including spacing between VG centers and measurement positions of the wake rake, with permission from SMART BLADE GmbH. (c) Side view of single vane. (d) Top view of pair of vanes.



Figure 3a and b depict an array of VG panels as it is installed on the airfoil SuS throughout the wind tunnel tests, see Sect. 3 and 4. Following Timmer and van Rooij (2003) and Baldacchino et al. (2018), the design parameters generate a counterrotating, common downflow VG system. According to Figure 3c, each VG consists of a delta-shaped pair of vanes with a uniform length, $L = 2h_{VG}$, and a certain VG height, h_{VG} , given in %c. Figure 3d shows that the distance between the two vanes is $d = 3h_{VG}$, facing each other in an angle $\beta \approx \pm 18^\circ$. Furthermore, the spacing between the center points of two VGs is $D = 7h_{VG}$, see Figure 3b. The positions 0, 1 and 2 indicate the spanwise wake rake locations, as discussed in Sect. 4.2.3.

1.5 Combining Vortex generators and Gurney flaps

Despite the large body of literature on both PFC devices, the simultaneous use of GFs and VGs is less profoundly researched. Storms et al. (1994) investigated one such configuration in the NASA Ames Research Center based on the NACA4412 at $Re = 2 \cdot 10^6$. Combining $h_{GF} = 1.25\%$ with $h_{VG} = 0.5\%$ at $x_{VG} = 12\%$ and a spacing between the VGs of $D = 6h_{VG}$, stall is delayed by around 5° and $c_{l,max}$ is increased by 36 % improving L/D at elevated AoA. However, at low and moderate AoA, the combined drag penalty leads to reduced L/D (α). Fuglsang et al. (2003) conducted extensive research based on the Riso-B1-24 in the VELUX wind tunnel of the DTU at $Re = 1.6 \cdot 10^6$. The Riso-B1 family is dedicated to rotor blades of multi MW wind turbines. The tested configurations consisted of $h_{GF} = 1\%$ combined with $h_{VG} = 1\%$ at $x_{VG} = 20\%$ and $D = 4.2h_{VG}$ delaying separation by approximately 3° , coupled with an increase in $c_{l,max}$ of 34 %. Additionally, ZZ tape was applied on the suction side with $h_{ZZ} = 0.35$ mm at $x_{ZZ} = 5\%$. Still, the combined effect of GFs and VGs delayed stall by approximately 3° and increased $c_{l,max}$ by 29 %. Fuglsang et al. (2004) concluded that, despite a small L/D decrease, the combination of both devices “(...) could provide an attractive choice for the root part of a wind turbine blade where reduction of solidity is a key issue to reduce blade costs.”. Besides, these results are in good agreement with comparable tests using the prior Riso-A1-24 airfoil design, as previously reported by Fuglsang et al. (1999). In a more recent study, Li-shu et al. (2013) performed experiments on the WA251A airfoil at the Northwestern Polytechnical University of Xi'an at $Re = 3 \cdot 10^6$. Applying $h_{GF} = 0.9\%$ and 1.25% together with $h_{VG} = 0.5\%$ at $x_{VG} = 21\%$, $c_{l,max}$ is increased by 18.6 % delaying stall by approximately 2° . The authors report “remarkable improvements” implementing both PFC devices simultaneously. In all mentioned reports of this section, the combined effect of GFs and VGs appears to be beneficial compared to the corresponding VG (only) configuration.

2. Airfoil simulations

In preparation for the wind tunnel tests, the simulation software XFOIL is used to determine the appropriate dimensions of each PFC device in relation to the local boundary layer thickness of the corresponding airfoil.



2.1 Airfoils

Figure 4a shows the airfoils that are tested throughout the wind tunnel experiments: the NACA63(3)618, the AH93W174 and DU97W300. They are applied at different sections of large rotor blades, see Figure 4b. The main airfoil specifications are summarized in Table 1.

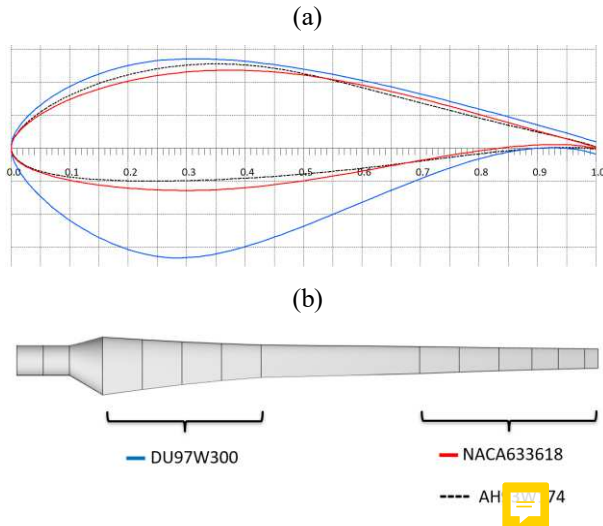


Figure 4. NACA63(3)618, AH93W174, DU97W300. (a) Airfoil coordinates normalized by the chord length. (b) Position of airfoils on a generic rotor blade.

Table 1. Maximum thickness, maximum camber and trailing edge thickness. Chord position in brackets. All values in %c.

	$h_{th,max}(x)$	$h_{camber,max}(x)$	h_{TE}
NACA63(3)618	18.0 (34.0)	3.0 (53.7)	0.17
AH93W174	17.4 (33.0)	4.0 (38.0)	0.33
DU97W300	30.0 (29.3)	2.1 (80.5)	1.75

165

The NACA63(3)618 is part of the six-digit wing sections developed by the National Advisory Committee for Aeronautics (NACA) for use on high speed aircrafts, see Abbott and von Doenhoff (1959). The NACA 63 and 64 families are still popular for the design of large rotor blades, especially in the mid to tip region, see Timmer (2009). The NACA63(3)618 is characterized by a relatively high lift and low drag performance due to the extended laminar BL. The main downside is the sensitivity to roughness effects, as shown in Sect. 4.1.1. The AH93W174 is a wind turbine airfoil for the mid to tip blade region developed by the Institut für Aerodynamik und Gasdynamik (IAG) at Stuttgart University, see Althaus (1996). Compared to the NACA63(3)618, the maximum thickness is similar, but the maximum camber is higher, thus leading to a steeper lift slope. Furthermore, L/D_{max} is shifted towards more elevated AoA covering a relatively wide range of high performance. However, the aerodynamic efficiency is degraded by the effect of forced LE transition, see Sect. A1. The DU97W300 is dedicated to the root to mid blade region, developed by the Delft University (DU), see Timmer and van Rooij (2003). It is characterized by the

175



limited upper surface thickness and relatively low maximum camber, see Figure 4a. Therefore, the pressure recovery is milder avoiding premature separation on the suction side, while improving its sensitivity to roughness effects, see Sect. 4.2.1. The lift penalty is compensated for by the pronounced S- shape of the PS contour approaching the TE, as explained by van Rooij and Timmer (2003). In fact, this aft-loading tail changes the flow field in a similar way than the GF, as previously discussed in Sect. 1.2.

2.2 XFOIL simulations

The 2D airfoil performance is simulated with the panel code XFOIL developed by Drela (1989). The freely available and widely recognized software is based on an viscid-inviscid interaction scheme, which was validated, amongst many others, by Timmer and Schaffarczyk (2004) and Fuglsang et al. (2004). Apart from the airfoil coordinates, including the finite TE thickness, the software requires the chord-based Re number, here $Re = 1.5 \cdot 10^6$ and the AoA range, here $-5^\circ < \alpha < 20^\circ$, as input parameters. The location of the free laminar-to-turbulent BL transition is modeled by means of the e^N method. The amplification factor, or N criterion, describes the level of both the surface roughness and the inflow turbulence intensity. The default value, $N = 9$, refers to clean conditions, i.e. assuming a completely smooth surface and laminar inflow conditions that are found in low turbulence wind tunnels. In this study, $N = 5$ is chosen to account for the relatively strong turbulence intensity of approximately 0.3%, see Sect. 3.1. In the so-called tripped case, the transition location is fixed at a static chordwise position, x_{tr} , on both the SuS and the PS.

The appropriate height of each PFC device is determined in relation to the local BL thickness, δ , which is defined as the normal distance between the solid surface and the first streamline reaching 99% of the axial free flow velocity. XFOIL calculates the BL displacement thickness, δ^* , i.e. describing the distance by which the free flowing streamlines are displaced from the solid surface due to the existence of the BL. According to Schlichting and Gersten (2000), the laminar BL thickness on a flat plate at zero incidence is approximately three times the BL displacement thickness,

$$\delta \approx 3\delta^*. \quad (1)$$

Eq. (1) is also valid for thin airfoil shapes. According to Baldacchino et al. (2018), the turbulent BL thickness is related to δ^* and the momentum thickness θ ,

$$\delta \approx \theta \left(3.15 + \frac{1.72}{\left(\frac{\delta^*}{\theta} \right) - 1} \right) + \delta^*. \quad (2)$$

2.3 Zig Zag tape

The baseline configurations include both the free and the forced BL transition. In the so-called tripped case, ZZ tape is applied alongside the complete airfoil span on both the SuS and the PS, as shown in Figure 3a. The ZZ tape height is selected in relation to the laminar BL thickness, see Eq. (1), at the corresponding chord positions, x_{ZZ} , and the design AoA, $\alpha_{opt} = \alpha(L/D_{max})$, so that



$$h_{ZZ} \leq \delta(\alpha_{opt}, x_{ZZ}) \leq 3\delta^*(\alpha_{opt}, x_{ZZ}), \quad (3)$$

205 where $x_{ZZ,SUS} = 5 \%c$ and $x_{ZZ,PS} = 10 \%c$.

Table 2. XFOIL simulations of the boundary layer thickness according to Eq. (1).

	$\alpha_{opt} [^\circ]$	$\delta_{SUS} [mm]$	$\delta_{PS} [mm]$
NACA63(3)618	5	0.51	0.55
AH93W174	7	0.53	0.53
DU97W300	9	0.54	0.42

According to Table 2 and applying Eq. (3), the NACA63(3)618 and the AH93W174 are both equipped with $h_{ZZ} = 0.4 \text{ mm}$, and the DU97W300 with $h_{ZZ} = 0.3 \text{ mm}$. The width of the turbulator tape is 12 mm and the angle between its sections is 60° .

210 These characteristics are in close agreement with comparable wind tunnel tests at the DU and the DTU, see Sect. 4.

2.4 Mini Gurney flaps

Previously, the authors reviewed wind tunnel studies of 9 different DU and NACA airfoils at $1 \cdot 10^6 < Re < 2 \cdot 10^6$, as described in Alber et al. (2017). The lift and the drag increase between the GF and the baseline configurations, Δc_l and Δc_d , were modelled with a surface best fit, resulting in the first degree polynomial functions ($R^2 > 0.9$),

$$\Delta c_l(\alpha) = c_{l,GF}(\alpha) - c_l(\alpha) = K_1 h_{GF} + K_2 c_l(\alpha) + K_3, \quad (4)$$

$$\Delta c_d(\alpha) = c_{d,GF}(\alpha) - c_d(\alpha) = K_4 h_{GF} + K_5 c_d(\alpha) + K_6, \quad (5)$$

215 where K_i are the polynomial coefficients for $0.2 \%c \leq h_{GF} \leq 2 \%c$, for $\Delta c_l, \Delta c_d > 0$.

The model revealed a non-proportional dependency on the GF height: diminishing h_{GF} , $\frac{\Delta c_l(\alpha)}{h_{GF}}$ increased, whereas $\frac{\Delta c_d(\alpha)}{h_{GF}}$ decreased. Consequently, applying Eq. (4) and (5), the impact of the GF height on the aerodynamic efficiency was estimated by means of the following condition,

$$\frac{(c_l + \Delta c_l)(\alpha)}{(c_d + \Delta c_d)(\alpha)} \geq \frac{c_l(\alpha)}{c_d(\alpha)} \equiv \frac{\Delta c_l(\alpha)}{\Delta c_d(\alpha)} \geq \frac{c_l(\alpha)}{c_d(\alpha)}, \quad (6)$$

for $c_l, c_d > 0$.

220 Based on the data evaluation of Alber et al. (2017), Eq. (6) was only satisfied for relatively small GFs in the range of $0.2 \%c \leq h_{GF} \leq 0.5 \%c$. In other words, the GF needs to be submerged *deeply* into the local BL to avoid an over-proportional drag, in relation to the lift increase, as previously postulated by Giguère et al. (1995), Kentfield (1996) and Giguère et al. (1997). Hence, the crucial design parameter with regard to the aerodynamic efficiency is the ratio between the GF height and the BL displacement thickness at the TE,

$$\frac{h_{GF}}{\delta^*}(\alpha). \quad (7)$$

225 Following from Eq. (7), the definition of a MGF hereby refers to an effective height of between one and two times the local δ^* at the design AoA, so that



$$\delta^*(\alpha_{opt}) \leq h_{MGF} \leq 2\delta^*(\alpha_{opt}). \quad (8)$$

For $h_{MGF} < \delta^*$, the impact of the MGF on the airfoil performance becomes insignificant. Combining Eq. (2) and Eq. (8), an appropriate MGF height is estimated to be in the order of one quarter of the turbulent BL thickness at the TE,

$$h_{MGF} \approx 0.25 \cdot \delta(\alpha_{opt}). \quad (9)$$

Within the boundary condition given by Eq. (8) and Eq. (9), the impact of a MGF appears to be beneficial in terms of the lift performance, the stall behavior and the aerodynamic efficiency, as further discussed in Sect. 4.

Table 3. XFOIL simulations of the boundary layer thickness according to Eq. (2).

	$\alpha_{opt} [^\circ]$	$\delta_{clean}^* [\%c]$	$\delta_{clean} [\%c]$	$\delta_{ZZ}^* [\%c]$	$\delta_{ZZ} [\%c]$
NACA63(3)618	5	0.17	1.28	0.28	2.07
AH93W174	7	0.11	0.82	0.23	1.66
DU97W300	9	0.25	2.16	0.35	2.85

According to Table 3 and applying Eq. (8) and Eq. (9), the MGFs are in the range of $0.1 \%c < h_{MGF} < 0.7 \%c$. It is reiterated that δ^* increases significantly in case of forced LE transition due to the early expansion of the turbulent BL. This observation is crucial when applying MGFs in order to compensate for the decambering effects of ZZ tape, as discussed in Sect. 4 and 5. In summary, $h_{MGF} = 0.25 \%c$, $0.5 \%c$ and $h_{GF} = 1 \%c$ are implemented to cover for both the clean and the tripped baseline cases. It is noted that $h_{GF} = 1 \%c$ is not considered a MGF configuration as per Eq. (8). All tested GFs consist of standard and equilateral angle profiles made of brass with an ascending wall thickness of 0.3 mm, 0.5 mm and 0.6 mm, in relation to the size of the GF.

2.5 Vortex generators

In general, the chord position of the VG array, x_{VG} , is located upstream the mean separation line, $x_{sep}(\alpha_{cl,max})$, in order to delay stall, and downstream of the BL transition location, $x_{tr}(\alpha_{opt})$, in order to minimize the drag penalty, so that $x_{tr}(\alpha_{opt}) < x_{VG} < x_{sep}(\alpha_{cl,max})$. Applying Eq. (2), the VG height is determined in relation to the turbulent BL thickness on the SuS, i.e. at the initiation of stall,

$$h_{VG} \geq \delta(x_{VG}, \alpha_{cl,max}). \quad (10)$$

Table 4. XFOIL simulations of the boundary layer thickness according to Eq. (2).

	$\alpha_{cl,max} [^\circ]$	$x_{VG} [\%c]$	$\delta_{clean}(x_{VG}) [\%c]$	$\delta_{ZZ}(x_{VG}) [\%c]$
NACA63(3)618	12	50	1.55	1.62
AH93W174	11	30	0.64	0.66
DU97W300	12	30	0.58	0.72



Table 4 shows that, at stall, δ is similar in both the clean and the tripped cases. Based on Eq. (10), an uniform VG height of $h_{VG} = 1.1\%c$ is selected, including the thickness of the base panel, see Figure 3b. In case of the DU97W300 and the AH93W174, $x_{VG} = 30\%c$ resembles a standard VG array in the root to mid region of rotor blades. Regarding the NACA63(3)618, a tip VG configuration is investigated at $x_{VG} = 50\%c$, where $h_{VG} < \delta$ in order to reduce additional drag. Next to the effect of stall delay, the primary objective is to maintain L/D (α) on a high level in the mid to tip blade region. According to Lin (2002), the optimum height of sub-BL or low-profile VGs is in the range of $20\%\delta < h_{VG} < 50\%\delta$.

2.6 Summary

Figure 5a displays both the height and the chordwise location of each PFC device that is investigated in this section. Figure 5b and Figure 5c depict the vorticity caused by either VGs or MGFs, according to previous research efforts at the HFI of the TU Berlin. The wake interaction of the flow control mechanisms and its effects on the lift and drag performance is tested as part of the wind tunnel campaign, as described in the following sections of this report.

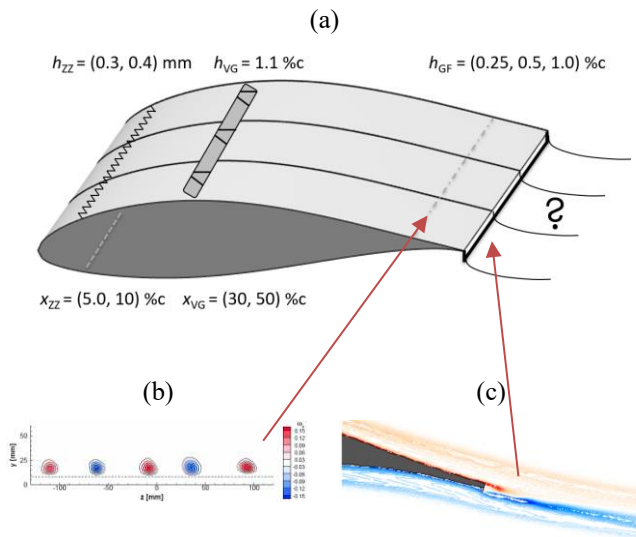


Figure 5. (a) Height and location of passive flow control devices. (b) PIV measurements of VG vortices on the NACA63(3)618 in spanwise view ($h_{VG} = 1.7\%c$ at $x_{PIV} = 80\%c$ and $Re = 1.3 \cdot 10^6$), reproduced from Mueller-Vahl et al. (2012). (c) CFD simulations of a Mini Gurney flap on the HQ17 in side view ($h_{GF} = 0.5\%c$ at $\alpha = 4.0^\circ$ and $Re = 1 \cdot 10^6$), reproduced from Schatz et al. (2004a).

3. Experimental set-up

The wind tunnel test section, the measurement methods and the data reduction process are specified, including the force balance for the lift, and the wake rake for the drag measurements at a constant Reynolds number of $Re = 1.5 \cdot 10^6$.



265 3.1 Test section



270 Between 1998 and 2000, the airfoil box was designed, constructed and integrated into the wind tunnel by Meyer (2000) in cooperation with the Deutsche Zentrum für Luft- und Raumfahrt e.V. (DLR). Since then, it has provided the experimental set-up for numerous research projects with a focus on passive and active flow control devices, such as Bechert et al. (2000), Meyer et al. (2006), Pechlivanoglou et al. (2011), Mueller-Vahl et al. (2012) and Bach et al. (2014).

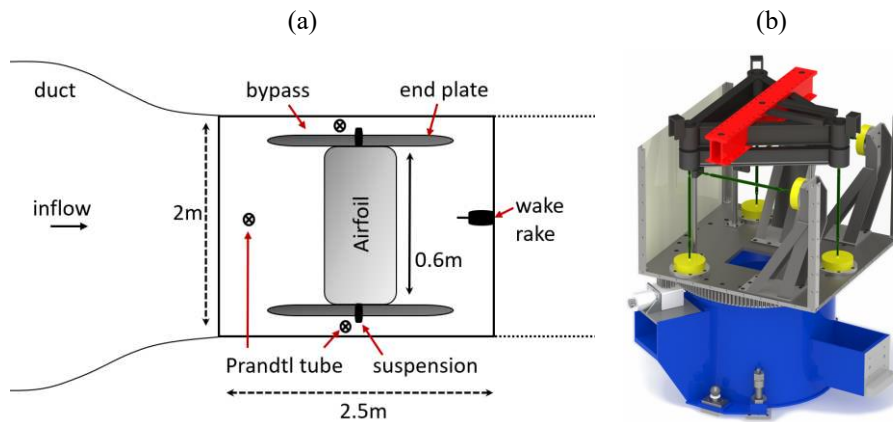


Figure 6. (a) Airfoil test section in top view. (b) Force balance underneath the test section in side view, load cells in yellow.

275 The inflow velocity is determined from the static pressure difference between the inlet and the outlet of the duct. For additional monitoring purposes, a Prandtl tube is mounted approximately $x = c = 100\%c$ upstream the airfoil LE. The airfoil model, or wing, is positioned in the centre of the box, as displayed in Figure 6a. It is enclosed by two smooth end plates, or splitter walls, that are parallel to the tunnel in order to minimize the influence of the wall BL. The velocities inside the 0.25 m wide bypass channels are measured via two separate Prandtl tubes to obtain the effective inflow or reference velocity. The suspension is decoupled from the end plates and the tunnel walls. Hence, the wing is directly mounted to the platform of the permanently
 280 installed force balance underneath the test section, see Figure 6b. The AoA is controlled by means of a stepping motor with an accuracy of 0.1° , which is part of the suspension. The airfoil models include the NACA63(3)618, the AH93W174 and the DU97W300, see Figure 4. All three wings were CNC milled from a solid block of ObomodulanTM, as described by Pechlivanoglou (2013). The chord length is 0.6 m and the span is 1.54 m resulting in an aspect ratio of 2.56.



3.2 Measurement methods

3.2.1 Force balance

The lift, drag and side forces of the airfoil model are directly transferred to the six component force balance. The load cells consists of strain gauges generating voltage signals that are proportional to the incoming forces. Each signal is digitalized by a CompactDAQ System of National Instruments with a sampling rate of 5 kHz. The data is recorded using a LabVIEW user interface, including forces, velocities and environmental conditions, i.e. air density and kinematic viscosity, all of which are automatically converted to **average results**. The LabVIEW interface also contains the AoA control in terms of range, steps and measurement duration. According to Meyer et al. (2016), the uncertainty of the averaged c_l and c_d measurements is 0.2%. The $c_l(\alpha)$ results show good agreement with literature data, as discussed in Sect. 4. However, since its implementation in the wind tunnel, the current set-up has been characterized by elevated $c_d(\alpha)$ results. The reasons are the small gaps between the wing and the end plates leading to suction effects. Moreover, a turbulent BL is formed on the end plates triggering separation on the outer parts of airfoil model, i.e. in the vicinity of splitter walls. Both effects are 3D and therefore detected in the form of increased drag values, see Meyer (2000) and Meyer et al. (2016). For the purpose of this study, a wake rake is designed, constructed and implemented into the test section aiming at 2D drag measurements.

3.2.2 Wake rake

The wake rake method is widely recognized to determine 2D drag coefficients at pre-stall conditions, see Barlow et al. (1999) and the references given throughout Sect 4.

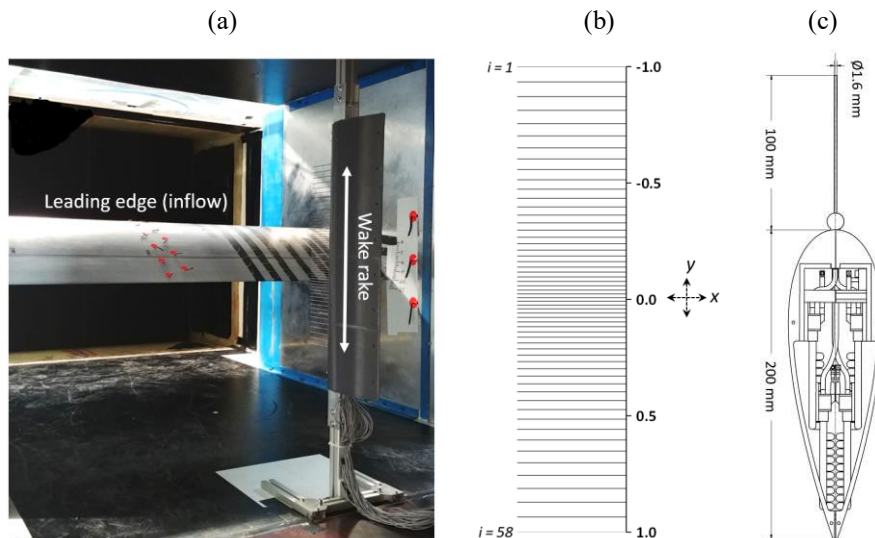


Figure 7. (a) Test section during wind tunnel measurements including airfoil model, one of the end plates and wake rake. (b) Normalized vertical rake tube positions, y , and numbering, i , in side view. (c) Cross section of wake rake casing and pressure tube in top view.



Figure 7a shows the present wake rake, which is positioned downstream the airfoil trailing edge at $x = c = 0.6$ m. This distance is necessary for the flow to return to the static pressure level in the wind tunnel, see Barlow et al. (1999). Figure 7b illustrates that the rake consists of a straight vertical line of 58 pitot tubes, each measuring the total pressure, p_{total} . The normalized vertical positions are defined as $y = 0.0$ for the center, $y_{i=1} = -1.0 = -250$ mm for the uppermost tube and $y_{i=58} = 1.0 = 250$ mm for the lowest tube. The total rake span is 0.5 m. The spacing between the tubes is smallest towards the center with $\Delta y_{\text{min}} = 4$ mm, and widest towards top and bottom with $\Delta y_{\text{max}} = 16.5$ mm, i.e. the data resolution is highest towards the center. The 3D printed casing consists of the symmetrical NACA0030 profile, see Figure 7c. The distance between the LE and the orifice of each pitot tube is 100 mm, where the impact of the rake on the flow is considered negligible. The static pressure, p_{static} , is determined as the average value of two Prandtl tubes that are installed inside the downstream plane of the rake, one on top and one below the casing. The differential pressure of each tube, $\Delta p(y_i)$, is measured with single HDOM010 sensors by First Sensor, which are installed inside the casing. They are connected with flexible silicon tubes, each shorter than 200 mm, in order to avoid dynamic feedback effects. The accuracy of each sensor is given with 0.1% of the full scale range of 1000 Pa under nominal conditions. At the constant inflow velocity of $u_{\text{inf}} = 40$ m/s, or $900 \text{ Pa} < \Delta p < 1000 \text{ Pa}$, the sensor accuracy is in the order of 1 Pa and therefore considered to be minor. The voltage signal is digitalized by a separate CompactDAQ system at a sampling rate of 10 kHz and recorded by a Labview user interface, both of which are decoupled from the DAQ system of the force balance, see Sect. 3.2.1. All sensors are calibrated by means of a mobile pressure calibration devices. Preparatory differential pressure tests in the empty test section show very good agreement between all rake sensors and the inflow Prandtl tube. After installing each airfoil model, the vertical center of the rake, $y = 0.0$, is roughly aligned with the maximum pressure loss at the corresponding design AoA. In this way, the static rake span covers the complete AoA range, $-5^\circ < \alpha < 17^\circ$, hence avoiding the installation of a vertical traversing system, see Figure 18. The raw data is post-processed using a specific Matlab script. The wake pressure loss and the drag coefficient are determined at each static AoA following Eq. (11) to (15).

1. The time-resolved total as well as static pressure is averaged in order to determine the differential pressure,

$$\Delta \bar{p}_i = \bar{p}_{\text{total}}(y_i) - \bar{p}_{\text{static}}, \quad (11)$$

where ρ refers to the air density in kg/m^3 and $i = 1, 2, \dots, 58$ to each rake tube.

2. The reference pressure of the free flow is calculated as the mean value of the two uppermost and the two lowest rake tubes, see Figure 7b, so that,

$$\Delta \bar{p}_{\text{ref}} = 0.25 \cdot (\Delta \bar{p}_1 + \Delta \bar{p}_2 + \Delta \bar{p}_{57} + \Delta \bar{p}_{58}). \quad (12)$$

The pressure coefficient, c_{pi} , is defined as,

$$c_{pi} = \frac{\Delta \bar{p}_i}{\Delta \bar{p}_{\text{ref}}}, \quad (13)$$

describing the characteristic pressure loss at each AoA, see Figure 18.

3. The uncorrected total drag contribution of each rake tube, c_{di} , becomes,

$$c_{di} = \sqrt{c_{pi}} - c_{pi}. \quad (14)$$



4. The uncorrected total drag coefficient, $c_{d,raw}(\alpha)$, is numerically integrated over the spacing between the rake tubes using the trapezoid rule, so that,

$$c_{d,raw}(\alpha) = \frac{1}{c} \sum_{i=1}^{58} (c_{di} + c_{di+1}) \cdot (y_{i+1} - y_i), \quad (15)$$

where c is the airfoil chord length and y_i the normalized position of each rake tube, as illustrated in Figure 7b.

3.2.3 Wind tunnel correction

335 The 2D airfoil performance is modified by the wind tunnel walls compared to equivalent free flow conditions. The reasons for that are: 1. the solid blockage effect leading to the constriction of the curved streamlines around the airfoil model and 2. the wake blockage effect leading to the constriction of the curved streamlines in the wake. Following Barlow et al. (1999), the total blockage, ε , is the sum of the solid and the wake blockage factors,

$$\varepsilon = \varepsilon_{solid} + \varepsilon_{wake} = \Lambda \frac{\pi^2}{48} \left(\frac{c}{h_{wt}} \right)^2 + \frac{c}{4h_{wt}} c_{d,raw} = \Lambda \mu + \frac{c}{4h_{wt}} c_{d,raw}, \quad (16)$$

for $\varepsilon > 0$,

340 where Λ refers the so-called body shape factor, which is related to the maximum airfoil thickness, $h_{wt} = 1.44 \text{ m}$, which is the height of the test section. Moreover, $\mu = \frac{\pi^2}{48} \left(\frac{c}{h_{wt}} \right)^2$ is introduced as an auxiliary constant.

Based on Eq. (16), the blockage correction is applied on the following parameters at each static AoA,

$$c_d = c_{d,raw}(1 - 3\varepsilon_{solid} - 2\varepsilon_{wake}), \quad (17)$$

$$c_l = c_{l,raw}(1 - \mu - 2\varepsilon), \quad (18)$$

$$Re = Re_{raw}(1 + \varepsilon), \quad (19)$$

$$\alpha = \alpha_{raw} + \frac{57.3\mu}{2\pi} (c_{l,raw} + 4c_{m,raw}), \quad (20)$$

$$c_m = c_{m,raw}(1 - 2\varepsilon) + 4\mu c_l, \quad (21)$$

where c_m refers to the moment coefficient at $0.25c$.

Eq. (17) to (20) are directly implemented into the data post-processing Matlab script.

345 3.3 Test matrix

The inflow velocity, $u_{inf} = 40 \text{ m/s}$, corresponds to a constant Re number of approximately $1.5 \cdot 10^6$. The free stream turbulence intensity of the empty wind tunnel is estimated with the inflow Prandtl tube and amounts to less than 0.3 %. The AoA ranges from $-5^\circ < \alpha < 17^\circ$, in steps of 1° . At each static AoA, there is a buffer of 4 s for the flow to settle, after which data is recorded for another 5 s. Hence, the total number of samples is $n = 5 \cdot 10^4$ for each rake sensor and $n = 2.5 \cdot 10^4$ for each load cell of the force balance. Before each test run, all sensors are subjected to a zero-offset measurement at standstill in order to reduce experimental errors.

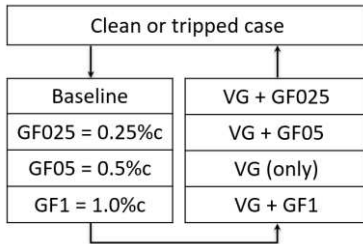


Figure 8. Test matrix and designation of all tested configurations.

Figure 8 summarizes the sequence of measurements for each airfoil starting with the clean baseline and followed by the three GF (only) configurations. Next, the VG array is installed and tested in combination with GF1. Subsequently, GF1 is removed in order to test VG (only), followed by the remaining configurations, VG + GF05 and VG + VG025. In the next round, ZZ tape is attached and the test matrix is repeated. Each complete cycle, clean or tripped, is measured during the same day, i.e. within less than 24 h, for the environmental conditions to remain as constant as possible.

4. Experimental results

The wind tunnel results are presented separately for the NACA63(3)618 (mid to tip blade region) and the DU97W300 (root to mid blade region). For clarity, the results of the AH93W174 are included as Appendix A. The baseline measurements consist of the clean and the tripped cases. They are compared to literature data in order to validate the experimental set-up. Next, different combinations of MGFs and VGs are assessed by means of characteristic parameters, i.e. the lift performance, the stall behavior and the aerodynamic efficiency.

4.1 NACA63(3)618

4.1.1 Baseline

Figure 9 shows the clean and the tripped polar curves. The drag results are valid until stall at $\alpha_{cl,max} = 10.5^\circ$ and the lift curves are measured until the post-stall AoA of 18.5° , see Figure 9a. As expected, ZZ tape with $h_{ZZ} = 0.4$ mm manifests itself in a lift decrease, coupled with a significant drag increase. The design point decreases from $\alpha_{opt, clean} = 6.4^\circ$ to $\alpha_{opt, ZZ} = 5.4^\circ$ and the corresponding aerodynamic efficiency drops from $L/D_{max, clean} = 109$ to $L/D_{max, ZZ} = 60$, see Figure 9b. For clarity, characteristic lift and L/D values are summarized in Table 5.

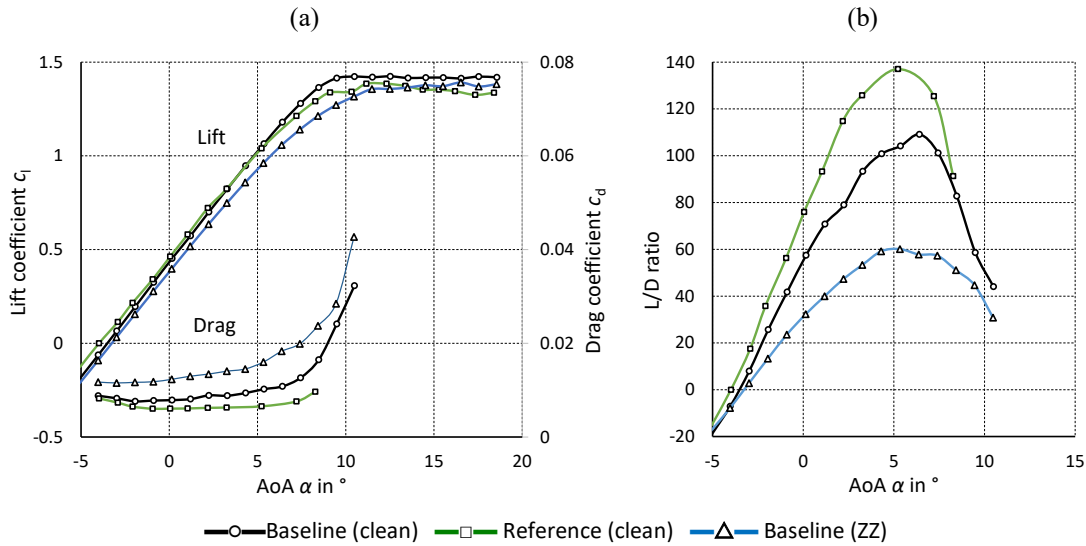


Figure 9. NACA63(3)618. Clean and tripped baseline cases at $Re = 1.5 \cdot 10^6$ compared to reference data from Abbott and von Doenhoff (1959) at $Re = 3 \cdot 10^6$. (a) Lift and drag coefficients. (b) L/D ratio.

375 The clean baseline measurements are compared to literature data from the airfoil catalogue of Abbott and von Doenhoff (1959). The NACA63(3)618 was tested at the closed-throat NASA Langley low turbulence pressure wind tunnel. The inflow turbulence was below 0.005 % at $Re = 3.0 \cdot 10^6$. Lift was determined by means of the reaction pressure difference between wind tunnel floor and ceiling and drag with a wake rake, both including wall and blockage corrections. Figure 9a shows good agreement between the lift curves. The separation points, $\alpha_{cl,max}$, and the design points, α_{opt} , are very similar, even though $c_{l,max}$ is slightly more elevated compared to the reference, which is probably due to the different measurement methods. The smaller drag and thus higher L/D results are explained by the fact that, in the reference case, double the Reynolds number is applied, see Figure 9b. Besides, the inflow turbulence is significantly stronger in case of the current measurements leading to earlier transition at elevated AoA and thus higher drag values.

4.1.2 Mini Gurney flaps

385 Timmer and van Rooij (2003) and Fuglsang et al. (2003) report no significant changes comparing the effect of rectangular and triangular GFs of identical height, apart from minor differences in drag. In order to verify this observation, the NACA63(3)618 is equipped with both GF profiles, as previously illustrated in Figure 1a: thin angle sections made of brass versus isosceles triangles made of a standard thermoplastic material. Figure 10 compares the lift over drag in both the clean and the tripped cases looking at each GF configuration separately. It is noted that the smallest triangular size, $h_{MGF,\Delta} = 0.33 \%c$ is larger than the corresponding rectangular profile, $h_{MGF,L} = 0.25 \%c$, see Figure 10a. Overall, all wedge shaped profiles shows a slight decrease in both lift and drag, which is visible in terms of GF05 and GF1, see Figure 10b and c. Nonetheless, the agreement between the two profiles is considered satisfying. In the remainder of this report, all GF configurations refer to the rectangular, or L-shaped, profile.

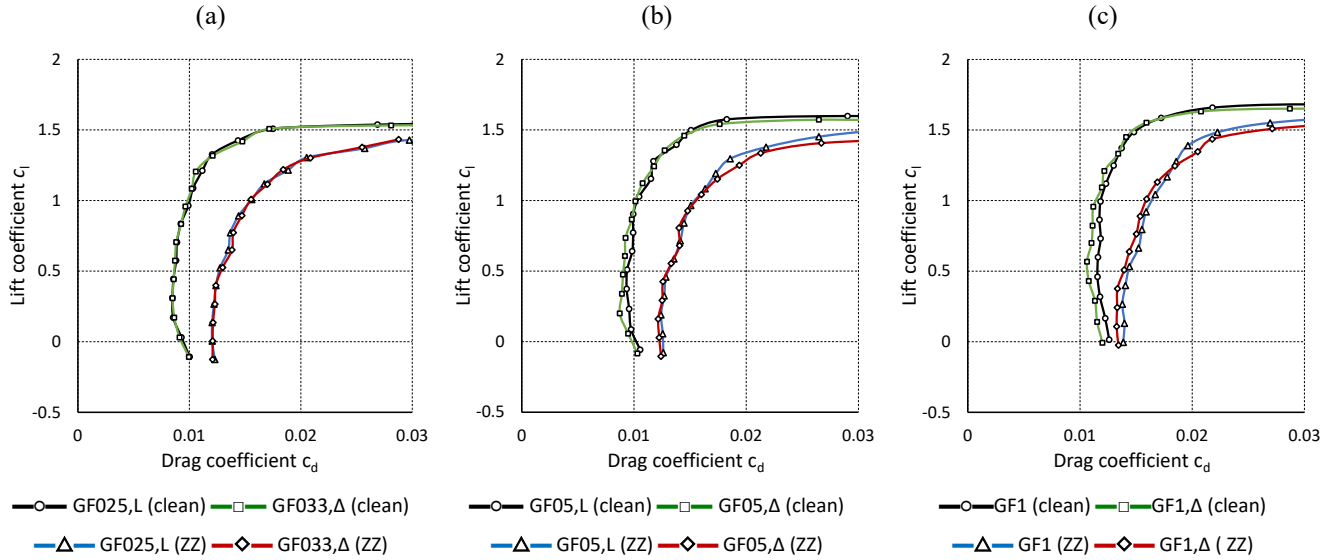


Figure 10. NACA63(3)618. Rectangular (L) versus triangular (Δ) Gurney flap profiles. Lift over drag curves in clean and tripped cases (a) $h_{MGF,L} = 0.25\%$ and $h_{MGF,\Delta} = 0.33\%$. (b) $h_{MGF} = 0.5\%$. (c) $h_{GF} = 1\%$.

Next, Figure 12a displays the pressure deficit or momentum loss in the wake of the GF configurations based on Eq. (13), which is then converted into the drag coefficients. In the clean case, at $\alpha_{opt} = 6.4^\circ$, the c_{pi} curves correspond to attached flow. As expected, the pressure deficit and thus drag is increased in relation to the GF height. Moreover, the position of the horizontal centerline of the wake dent is characteristic for the downwash angle, which is proportional to lift, as discussed in Sect. 1.2. Hence, the minimum of the c_{pi} curves descend towards the wind tunnel floor for increased GF heights. In the tripped case, the wake pressure deficit is more pronounced due to higher drag, and the downwash angle is smoother due to lower lift values, see Figure 12b.

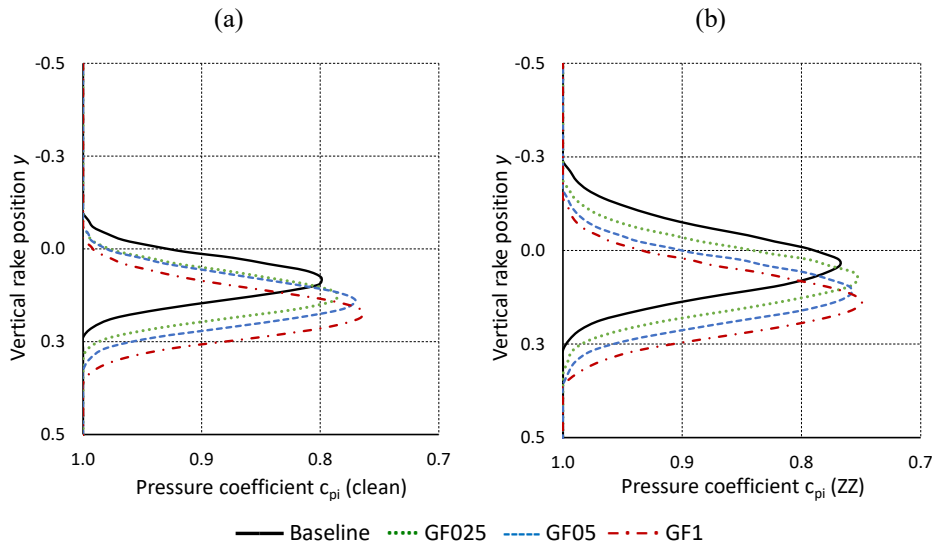




Figure 11. NACA63(3)618 at $\alpha = 6.4^\circ$. Gurney flaps. Pressure coefficients over vertical wake rake positions. (a) Clean case. (b) Tripped case.

Furthermore, the fluctuations of the wake pressure measurements are determined via the standard deviation of the raw data,

$$\sigma_{pi} = \sqrt{\frac{1}{n-1} \sum_{i=1}^n |\Delta p_i - \Delta \bar{p}_i|^2}, \quad (22)$$

where $n = 5 \cdot 10^4$ is the number of samples of each pressure sensor and $\Delta \bar{p}_i$ refers to the average differential pressure at each AoA, see Eq. (11).

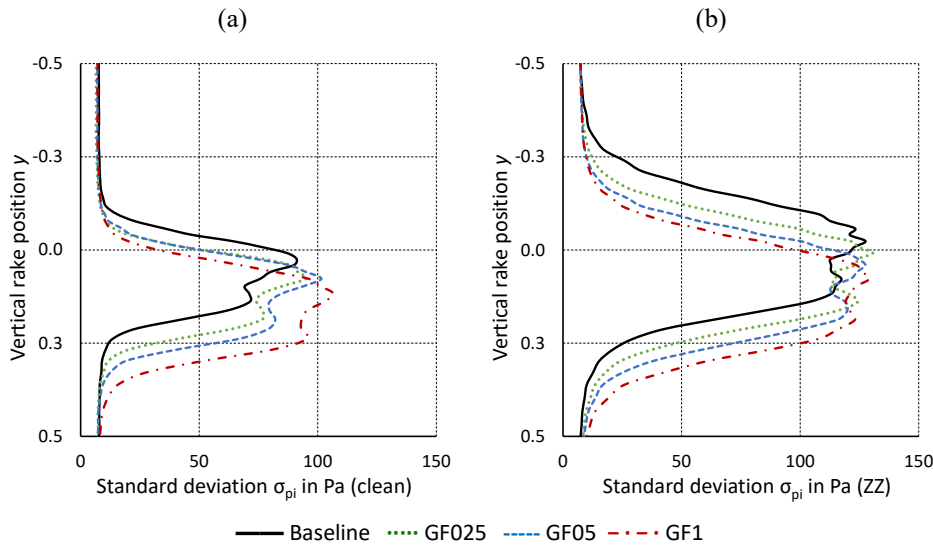


Figure 12. NACA63(3)618 at $\alpha = 6.4^\circ$. Gurney flaps. Standard deviation of raw pressure data over vertical wake rake positions. (a) Clean case. (b) Tripped case.

Figure 12a shows that, in the clean case, the intensity of the wake unsteadiness is dependent on the GF height. Despite the offset due to the higher downwash angle, the σ_{pi} curves are very similar between the clean baseline and the MGF configurations, as predicted by Bechert et al. (2000) and Schatz et al. (2004b), see Sect. 1.2. Moreover, Figure 12b shows that σ_{pi} is much more pronounced in the tripped baseline case because of the thicker and more turbulent BL, so that the contribution of all GF configurations to σ_{pi} appears to be marginal.

Next, Figure 13 illustrates the polar curves of all GF configurations referring to the NACA63(3)618. Depending on the GF height, both lift and drag is increased. Compared to the respective baseline, the shape of the polar curves and the stall behaviour is maintained, so that $\alpha_{opt, clean} = 6.4^\circ$, $\alpha_{opt, ZZ} = 5.4^\circ$ and $\alpha_{cl, max} = 10.5^\circ$ in both the clean and the tripped cases. For clarity, characteristic lift and L/D values are summarized in Table 5.

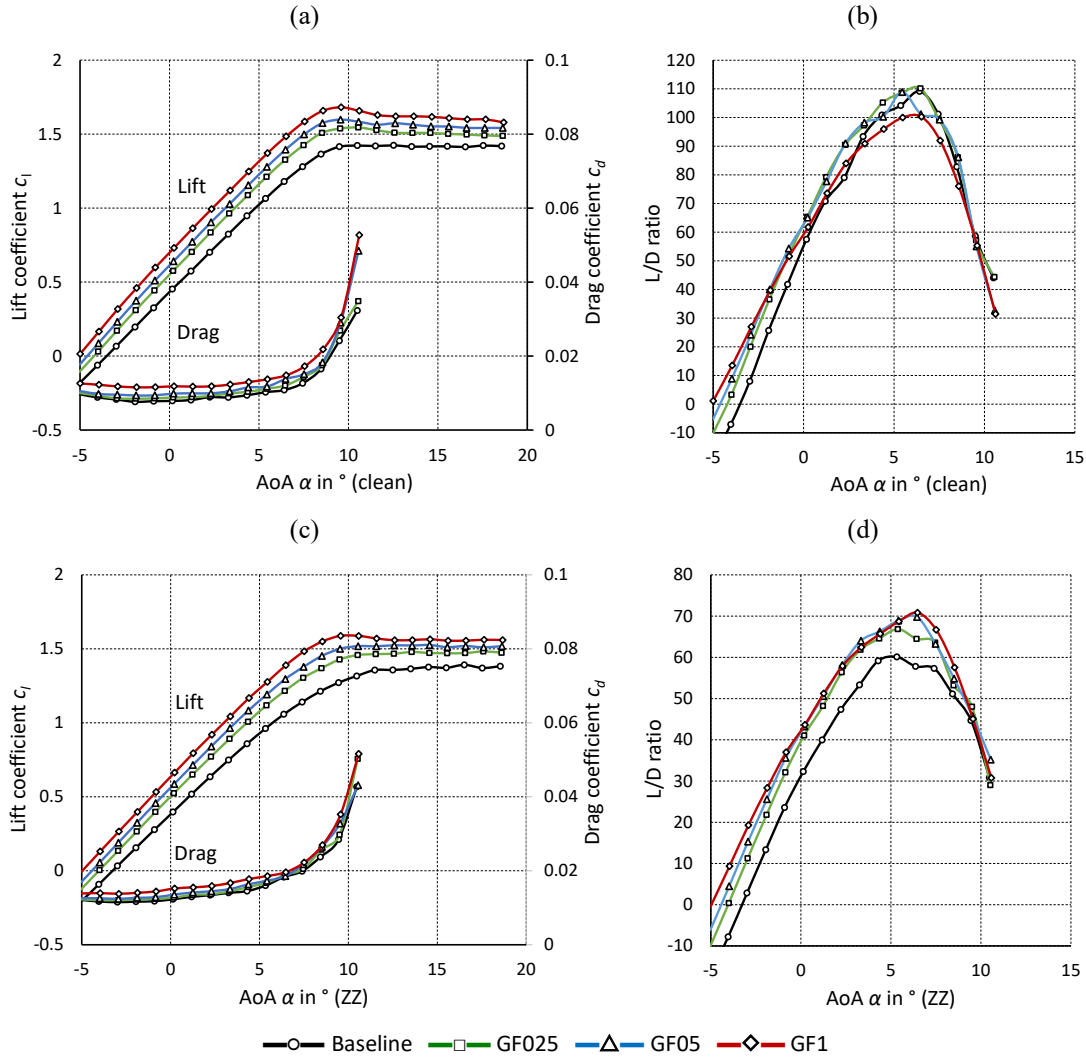


Figure 13. NACA63(3)618. Gurney flaps. (a) Lift and drag coefficients (clean). (b) L/D ratio (clean). (c) Lift and drag coefficients (ZZ). (d) L/D ratio (ZZ).

Table 5. NACA63(3)618. Gurney flaps. Characteristic values.

	Clean		Tripped	
	$c_{l,max}$ (10.5°)	L/D_{max} (6.4°)	$c_{l,max}$ (10.5°)	L/D_{max} (5.4°)
Baseline	1.42	109	1.32	60
GF025	1.54	110	1.46	67
GF05	1.58	101	1.52	69
GF1	1.66	100	1.59	69

Looking at the clean cases, Figure 13b illustrates that $L/D_{max, clean}$ is slightly improved by GF025 and GF05. As such, GF025 provides the preferred results, while GF1 leads to an overall $L/D(\alpha)$ decrease. In the tripped cases, the aerodynamic efficiency

is improved by all GF heights, see Figure 13d and Table 5. As discussed in Sect. 2.4, the local BL expands significantly due to forced LE transition, so that larger GFs appear to be more beneficial.

4.1.3 Vortex generators plus Mini Gurney flaps

Figure 14 illustrates the polar curves of all VG + GF configurations. Looking at the VG (only) cases, stall is delayed by around 2°, coupled with a substantial increase in $c_{l,max}$, see Figure 14a. Furthermore, VGs lead to a more abrupt stall behaviour and thus adverse load excursions, as previously reported by Mueller-Vahl et al. (2012). In all combined cases, the GF is added to the VG effect as a constant lift and drag increase. For clarity, characteristic lift and L/D values are summarized in Table 6.

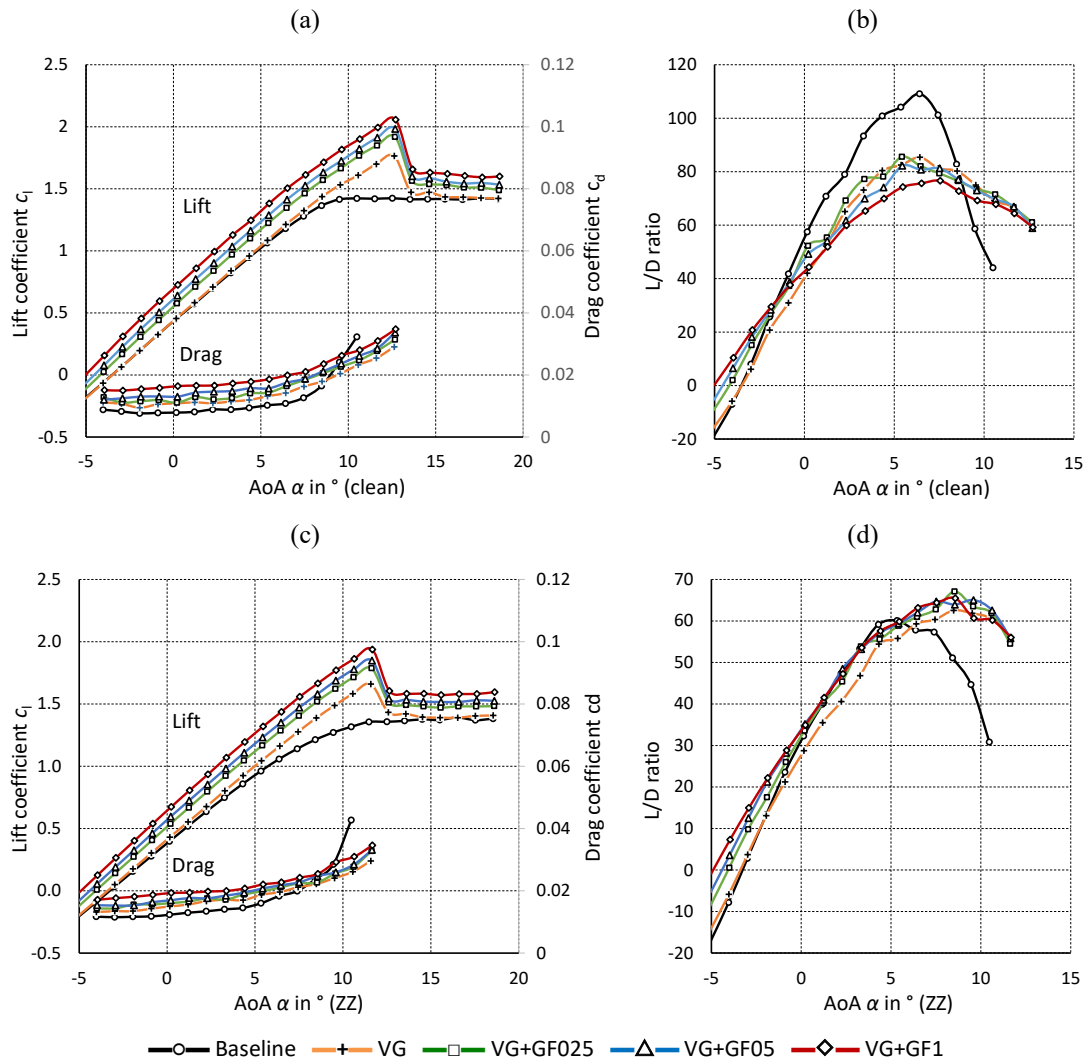


Figure 14. NACA63(3)618. Vortex generators and Gurney flaps. (a) Lift and drag coefficients (clean). (b) L/D ratio (clean). (c) Lift and drag coefficients (ZZ). (d) L/D ratio (ZZ).



435 Table 6. NACA63(3)618. Vortex generators plus Gurney flaps. Characteristic values.

	Clean		Tripped	
	$c_{l,max}(\alpha)$	$L/D_{max}(\alpha)$	$c_{l,max}(\alpha)$	$L/D_{max}(\alpha)$
Baseline	1.42 (10.5°)	109 (6.4°)	1.32 (10.5°)	60 (5.4°)
VG	1.76 (12.7°)	85 (6.4°)	1.66 (11.6°)	63 (8.5°)
VG+GF025	1.92 (12.7°)	82 (6.4°)	1.79 (11.6°)	67 (8.5°)
VG+GF05	1.98 (12.7°)	81 (6.4°)	1.85 (11.6°)	64 (8.5°)
VG+GF1	2.06 (12.7°)	76 (6.4°)	1.94 (11.6°)	65 (8.5°)

According to Figure 14a and c, drag is reduced at elevated AoA due to the effect of stall delay. However, in the clean case, the drag penalty at low and moderate AoA causes $L/D_{max, clean}$ to decrease. Hence, the preferred results are achieved for VG + GF025 compared to the remaining configurations, see Figure 14b. Under tripped conditions, all PFC devices are capable of
 440 maintaining L/D at low and moderate AoA. Moreover, $L/D_{max, ZZ}$ increases significantly, as it is shifted by around 2° and thus recovering a wide area of otherwise separated flow in the range of $6.5^\circ < \alpha < 11.6^\circ$, see Figure 14d. Again, VG + GF025 is the preferred configuration. Overall, the polar graphs indicate that the VG is superposed by the GF effect. In fact, looking at both the lift and the L/D curves of Figure 14, the combined cases prove to be beneficial compared to the VG (only) configurations. The reason for this phenomenon is suspected to be the beneficial wake flow interaction between both PFC devices, as
 445 previously illustrated in Figure 5 and further discussed in the following section.

4.2 DU97W300

4.2.1 Baseline

Figure 15 illustrates the clean and the tripped polar curves. In the tripped case, the stall angle decreases from $\alpha_{cl,max, clean} = 12.6^\circ$ to $\alpha_{cl,max, ZZ} = 10.4^\circ$ and the design AoA from $\alpha_{opt, clean} = 9.5^\circ$ to $\alpha_{opt, ZZ} = 7.4^\circ$, see Figure 15a. Hence, using $h_{ZZ} = 0.3\text{mm}$,
 450 separation is initiated early, in fact only 1° below $\alpha_{opt, clean}$. As a result, the aerodynamic efficiency drops from $L/D_{max, clean} = 88$ to $L/D_{max, ZZ} = 41$, see Figure 15b. For clarity, characteristic lift and L/D values are summarized in Table 7.

The baseline measurements are compared to reference data of the DU, see Timmer and van Rooij (2003). The DU97W300
 was tested in the closed-loop low turbulence wind tunnel. The free stream turbulence is 0.07 % at $Re = 3 \cdot 10^6$. Lift was
 455 determined from the measured surface pressure distribution and drag by means of a wake rake positioned 60 %c downstream the airfoil TE, including wall and blockage corrections. Forced LE transition was triggered by $h_{ZZ} = 0.35\text{mm}$ at $x_{SuS} = 5.0\%c$ and $h_{ZZ} = 0.25\text{mm}$ at $x_{PS} = 20.0\%c$, i.e. very similar to the current configuration.

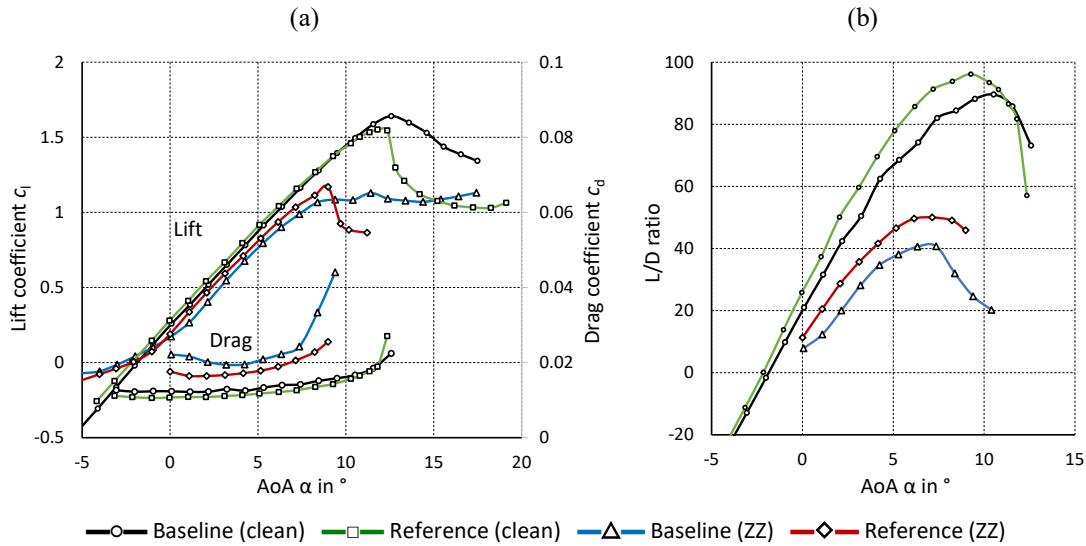


Figure 15. DU97W300. Clean and tripped baseline cases at $Re = 1.5 \cdot 10^6$ compared to reference data from Timmer and van Rooij (2003) at $Re = 3 \cdot 10^6$. (a) Lift and drag coefficients. (b) Lift to drag ratio.

Figure 15a shows good agreement between the lift curves, including $\alpha_{cl,max}$. In both cases, the reference curves are characterized by a more abrupt stall behaviour compared to the current measurements. The smaller drag and thus larger L/D values are explained by the higher Re number of the reference measurements, see Figure 15b. It is noted that both drag curves show abrupt PS separation at negative AoA due to the ZZ tape, which are not displayed in Figure 15a. In a related publication, van Rooij and Timmer (2003) report the following specific values of the clean DU97W300 baseline at $Re = 2 \cdot 10^6$ rather than $3 \cdot 10^6$: $c_{l,max} = 1.55$ and $L/D_{max} = 91.7$. This is in excellent agreement with the current measurements at $Re = 1.5 \cdot 10^6$: $c_{l,max} = 1.64$ and $L/D_{max} = 89.5$.

4.2.2 Mini Gurney flaps

Figure 16 shows the polar curves of all GF configurations, which reinforce the observations presented in Sect. 4.1.2: 1. the shape of the polar curves is basically maintained, 2. the lift and drag increase depends on the GF height, and 3. the beneficial GF effect on L/D (α) is more pronounced in the tripped case. For clarity, characteristic lift and L/D values are summarized in Table 7.

Figure 16b illustrates that, in the clean case, the aerodynamic efficiency is kept on a similar level applying either of the MGFs, whereas $L/D_{max, clean}$ is decreased using GF1. The performance deterioration due to forced LE transition is alleviated by all GFs, with GF05 achieving the preferred results in terms of $L/D_{ZZ}(\alpha)$, see Figure 16d and Table 7.

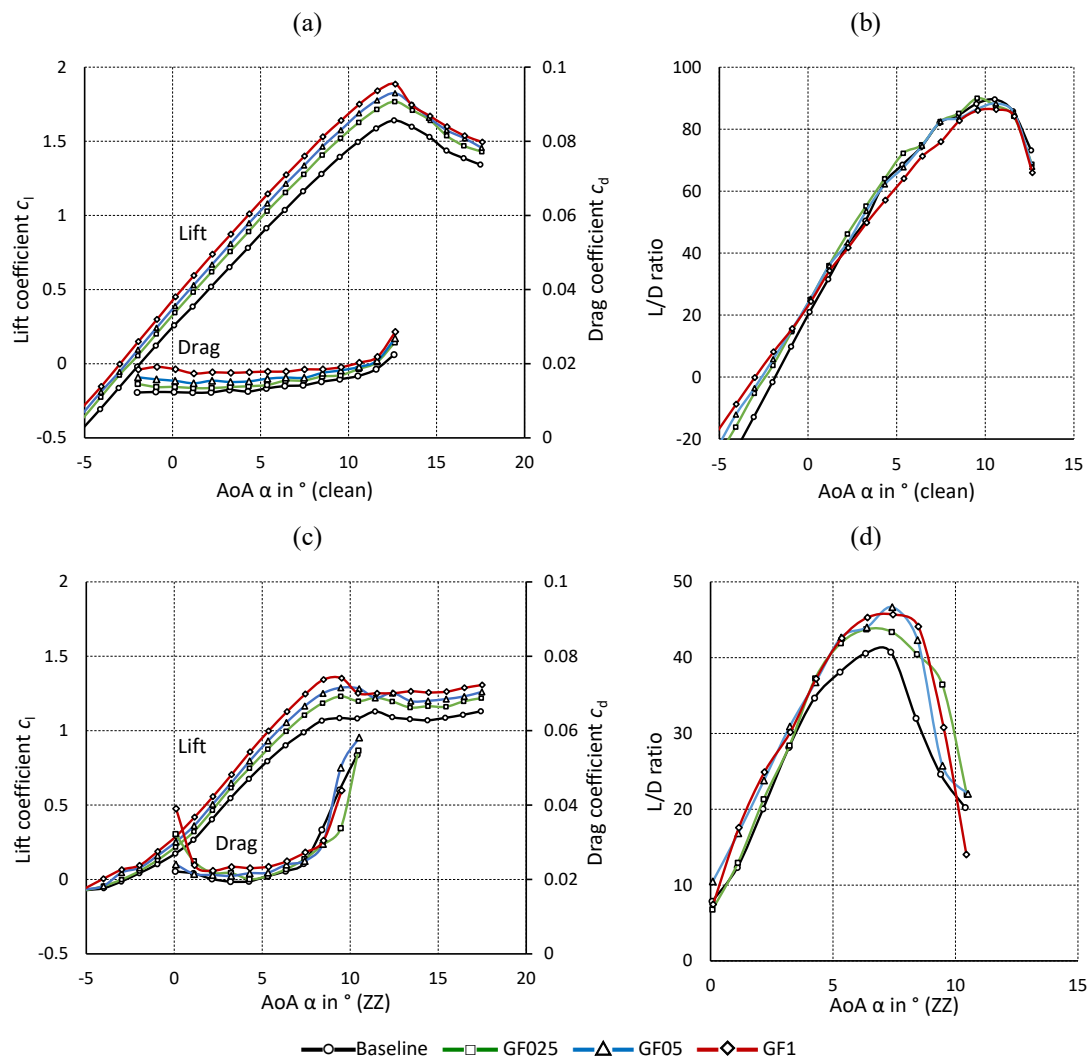


Figure 16. DU97W300. Gurney flaps. (a) Lift and drag coefficients (clean). (b) L/D ratio (clean). (c) Lift and drag coefficients (ZZ). (d) L/D ratio (ZZ).

480 Table 7. DU97W300. Gurney flaps. Characteristic values.

	Clean		Tripped	
	$c_{l,max}$ (12.6°)	L/D_{max} (9.5°)	$c_{l,max}$ (10.4°)	L/D_{max} (7.4°)
Baseline	1.64	88	1.08	41
GF025	1.77	90	1.20	43
GF05	1.82	87	1.28	47
GF1	1.89	86	1.25	46



4.2.3 Vortex generators plus Mini Gurney flaps

The flow field in the wake of GFs is considered 2D at pre-stall operation, see Sect. 1.2. As opposed to that, VGs induce counter-rotating vortices into the BL that are released as scattered 3D structures into the TE wake, see Figure 5b. Hence, the VG effect is registered in the form of spanwise oscillations of the drag measurements by the wake rake, as reported by Baldacchino et al. (2018). The amplitude of these oscillations depend on both the size and the position of the VG array, the distance between the wake rake and the airfoil TE as well as the operational conditions, i.e. Re , AoA and inflow turbulence intensity. Figure 17 displays the spanwise dependency of the current drag measurements. In accordance with Figure 3b, position 0 stands for 0D, i.e. in the airfoil center and right in-between the VG vanes. At position 1, the rake is shifted $0.25D = 11.4$ mm in the spanwise direction and position 2 refers to $0.5D = 22.8$ mm, i.e. right in between two adjacent VGs.

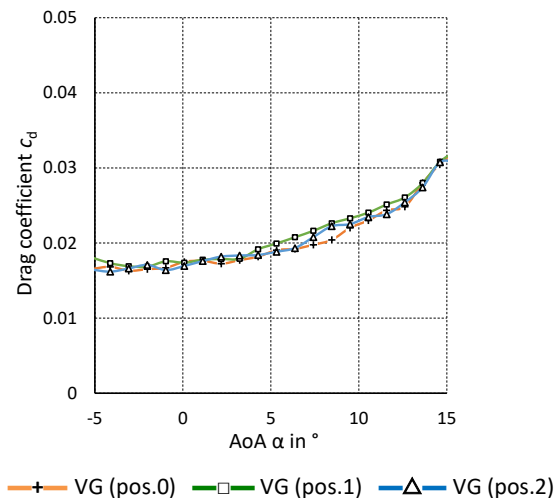


Figure 17. DU97W300. Clean VG (only) configurations. Drag measurements for different spanwise wake rake positions.

Figure 17 shows that the influence of the spanwise rake positions on the drag results is marginal at the relatively large distance of 100 %c between airfoil TE and rake tubes. Hence, all drag results that are presented in this report refer to the center position of the rake, i.e. the spanwise position 0.

Next, Figure 18 shows the pressure deficit or momentum loss in the wake of all clean VG + GF configurations. Figure 18a captures the pressure distribution at the design AoA , $\alpha_{opt, clean} = 9.5^\circ$. All configurations are characterized by attached flow, so that the wake deficit and thus the drag coefficients are relatively small. The pre-stall lift increase due to the GFs is directly related to the downwash angle, as discussed in Sect. 4.1.2. Figure 18b illustrates the situation at $\alpha_{cl, max} = 12.6^\circ$, where the baseline curve indicates that separation is initiated. The wake deficit extends towards the upper side of the rake due to the formation of the TE separation bubble on the airfoil SuS. At the same time, the VG + GF configurations delay separation leading to a much smaller wake deficit compared to the baseline.

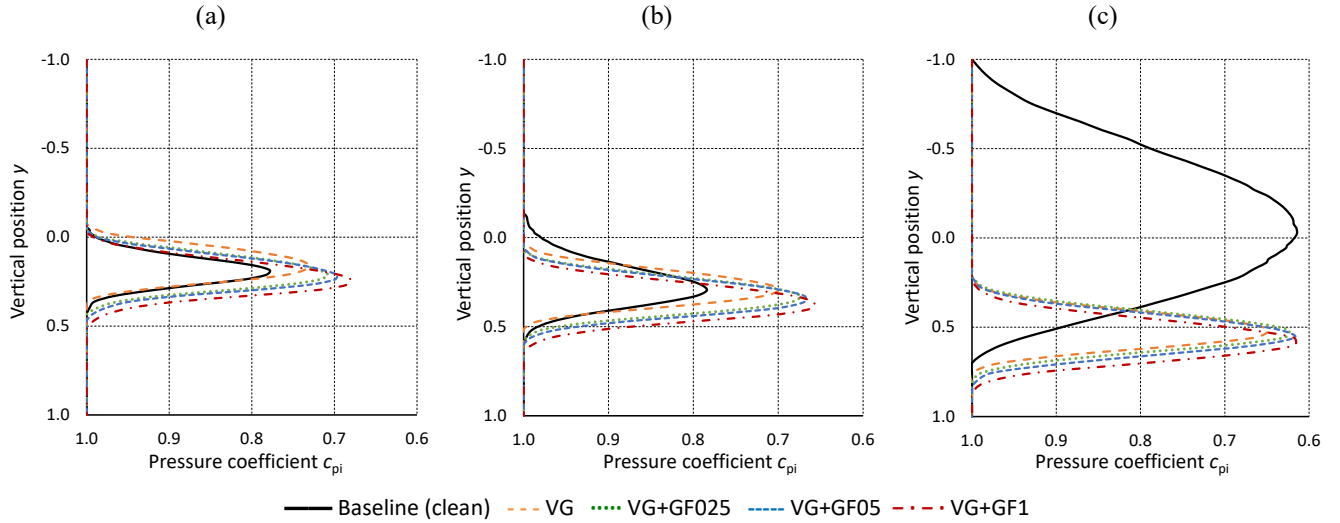


Figure 18. DU97W300. Pressure coefficients over vertical wake rake positions in the clean case. Vortex generators and Gurney flaps. (a) $\alpha_{\text{opt}} = 9.5^\circ$. (b) $\alpha_{\text{cl,max}} = 12.6^\circ$. (c) $\alpha = 16.5^\circ$.

At $\alpha = 16.5^\circ$, the baseline airfoil is clearly stalling, see Figure 18c. At this point, the wake consists of separated flow, i.e. 3D structures that cannot be determined accurately by means of wake rake measurements anymore. However, the VG + GF configurations suppress the formation of stall cells so that the flow remains attached, as described by Manolesos and Voutsinas (2015). Finally, at $\alpha = 17.5^\circ$, which is not displayed here, the flow separates abruptly leading to a steep decline of the lift curves, as illustrated in Figure 19a. These load excursions are perceptible in the form of strong mechanical vibrations of the set-up as well as a heavy roaring sound inside the wind tunnel. In summary, the wake deficit remains similar in shape and amount comparing the VG (only) to the combined configurations, again pointing towards a favorable wake interaction between VGs and MGFs.

Figure 19 displays the polar curves of all VG + GF configurations. For clarity, characteristic lift and L/D values are summarized in Table 8. The results of both the baseline and the VG (only) configurations are in very close agreement with reference measurements of the DU. Baldacchino et al. (2018) tested a comprehensive variety of VG configurations including $h_{\text{VG}} = 0.8\%c$ at $x_{\text{VG}} = 30\%c$ and $Re = 2 \cdot 10^6$. However, the tripped case consists of SuS (only) ZZ tape with $h_{\text{ZZ}} = 0.17 \text{ mm}$ at $x_{\text{ZZ}} = 5.0\%c$, which explains the elevated $L/D_{\text{max,ZZ}}$ compared to the current measurements, as detailed in Table 8. Next, The VG + GF configurations show that stall is delayed by around 4° coupled with a significant $c_{l,\text{max}}$ increase, again, followed by an abrupt and steep drop at stall, see Figure 19a and c. Despite the improved drag behavior at elevated AoA, the combined drag penalty causes L/D_{clean} to decrease significantly at low and moderate AoA. Overall, the results of the VG + MGFs are preferred over the VG + GF1 due to the beneficial L/D distribution, see Figure 19b. Under tripped conditions, all PFC devices are capable of maintaining L/D at low and moderate AoA. Moreover, $L/D_{\text{max,ZZ}}$ is increased as it is shifted by around 5° recovering a large area of otherwise separated flow in the range of $7.4^\circ < \alpha < 15.6^\circ$, see Figure 19d. Again, VG + MGFs are the preferred configurations.

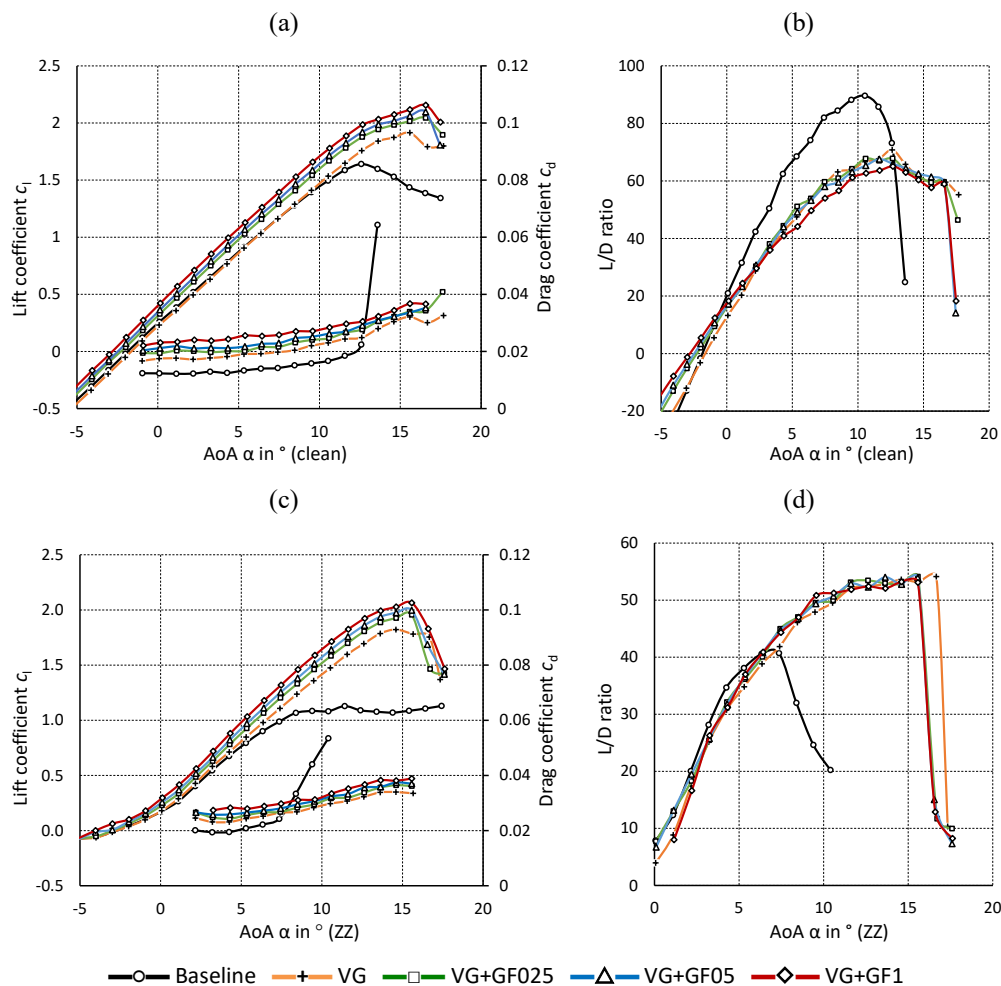


Figure 19. DU97W300. Vortex generators and Gurney flaps. (a) Lift and drag coefficients (clean). (b) L/D ratio (clean). (c) Lift and drag coefficients (ZZ). (d) L/D ratio (ZZ).

Table 8. DU97W300. Vortex generators plus Gurney flaps. Characteristic values. Reference data (ref.) is estimated based on Baldacchino et al. (2018).

	Clean		Tripped	
	$c_{l,max}(\alpha)$	$L/D_{max}(\alpha)$	$c_{l,max}(\alpha)$	$L/D_{max}(\alpha)$
Baseline	1.64 (12.6°)	88 (9.5°)	1.13 (11.4°)	41 (7.4°)
Baseline (ref.)	1.53 (12.4°)	91 (9.3°)	1.11 (9.2°)	50 (6.2°)
VG	1.91 (15.6°)	71 (12.6°)	1.82 (14.6°)	52 (12.6°)
VG (ref.)	1.95 (15.5°)	73 (11.3°)	1.87 (15.5°)	60 (10.0°)
VG+GF025	2.04 (16.6°)	68 (12.6°)	1.96 (15.6°)	53 (12.6°)
VG+GF05	2.10 (16.6°)	66 (12.6°)	2.00 (15.6°)	52 (12.6°)
VG+GF1	2.16 (16.6°)	65 (12.6°)	2.06 (15.6°)	52 (12.6°)

In summary, the DU97W300 measurements confirm the observations based on both the NACA63(3)618, see Sect. 4.1, and AH93W174, see Appendix A: the VG is superposed by the GF effect, resulting in beneficial aerodynamic effects.

5. Rotor blade performance

The most beneficial combination of PFC devices is selected on the basis of the wind tunnel results, see Sect. 4. The experimental polar data is imported into the software QBlade (Marten, 2020) in order to create a generic rotor blade. The blade performance is simulated by means of two case studies, the retrofit application on an existing, and the new design application on a alternative rotor blade.

5.1 Blade configurations

As illustrated in Figure 5a, it is reiterated that the VG and the MGF configurations refer to $Re = 1.5 \cdot 10^6$, $h_{ZZ} = 0.3$ mm and 0.4 mm, respectively, $h_{VG} = 1.1$ %c and $h_{MGF} = 0.25$ %c and 0.5%c, while $h_{GF} = 1.0$ %c is not considered relevant for this section of the report. Table 9 demonstrates the qualitative effect of the PFC devices on all tested airfoils by means of characteristic parameters.

Table 9. Performance evaluation of Mini Gurney flaps and vortex generators based on the wind tunnel tests of the NACA63(3)618, the AH93W174 and the DU97W300. ↑ for increase, ≈ for similar and ↓ for decrease.

	Clean			Tripped		
MGFs (only)	$c_l(\alpha_{opt}) \uparrow$	$\alpha_{cl,max} \approx$	$L/D_{max} \approx$	$c_l(\alpha_{opt}) \uparrow$	$\alpha_{cl,max} \approx$	$L/D_{max} \uparrow$
VG + MGF	$c_l(\alpha_{opt}) \uparrow$	$\alpha_{cl,max} \uparrow$	$L/D_{max} \downarrow$	$c_l(\alpha_{opt}) \uparrow$	$\alpha_{cl,max} \uparrow$	$L/D_{max} \uparrow$

The tendencies that are shown in Table 9 emphasize, first of all, that the effect of the PFC configurations is case dependent. In general, it is difficult to measure and to foresee the degree of LER, as described by Papi et al. (2021). For the purpose of this study, the principal objective is to improve the airfoil performance in the tripped case without jeopardizing the aerodynamic efficiency of the clean airfoil. Looking at the MGF (only) configurations, lift is increased at the design point and the stall behavior is basically consistent. The decambering effect of the ZZ tape is partly compensated for by the MGFs, as such improving the aerodynamic efficiency, while $L/D_{max, clean}$ is slightly improved or, at least, maintained. In the tripped case, VG + MGF achieve a triple improvement concerning lift increase, stall delay and aerodynamic efficiency. However, in the clean case, $L/D_{max, clean}$ decreases due to the combined drag penalty.

Apart from that, the principal objective of installing PFC devices on rotor blades is to enhance the energy yield over a life time of at least 20 years. Over time, the continuous development of adverse roughness effects is inevitable, as described by Maniaci et al. (2020) and Papi et al. (2021). Hence, in the mid to tip region, the driving parameters are the increase in both lift and



L/D_{\max} . In the root to mid region, stall delay and L/D_{\max} are considered particularly important. Based on Table 9, the selected PFC configurations in both the clean and the tripped cases are summarized in Table 10.

Table 10. Selected PFC configurations for generic rotor blade design

NACA63(3)618	GF025
AH93W174	GF025
DU97W300	VG + GF05

560

Concerning the NACA63(3)618 and the AH97W174, see Appendix A, GF025 is selected over GF05 as it is considered the more conservative option, especially in terms of $L/D_{\text{clean}}(\alpha)$. In case of the DU97W300, VG + GF05 is the preferred option due to the significant stall delay as well as lift increase. In principal, both MGF configurations, i.e. GF05 and VG + GF025 and vice versa, lead to similar results, indicating a certain tolerance regarding the choice of the exact MGF height, as long as Eq. (8) is fulfilled. It is noted that the AH93W174 is not included in the rotor blade design and performance simulations of the remaining Sect. 5.2 and 5.3.

5.2 Blade design

The experimental lift and drag polars are imported into the open source software QBlade. Figure 20 illustrates the rotor blade design of the NREL 5 MW reference wind turbine with $R = 63$ m, an average wind speed at hub height of $u_{\text{avg}} = 8$ m/s, and, according to Eq. (23), a design tip speed ratio (TSR) of $\lambda_{\text{opt}} = 8$, as specified by Jonkman et al. (2009). The NREL blade is used as a template for the so-called generic rotor blade, which is designed in order to identify the impact of the PFC configurations on the rotor performance of an aerodynamically optimized blade. It is scaled down to $R = 20$ m, $u_{\text{avg}} = 7$ m/s and $\lambda_{\text{opt}} = 7$, as such reaching Re numbers closer to the wind tunnel tests, which are in the range of $1.5 \cdot 10^6$ to $2 \cdot 10^6$ rather than $3 \cdot 10^6$ to $9 \cdot 10^6$.

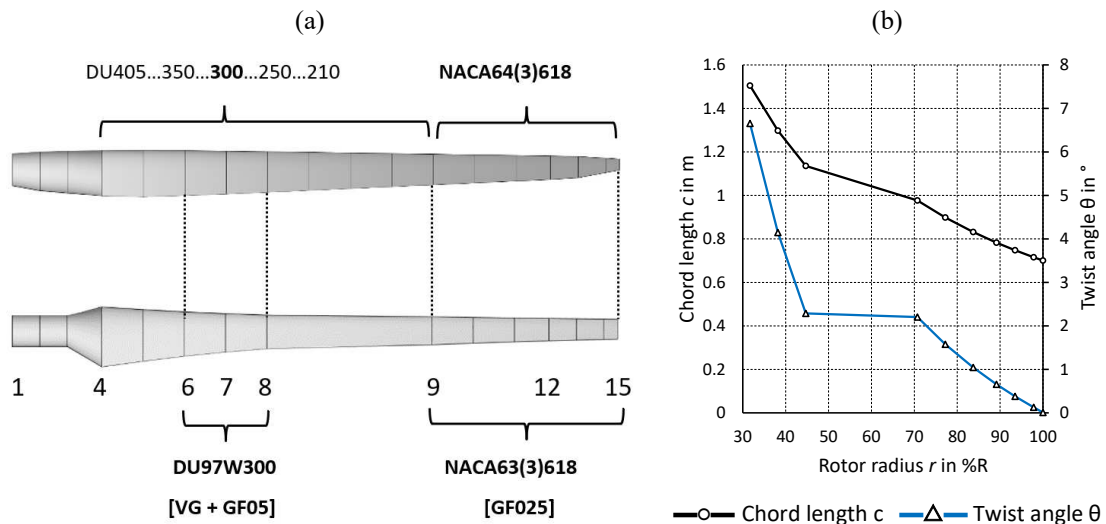




Figure 20. (a) Design of generic rotor blade based on the NREL 5 MW reference turbine. (b) Geometry of generic blade over rotor radius. Figure 20a illustrates that the DU97W300 is placed from blade position 6 to 8 and the NACA63(3)618 between position 9 to 15. The mid span region is simply interpolated between position 8 and 9. Figure 20b shows the chord length $c(r)$ and the twist angle $\theta(r)$ of the generic blade, both of which are determined by means of the aerodynamic blade optimization procedure of Schmitz (1956), as described by Gasch and Tvele (2012),

$$\lambda(r) = \frac{2\pi f r}{u_{avg}}, \quad (23)$$

where f is the rotational frequency in Hz and $\lambda(R) = \lambda_{opt}$.

$$c(r) = \frac{16\pi}{B} \cdot \frac{r}{c_l(\alpha_{opt}(r))} \cdot \sin^2\left(\frac{1}{3} \cdot \tan^{-1}\left(\frac{R}{\lambda_{opt} \cdot r}\right)\right), \quad (24)$$

$$\theta(r) = \varphi(r) - \alpha_{opt}(r) = \frac{2}{3} \cdot \tan^{-1}\left(\frac{R}{\lambda_{opt} \cdot r}\right) - \alpha_{opt}(r), \quad (25)$$

where B is the number of blades and $\varphi(r)$ the inflow angle in $^\circ$.

The Schmitz design, i.e. Eq. (24) and (25), leads to elevated chord lengths and twist angles in the root region due to the decreasing rotational speed and thus $\lambda(r)$, towards the blade root. For practical and logistical reasons, the chord length in the root region, i.e. $r < 30\%R$, is usually reduced in order to restrict the volume and weight of large rotor blades. Hence, the numerical results of the generic blade are only considered to be feasible between position 6 at $r = 31.7\%R$ and the very tip.

Besides, no specific tip design is implemented.

Next, two generic case studies are defined and presented. The first one consists of the retrofit application of PFC devices that are installed on an existing rotor blade during regular maintenance activities. The original blade design is based on a smooth surface, i.e. clean airfoil polars. Over time, LER effects reduce the aerodynamic efficiency and thus the AEP. Subsequently, VGs and GFs are installed in order to recover some of the decreased power output. The simulation parameters of the retrofit case, i.e. the blade geometry and all controller settings, are identical. The experimental polar data files of the clean, are replaced by the tripped baseline and, subsequently, by the tripped baseline including the PFC configurations, as illustrated in Figure 21.

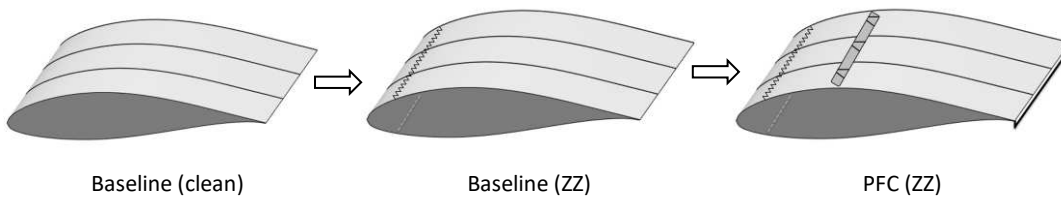


Figure 21. Retrofit application of passive flow control devices on a generic rotor blade section.

The second case study consists of the new design application of PFC devices that are installed as part of the blade manufacturing process on the ground. The original, i.e. clean blade, is adversely affected by LER, as shown in Figure 21. The performance is compared to an alternative blade configuration including the PFC devices as part of the design process itself, see Figure 22.

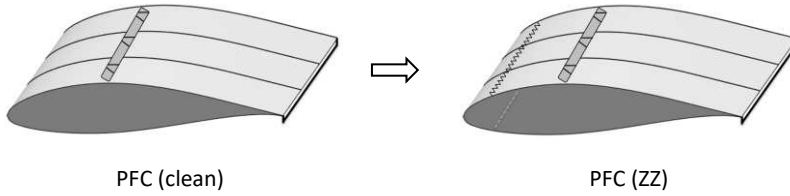


Figure 22. New design application of passive flow control devices on a generic rotor blade section.

The blade geometry, $c(r)$ and $\theta(r)$, is calculated separately for the clean baseline and the new blade including PFC devices. Applying Eq. (24) and for $R, \lambda_{\text{opt}}, B$ to be identical, the ratio between the chord length at each blade position, r , is inversely proportional to the corresponding lift coefficients at the design AoA,

$$\frac{c(r)}{c_{PFC}(r)} = \frac{c_{l,PFC}(\alpha_{\text{opt},PFC})}{c_l(\alpha_{\text{opt}})} \quad (26)$$

According to Eq. (26), $c_{PFC}(r)$ decreases for larger $c_{l,PFC}$ values due to the MGF and VG effect, as illustrated in Figure 24.

5.3 Blade simulations

The rotor blade simulations are performed using the steady Blade Element Momentum (BEM) method, which is embedded into QBlade, v99 based on Hansen (2015). The BEM simulation entirely depends on the quality of the imported polar data. Furthermore, empirical correction algorithms are activated, as described in Marten et al. (2013), including root and tip losses, thrust forces of heavily loaded rotors (Glauert correction) and spanwise crossflow effects. Apart from that, the results are interpolated between adjacent blade sections. The power curves are determined with respect to a rated power output of $P_{\text{max}} = 600$ kW at $u_{\text{rated}} = 12$ m/s. In all cases, the basic pitch and rpm controller settings are optimized for reaching maximum power output. Following Gasch and Tewe (2012), the AEP or E is calculated by means of the Weibull distribution using the probability factors $k = 2$ for a typical site in central Europe and the average wind speed at hub height, $u_{\text{avg}} = 7$ m/s over an operational wind speed range between $u_{\text{cut-in}} = 3$ m/s and $u_{\text{cut-out}} = 25$ m/s.

5.3.1 Retrofit application

The BEM results of the retrofit application are presented. Figure 23 shows the AoA along the local rotor radius, r . The clean baseline coincides with $\alpha_{\text{opt, clean}}(L/D_{\text{max}}) = 9.5^\circ$ of the DU97W300 and $\alpha_{\text{opt, clean}} = 6.4^\circ$ of the NACA63(3)618. Replacing the clean by the tripped polar data, the AoA are significantly increased, see Figure 23a. In fact, the DU97W300 is stalling for $\alpha > 10.5^\circ$, so that the local L/D drops dramatically towards the root region, see Figure 23b. This adverse effect of the ZZ tape is partly compensated for by the PFC devices: the AoA are much closer to $\alpha_{\text{opt, clean}}$, so that $L/D(r)$ is partly recovered indicating that the PFC configuration is less sensitive to LER. Figure 23c shows the power coefficients over the complete operational range of the rotor. In the tripped case, the c_p curve is shifted towards higher TSR, so that $\lambda(c_{p, \text{max}, \text{ZZ}}) = 8$ rather than $\lambda_{\text{opt}} = 7$. Hence, $c_{p, \text{max}, \text{clean}}(\lambda_{\text{opt}}) = 0.48$ is decreased by 13 % to $c_{p, \text{max}, \text{ZZ}}(\lambda_{\text{opt}}) = 0.42$. After the retrofit application, the c_p curve is closer to the design point with $c_{p, \text{max}, \text{PFC(ZZ)}}(\lambda_{\text{opt}}) = 0.45$, so that the relative decrease is reduced to 5.7 %.

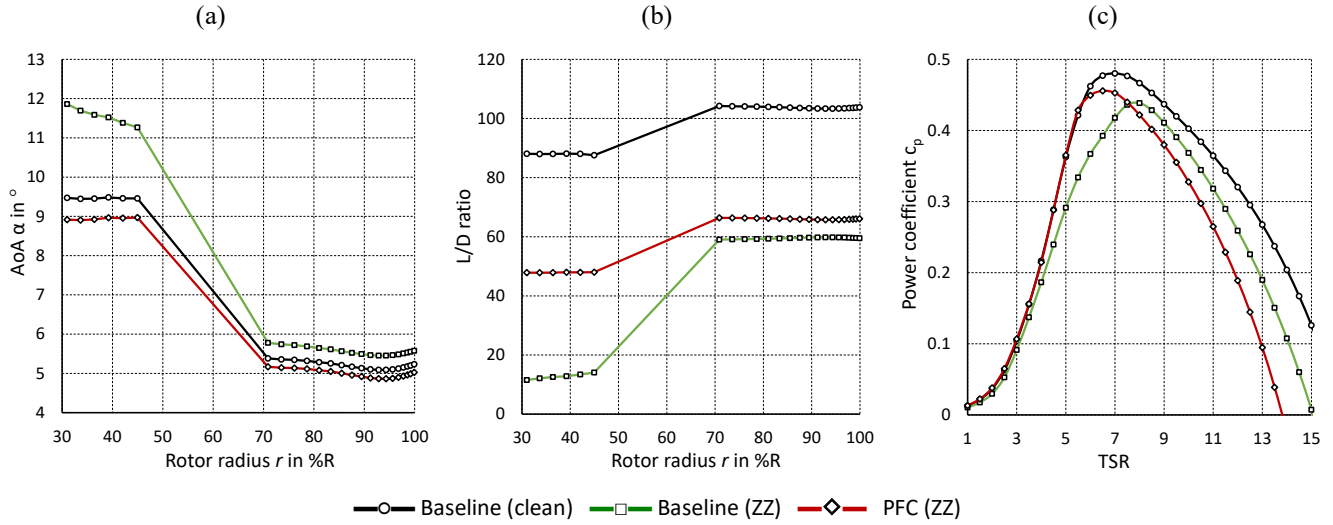


Figure 23. Rotor blade performance simulation of baseline and retrofit application. (a) AoA over rotor radius at $\lambda_{opt} = 7$. (b) L/D over rotor radius at $\lambda_{opt} = 7$. (c) Power coefficients over TSR.

625 Furthermore, the AEP amounts to $E_{clean} = 1594$ MWh, $E_{ZZ} = 1464$ MWh (-8.2 %) and $E_{PFC(ZZ)} = 1529$ MWh (-4.1 %). In this generic case study, the energy decline due to forced LE transition is approximately halved by the retrofit application of MGFs and VGs.

5.3.2 New design application

The BEM results of the new design application are presented. According to Eq. (26), the lift increase caused by the MGFs
 630 leads to a significant chord length reduction, as illustrated in Figure 24a and b.

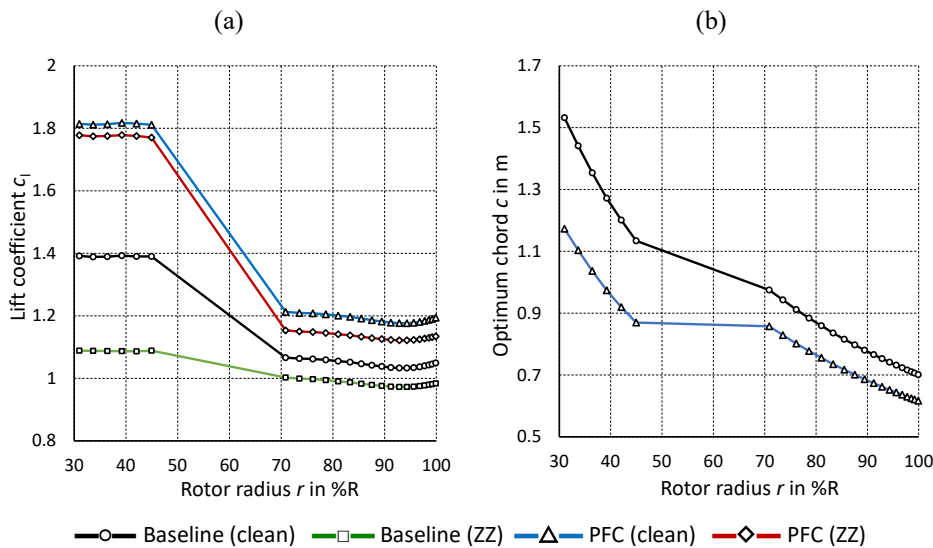


Figure 24. Blade geometry of baseline and new design application at $\lambda_{opt} = 7$. (a) Lift coefficients over rotor radius (b) Optimum chord length over rotor radius.



Compared to the baseline case, $c_{PFC}(r)$ is reduced by 23.4 % in the root and by 12 % in the tip region. Regardless of any structural-dynamic considerations, this approach potentially contributes to the development of more slender and thus lighter blades. Apart from saving material costs, as previously suggested by Fuglsang et al. (2004), see Sect. 1.5, periodic gravitational load alternations and thus fatigue loads might be mitigated.

Next, Figure 25 shows the BEM simulation results. It is reiterated that the clean and tripped baseline configurations are identical to the retrofit application.

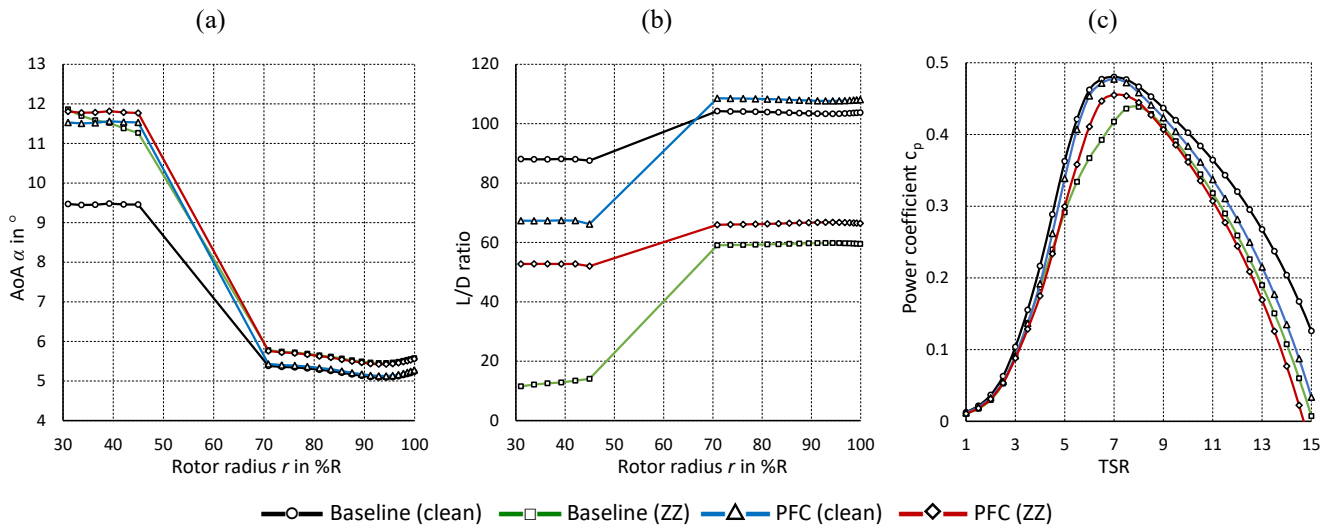


Figure 25. Rotor blade performance simulation of baseline and new design application. (a) AoA over rotor radius at $\lambda_{opt} = 7$. (b) L/D over rotor radius at $\lambda_{opt} = 7$. (c) Power coefficients over TSR.

Looking at the root region, the design AoA at $\lambda_{opt} = 7$ is shifted from $\alpha_{opt,Base(clean)} \approx 9.5^\circ$ to $\alpha_{opt,Base(ZZ)} \approx 11.5^\circ$, where the DU97W300 is already stalling, see Figure 25a. The clean and the tripped PFC cases, on the other hand, lead to a significantly higher design AoA, i.e. $\alpha_{opt,PFC} \approx 12^\circ$. Unlike the baseline configurations, stall is delayed by the VGs until $\alpha_{cl,max,PFC} \approx 16^\circ$. In the tip region, the MGF configuration leads to identical $\alpha(\lambda_{opt})$ compared to the respective baseline. As a result, $L/D_{clean}(r)$ in the root region is decreased compared to the clean baseline due to the drag penalty of the PFC devices, see Figure 25b. However, in the tripped case, the reduction of $L/D_{PFC(ZZ)}(r)$ is significantly less severe compared to the baseline case because of stall delay. Moreover, looking at the tip region, the MGF effect leads to elevated $L/D(r)$ in both the clean and, particularly, the tripped case. Again, the L/D curves indicate that the PFC configuration is less sensitive to LER. Figure 25c shows the c_p curves. In the tripped baseline case, the design TSR is shifted to $\lambda(c_{p,max,ZZ}) = 8$ rather than $\lambda_{opt} = 7$. For both PFC cases, $c_{p,max,PFC}$ remains at $\lambda_{opt} = 7$, so that the overall shape of the clean baseline curve is maintained. As a consequence, $c_{p,max,PFC(clean)} = 0.48$ is almost identical to the clean baseline, despite moderate differences at elevated TSR, i.e. for $\lambda > \lambda_{opt}$. Furthermore, $c_{p,max,PFC(ZZ)}(\lambda_{opt}) = 0.45$ decreases by only 4.6 % rather than 13 % compared to the respective clean case. The AEP amounts to $E_{Base(clean)} = 1594$ MWh and $E_{Base(ZZ)} = 1464$ MWh (-8.2%), compared to $E_{PFC(clean)} = 1587$ MWh and $E_{PFC(ZZ)} = 1536$ MWh (-3.6%).



Hence, the difference between the clean baseline and clean PFC configuration is minor. In addition, the blades are more slender and the energy decline due to forced LE transition is mitigated by the new design application of MGFs and VGs.

6 Conclusions

The present study investigates the use of MGFs and their combination with VGs for improved rotor blade performance of HAWTs. The main conclusions are summarized alongside each sections of this report.

1. The aerodynamic effects of either GFs or VGs on the airfoil performance is well documented in literature. Various wind tunnel studies emphasize the benefits of very small GFs, so-called MGFs, particularly in terms of the aerodynamic efficiency. However, the simultaneous installation of GFs and VGs is less profoundly researched.
2. The simulation software XFOIL is used to determine the appropriate dimensions of each PFC device in relation to the boundary layer displacement thickness of the following airfoils: the NACA63(3)618, the AH93W174 and the DU97W300. The definition of a MGF refers to an effective height in the range of one to two times the local boundary layer displacement thickness at the design AoA. Within this boundary condition, the MGF effect on the airfoil performance appears to be beneficial in terms of the lift performance, the stall behavior and the aerodynamic efficiency.
3. The baseline results of the tested airfoils are validated against literature data. The effects of the PFC devices are captured successfully by the current measurement methods, i.e. the force balance for the lift, and the wake rake for the drag coefficients. Furthermore, the wake rake registers both the increased downwash angle due to the GFs and the stall delay due to the VGs. Compared to the clean baseline, the additional intensity of the wake unsteadiness diminishes in relation to the GF height, i.e. using MGFs.
4. The impact of MGFs and VGs depends on whether the free or the forced boundary layer transition is applied. MGFs (only) increase the pre-stall lift performance compared to the corresponding baseline. The aerodynamic efficiency is maintained in the clean, and improved in the tripped case. Combining MGFs and VGs leads to stall delay, lift increase and a significant improvement of the aerodynamic efficiency in the tripped case. However, in the clean case, maximum L/D is decreased due to the combined drag penalty. In summary, the selected configurations include the smallest MGF height of 0.25 %c on both the NACA63(3)618 and the AH93W174, and the medium sized MGF height of 0.5 %c plus VGs with a height of 1.1 %c on the DU97W300.
5. The experimental polar data is imported into the software QBlade in order to create an aerodynamically optimized rotor blade. The performance of the generic rotor blade is simulated based on two case studies, the retrofit application on an existing, and the new design application on a alternative rotor blade. The retrofit application alleviates the adverse effects of the ZZ tape. Separation is delayed in the root to mid region, and the aerodynamic efficiency and thus power output, is recovered in the mid to tip region of the blade. The new design application leads to a more



slender blade while maintaining the power output. Furthermore, the alternative blade appears to be more resistant against the effects of forced leading edge transition.



Further research on MGFs and their interaction with relatively small VGs is recommended, especially considering leading edge roughness effects. Next steps involve the design of Mini VGs in conjunction with Mini GFs to further reduce drag. Moreover, advanced methods for emulating different degrees of leading edge roughness should be applied. In addition, a complete aeroelastic simulation of the rotor performance is required, especially with regard to open field tests of MGFs in combination with VGs on large wind turbine rotor blades.

Appendix A: AH93W174

The wind tunnel results of the AH93W174 are presented alongside the NACA63(3)618 and the DU97W300, see Sect. 4. For brevity, only the L/D graphs and the characteristic lift and L/D values are included in A2 and A3.

A1. Baseline

The clean and the tripped polar curves are presented. Stall is initiated at $\alpha_{cl,max} = 10.5^\circ$ and $\alpha_{opt, clean} = 8.5^\circ$ decreases to $\alpha_{opt, ZZ} = 5.3^\circ$, see Figure A1a. Figure A1b shows that the aerodynamic efficiency drops from $L/D_{max, clean} = 118$ to $L/D_{max, ZZ} = 61$. For clarity, characteristic lift and L/D values are summarized in Table A 1.

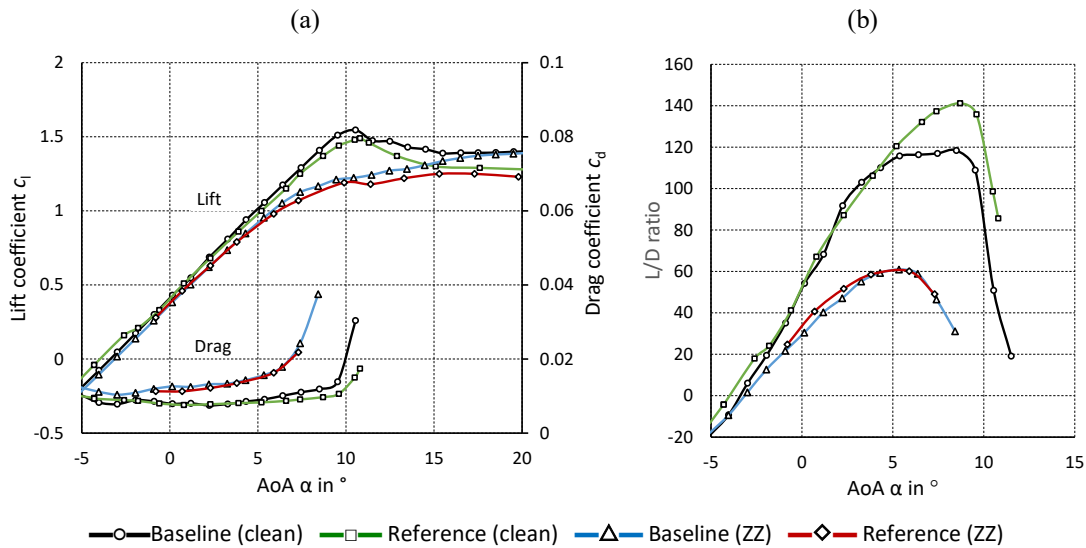


Figure A1. AH93W174. Clean and tripped baseline cases at $Re = 1.5 \cdot 10^6$ compared to reference data from Althaus (1996) at $Re = 1.5 \cdot 10^6$. (a) Lift and drag coefficients. (b) L/D ratio.

The baseline measurements are compared to literature data from the airfoil catalogue of Althaus (1996). The AH93W174 was tested in the laminar wind tunnel of the IAG at Stuttgart University. The inflow turbulence in the open return test section was



0.012 %. Lift and drag were determined at $Re = 1.5 \cdot 10^6$ using the methods that were previously mentioned in case of the NACA63(3)618, see Sect. 4.1.1. The wake rake was positioned 30%c downstream the airfoil TE. Forced LE transition was triggered at the SuS (only) via trip wire using a diameter of 0.3mm at $x_{SuS} = 5.0$ %c.

Figure A1a shows very good agreement between both lift and drag curves, despite slight deviations approaching $c_{l,max}$. Furthermore, the clean case shows a steeper drag increase at elevated AoA resulting in reduced $L/D_{max, clean}$ compared to the reference data, see Figure A1b. The reason is probably the inflow turbulence, which is significantly stronger in case of the current measurements, hence leading to earlier transition at elevated AoA and thus higher drag values. Moreover, the difference in the rake positions downstream the airfoil TE, i.e. 30%c versus 100%c, might contribute to the deviations in the drag results.

A2. Mini Gurney flaps

The polar curves of all GF configurations are presented. Overall, the results agree with the NACA63(3)618 measurements, see Sect. 4.1.2. For brevity, only the L/D graphs and the characteristic lift and L/D values are shown. According to Figure A 2 and Table A 1, the preferable results are achieved for GF025 in the clean, and GF05 as well as GF1 in the tripped case. Again, the beneficial GF effect is more pronounced in the tripped cases.

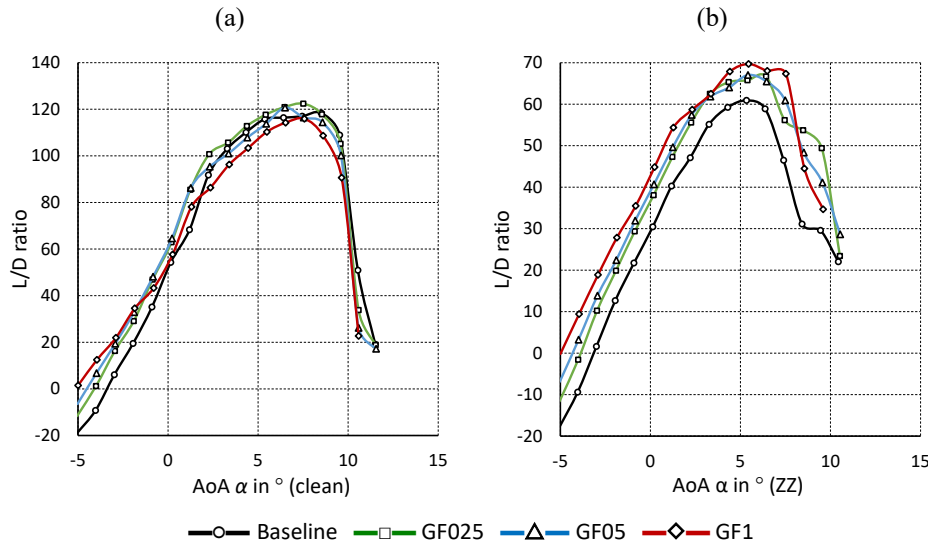


Figure A 2. AH93W174. Gurney flaps. (a) L/D ratio (clean). (b) L/D ratio (ZZ).

Table A 1. AH93W174. Gurney flaps. Characteristic values.

AH93W174				
	Clean		Tripped	
	$c_{l,max}$ (9.5°)	L/D_{max} (7.5°)	$c_{l,max}$ (10.5°)	L/D_{max} (5.4°)
Baseline	1.51	117	1.22	61



GF025	1.66	122	1.37	66
GF05	1.73	116	1.44	67
GF1	1.83	116	1.55	70

A3. Vortex generators plus Mini Gurney flaps

The polar curves of all VG + GF configurations are presented. Overall, the AH93W174 results agree with the NACA63(3)618 measurements. In fact, the beneficial effects of both the VG (only) and the VG + GF configurations are significantly more pronounced: $\alpha_{cl,max}$ is shifted by around 6° and $\alpha_{opt,ZZ}$ by approximately 5° , so that a large area of otherwise separated flow is recovered at elevated AoA. Hence, in both cases, the preferred results are achieved using VG + GF025. For brevity, only the

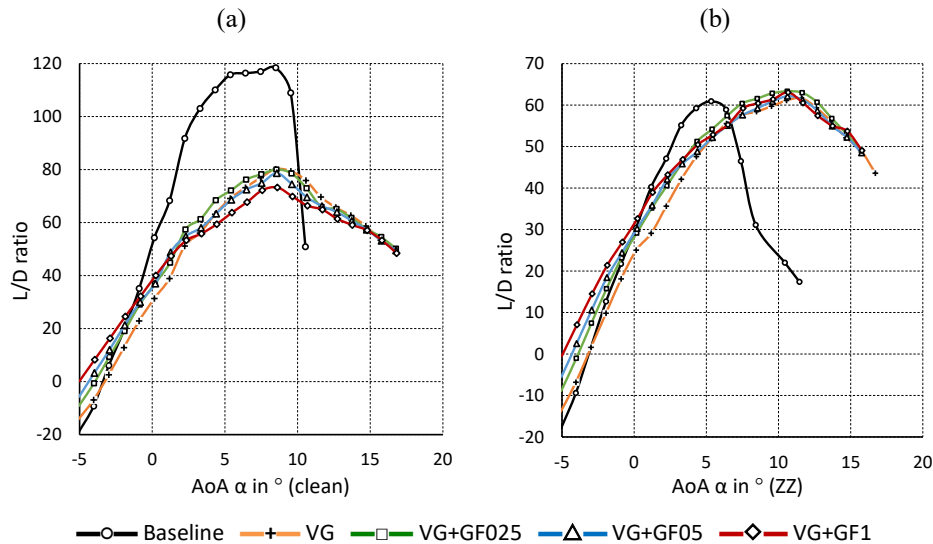


Figure A 3. AH93W174. Vortex generators and Gurney flaps. (a) L/D ratio (clean). (b) L/D ratio (ZZ).

Table A 2. AH93W174. Vortex generators combined with Gurney flaps. Characteristic values.

AH93W174				
	Clean		Tripped	
	$c_{l,max}(\alpha)$	$L/D_{max}(\alpha)$	$c_{l,max}(\alpha)$	$L/D_{max}(\alpha)$
Baseline	1.55 (10.5°)	118 (8.5°)	1.55 (10.5°)	61 (5.3°)
VG	2.05 (16.7°)	80 (8.5°)	2.05 (16.7°)	61 (10.6°)
VG+GF025	2.18 (16.7°)	80 (8.5°)	2.11 (15.8°)	63 (10.6°)
VG+GF05	2.25 (16.7°)	79 (8.5°)	2.19 (15.8°)	62 (10.6°)
VG+GF1	2.35 (16.7°)	73 (8.5°)	2.28 (15.8°)	63 (10.6°)



Data availability.

730 Measurement data and results can be provided by contacting the corresponding author.

Author contribution

JF designed and fabricated the wake rake and the vortex generators. JA validated the wake rake measurements and designed the Mini Gurney flaps. JA, MM, GWD, JF and AS prepared and conducted the wind tunnel experiments. JA performed the airfoil and rotor blade simulations. JA and AS processed the experimental and numerical data. JA wrote the manuscript with
735 the support of all co-authors, who contributed with important suggestions.

Competing interests

The authors declare that they have no conflict of interest.

Acknowledgements

The authors would also like to appreciate the constant support of the technicians of the Hermann-Föttinger Institut at the
740 Technische Universität Berlin.

References

- Abbott, I.H., and von Doenhoff, A.E.: Theory of Wing Sections, Dover publications, Inc. New York, ISBN 100486605868, 1959.
- 745 Alber, J., Pechlivanoglou, G., Paschereit, C. O., Twele, J., and Weinzierl, G.: Parametric Investigation of Gurney Flaps for the Use on Wind Turbine Blades, in: Proceedings of the ASME Turbo Expo 2017, Volume 9, Wind Energy, Charlotte, North Carolina, USA, Paper GT2017-64475, <https://doi.org/10.1115/GT2017-64475>, June, 2017.
- Althaus, D.: Niedriggeschwindigkeitsprofile: Profilentwicklungen und Polarenmessungen im Laminarwindkanal des Instituts
750 für Aerodynamik und Gasdynamik der Universität Stuttgart, Vieweg & Sohn Verlagsgesellschaft mbH, ISBN 3-528-03820-9, 1996.
- Bach, A. B., Lennie, M., Pechlivanoglou, G., Nayeri, C. N. and Paschereit, C. O.: Finite micro-tab system for load control on a wind turbine, Journal of Physics: Conference Series, Volume 524, <http://dx.doi.org/10.1088/1742-6596/524/1/012082>, 2014.



755

Bak, C., Skrzypiński, W., Fischer, A., Gaunaa, M., Brønnum, N. F. and Kruse, E. K.: Wind tunnel tests of an airfoil with 18% relative thickness equipped with vortex generators, Journal of Physics: Conference Series, Volume 1037, Issue 2, <http://dx.doi.org/10.1088/1742-6596/1037/2/022044>, 2018.

760

Bak, C., Skrzypiński, W., Gaunaa, M., Villanueva, H., Brønnum, N. F. and Kruse, E. K.: Full scale wind turbine test of vortex generators mounted on the entire blade, Journal of Physics: Conference Series, Volume 753, Issue 2, <http://dx.doi.org/10.1088/1742-6596/753/2/022001>, 2016.

765

Bak, C., Zahle, F., Bitsche, R., Kim, T., Yde, A., Henriksen, L. C., Natarajan, A., and Hansen, M.: Description of the DTU 10 MW Reference Wind Turbine, Technical University of Denmark, DTU Wind Energy Report-I-0092, June 2013.

770

Baldacchino, D., Ferreira, C., de Tavernier, D., Timmer, W. A. and van Bussel, G. J. W.: Experimental parameter study for passive vortex generators on a 30% thick airfoil, Wind Energy. 2018, Vol. 21, p. 745-765, <https://doi.org/10.1002/we.2191>, 2018.

Barlas, T.K., Kuik, van G. A. M.: Review of state of the art in smart rotor control research for wind turbines, Progress in Aerospace Sciences, Vol. 46, Issue 1, p. 1-27, ISSN 0376-0421, <https://doi.org/10.1016/j.paerosci.2009.08.002>, 2010.

Barlow, J. B., Rae, W. H. and Pope, A.: Low-Speed Wind Tunnel Testing, John Wiley & Sons, 3rd edition, USA, <https://doi.org/10.2514/2.633>, 1999.

775

Bechert, D. W., Meyer, R., and Hage, W.: Drag reduction of airfoils with miniflaps – Can we learn from dragonflies?, AIAA Fluids 2000 Conference and Exhibit, Denver, USA, Paper 2000-2315, <https://doi.org/10.2514/6.2000-2315>, June 2000.

780

Bechert, D., Meyer, R., and Hage, W.: Airfoil with performance enhancing trailing edge, Europäische Patentschrift, Patent Number: 01250001.3, Date of Patent: 2nd of January 2001.

Boyd, J. A.: Trailing edge device for an airfoil, United States Patent, Patent Number: 4,542,868, Date of Patent: 24th of September, 1985.

785

Brink, am B. K.: Trailing edge wedge for an aircraft wing, United States Patent, Patent Number: US 6,382,561 B1, Date of Patent: 7th of May 2002.

Cole, J. A., Vieira, B. A. O., Coder, J. G., Premi, A. and Maughmer, M. D.: Experimental Investigation into the Effect of Gurney Flaps on Various Airfoils, Journal of Aircraft, Vol. 50, No. 4, <https://doi.org/10.2514/1.C032203>, 2013.



- 790 Drela, M.: XFOIL: An Analysis and Design System for Low Reynolds Number Airfoils, in: Mueller, T. J., Low Reynolds
 Number Aerodynamics, Vol. 54, Springer Berlin, Heidelberg, https://doi.org/10.1007/978-3-642-84010-4_1, 1989.
- Fuglsang, P., Bak, C., Gaunaa, M. and Antoniou, I.: Design and Verification of the Risø-B1 Airfoil Family for Wind Turbines,
 ASME. J. Sol. Energy Eng, Vol. 126, p. 1002-1010, <https://doi.org/10.1115/1.1766024>, November 2004.
- 795 Fuglsang, P., Bak, C., Gaunaa, M. and Antoniou, I.: Wind tunnel tests of Risø-B1-18 and Risø-B1-24, Forskningscenter Risø,
 Risø-R-1375(EN), 2003.
- Fuglsang, P., Dahl, K. S. and Antoniou, I.: Wind tunnel tests of the Risø-A1-18, Risø-A1-21 and Risø-A1-24 airfoils,
 800 Forskningscenter Risø, Risø-R-1112(EN), 1999.
- Gasch, R. and Tvele, J.: Wind Power Plants - Fundamentals, Design, Construction and Operation, Springer-Verlag Berlin
 Heidelberg, <https://doi.org/10.1007/978-3-642-22938-1>, 2012.
- 805 Giguère, P., Dumas, G. and Lemay, J.: Gurney Flap Scaling for Optimum Lift-to-Drag Ratio, AIAA Journal, Vol.35, No. 12,
<https://doi.org/10.2514/2.49>, December 1997.
- Giguère, P., Lemay, J., and Dumas, G.: Gurney flap effects and scaling for low-speed airfoils, in: 13th AIAA Applied
 Aerodynamics Conference, San Diego, USA, Paper 1995-1881-CP, <https://doi.org/10.2514/6.1995-1881>, June, 1995.
- 810 González-Salcedo, Á., Croce, A., León, C. A., Nayeri, C. N., Baldacchino, D., Vimalakanthan K., and Barlas, T.: Blade Design
 with Passive Flow Control Technologies, p. 11-16, in: Stoevesandt B., Schepers G., Fuglsang P., and Yuping S. (eds):
 Handbook of Wind Energy Aerodynamics, Springer, Cham., https://doi.org/10.1007/978-3-030-05455-7_6-1, 2020.
- 815 Gruschwitz, E. and Schrenk, O.: A simple method for increasing the lift of airplane wings by means of flaps, National Advisory
 Committee for Aeronautics, N.A.C.A. Technical Memorandum, No. 714, Washington, 1933.
- Hansen, M. O. L.: Aerodynamics of Wind Turbines, 3rd edition, Earthscan from Routledge, Taylor & Francis Group, London,
 UK, <https://doi.org/10.4324/9781315769981>, 2015.
- 820 Henne, P. A. and Gregg, R. D.: Divergent trailing-edge airfoil, United States Patent, Patent Number: 4,858,852, Date of Patent:
 22th of August 1989.



Jeffrey, D., Zhan, X. and Hurst, D. W.: Aerodynamics of Gurney Flaps on a Single-Element High-Lift Wing, *Journal of Aircraft*, Vol. 37, No. 2, <https://doi.org/10.2514/2.2593>, April 2000.

Jonkman, J., Butterfield, S., Musial, W. and Scott, G.: Definition of a 5-MW Reference Wind Turbine for Offshore System Development, National Renewable Energy Lab. (NREL), Technical Report NREL/TP-500-38060, <https://doi.org/10.2172/947422>, 2009.

830

Kentfield, J.: The Influence of Free-Stream Turbulence Intensity on the Performance of Gurney-Flap Equipped Wind-Turbine Blades, *Wind Engineering*, <https://www.jstor.org/stable/43749607.1996>.

Liebeck, R. H.: Design of Subsonic Airfoils for High Lift, in: 9th AIAA Fluid and Plasma Dynamics Conference, Vol. 15, No. 9, Paper 76-406, San Diego, USA, <https://doi.org/10.2514/3.58406>, 1978.

835

Lin, J. C.: Review of research on low-profile vortex generators to control boundary-layer separation, *Progress in Aerospace Sciences*, Vol. 38, Issues 4–5, p. 389-420, ISSN 0376-0421, [https://doi.org/10.1016/S0376-0421\(02\)00010-6](https://doi.org/10.1016/S0376-0421(02)00010-6), 2002.

Li-shu, H., Chao, G., Wen-Ping S. and Ke, S.: Airfoil flow control using vortex generators and a Gurney flap, *Journal of Mechanical Engineering Science*, Vol. 227, Issue 12, p. 2701-2706, <https://doi.org/10.1177/0954406213478533>, 2013.

840

Maniaci, D. C., Westergaard, C., Hsieh, A. and Paquette, J. A.: Uncertainty Quantification of Leading Edge Erosion Impacts on Wind Turbine Performance, *Journal of Physics: Conference Series*, Vol. 1618, <http://dx.doi.org/10.1088/1742-6596/1618/5/052082>, 2020.

845

Manolesos, M. and Voutsinas, S. G.: Experimental investigation of the flow past passive vortex generators on an airfoil experiencing three-dimensional separation, *Journal of Wind Engineering and Industrial Aerodynamics*, Vol. 142, p.130-148, ISSN 0167-6105, <https://doi.org/10.1016/j.jweia.2015.03.020>, 2015.

850

Marten, D., Wendler, J., Pechlivanoglou, G., Nayeri, C. N., and Paschereit, C. O.: Development and Application of a Simulation Tool for Vertical and Horizontal Axis Wind Turbines, *ASME Turbo Expo 2013*, Volume 8, San Antonio, Texas, USA, Paper GT2013- 94979, <https://doi.org/10.1115/GT2013-94979>, June 2013.

Marten, D.: QBlade: A Modern Tool for the Aeroelastic Simulation of Wind Turbines, Doctoral Thesis, Technische Universität Berlin, DOI:10.14279/depositonce-10646, <https://depositonce.tu-berlin.de/handle/11303/11758>, 2020.

855



Meyer, R., Hage, W., Bechert, D. W., Schatz, M. and Thiele, F.: Drag Reduction on Gurney Flaps by Three-Dimensional Modifications, Journal of Aircraft, Vol. 43, No. 1, <https://doi.org/10.2514/1.14294>, February 2006.

860

Meyer, R., K., J.: Experimentelle Untersuchungen von Rückstromklappen auf Tragflügeln zur Beeinflussung von Strömungsablösungen, PhD Thesis, Technische Universität Berlin, Hermann-Föttinger-Institut für Strömungsmechanik, December 2000.

865 Mueller-Vahl, H., Pechlivanoglou, G., Nayeri, C. N. and Paschereit, C. O.: Vortex Generators for Wind Turbine Blades: A combined Wind Tunnel and Wind Turbine Parametric Study, ASME Turbo Expo, GT2012-69197, <https://doi.org/10.1115/GT2012-69197>, 2012.

Oerlemans S., Fisher, M., Maeder T. and Kögler, K.: Reduction of Wind Turbine Noise Using Optimized Airfoils and Trailing-
870 Edge Serrations, AIAA Journal, Vol. 47, No. 6, <https://arc.aiaa.org/doi/10.2514/1.38888>, June 2009.

Papi, F., Balduzzi, F., Ferrara, G. and Bianchini, A.: Uncertainty quantification on the effects of rain-induced erosion on annual energy production and performance of a Multi-MW wind turbine, in: Renewable Energy, Vol.165, p. 701-715, <https://doi.org/10.1016/j.renene.2020.11.071>, 2021.

875

Pechlivanoglou, G., Nayeri, C. N. and Paschereit, C. O.: Performance Optimization of Wind Turbine Rotors With Active Flow Control, Proceedings of the ASME 2011 Turbo Expo, Vol. 1, pp. 763-775, Vancouver, Canada, <https://doi.org/10.1115/GT2011-45493>, June 2011.

880 Pechlivanoglou, G.: Passive and active flow control solutions for wind turbine blades, PhD Thesis, Technischen Universität Berlin, Fakultät V - Verkehrs- und Maschinensysteme, 2013.

Schatz, M., Günther, B., and Thiele, F.: Numerical Simulation of the Unsteady Wake behind Gurney-Flaps, available at: https://www.cfd.tu-berlin.de/research/flowcontrol/gurneys_en/ (last access: 17 October 2020), 2004a.

885

Schatz, M., Günther, B., and Thiele, F.: Computational modelling of the unsteady wake behind Gurney-flaps, 2nd AIAA Flow Control Conference Portland, Oregon, USA, Paper 2004-2417, <https://doi.org/10.2514/6.2004-2417>, June 2004b.



890 Schlichting, H. and Gersten, K.: Boundary-Layer Theory, Springer-Verlag Berlin Heidelberg, Edition Number 9,
<https://doi.org/10.1007/978-3-662-52919-5>, 2000.

Schmitz, G.: Theorie und Entwurf von Windrädern optimaler Leistung (Theory and design of windwheels with an optimum performance), Wiss. Zeitschrift der Universität Rostock, 5. Jahrgang, 1955/56.

895

SMART BLADE: <https://www.smart-blade.com/vortex-generators> (last access: 17 October 2021), 2021.

Storms, B. L. and Jang, C. S.: Lift Enhancement of an Airfoil Using a Gurney Flap and Vortex Generators, in: 31st AIAA Aerospace Sciences Meeting, Journal of Aircraft, Vol. 31, No. 3, Paper 93-0647, Reno, Nevada, USA,
 900 <https://doi.org/10.2514/3.46528>, May, 1994.

Timmer, W. A. and van Rooij, R. P. J. O. M.: Summary of the Delft University Wind Turbine Dedicated Airfoils , ASME. J. Sol. Energy Eng, Vol. 125(4), p. 488-496, <https://doi.org/10.1115/1.1626129>, November 2003.

905 Timmer, W. A.: An overview of NACA 6-digit airfoil series characteristics with reference to airfoils for large wind turbine blades, 47th AIAA Aerospace Sciences Meeting, Orlando, Florida, AIAA 2009-268, <https://doi.org/10.2514/6.2009-268>, January 2009.

Timmer, W.A. and Schaffarczyk, A.P.: The effect of roughness at high Reynolds numbers on the performance of aerofoil DU
 910 97-W-300Mod, Wind Energ., 7: 295-307, <https://doi.org/10.1002/we.136>, 2004.

van Rooij, R. P. J. O. M. and Timmer, W. A.: Roughness Sensitivity Considerations for Thick Rotor Blade Airfoils, 41st Aerospace Science Meeting and Exhibit, Reno, Nevada, USA, AIAA Paper 2003-0350, January 2003,
<https://doi.org/10.2514/6.2003-350>.

915

Vestas: Aerodynamic upgrades, PowerPlus™ case study, available at:
<https://nozebra.ipapercms.dk/Vestas/Communication/Productbrochure/ProductImprovements/aerodynamic-upgrades-case-study/>, (last access: 17th of October 2021), 2019.

920 Wang, J. J., Li, Y. C., and Choi, K.-S.: Gurney flap - Lift enhancement, mechanisms and applications, Progress in Aerospace Sciences, Vol. 44, Issue 1, p. 22-47, ISSN 0376-0421, <https://doi.org/10.1016/j.paerosci.2007.10.001>, January 2008.

Wilcox, B. J., White, E. B., and Maniaci, D. C.: Roughness Sensitivity Comparisons of Wind Turbine Blade Sections, Sandia Report, SAND2017-11288, <https://doi.org/10.2172/1404826>, 2017.



- 925 Zaparka, E. F.: Aircraft and control thereof, United States Patent, Re. 19,412, Original No. 1,893,065, Date of Patent: 1st of January 1935.